LONGSHORE CURRENTS NEAR CAPE HATTERAS, NC

A Thesis
Presented to
The Academic Faculty

by

Stephanie M. Smallegan

In Partial Fulfillment
of the Requirements for the Degree
Master of Science in the
School of Civil and Environmental Engineering

Georgia Institute of Technology
May 2012

LONGSHORE CURRENTS NEAR CAPE HATTERAS, NC

Approved by:

Dr. Kevin A. Haas, Advisor
School of Civil and Environmental Engineering
Georgia Institute of Technology

Dr. Paul A. Work
School of Civil and Environmental Engineering
Georgia Institute of Technology

Dr. Hermann Fritz
School of Civil and Environmental Engineering
Georgia Institute of Technology

Date Approved: March 29, 2012

ACKNOWLEDGEMENTS

The present work was funded by the United States Geological Survey Carolinas Coastal Change Processes Project and by the National Science Foundation Graduate Research Fellowship under grant number DGE – 1148903. I want to thank my advisor, Dr. Kevin Haas, for his continued support in my research, repeated reviews of my thesis, and for teaching, motivating, and encouraging me especially through the difficult times. I have been given so many opportunities to further my career through conferences and professional meetings because of his guidance and believing I am capable of success. I also thank my committee members, Dr. Hermann Fritz and Dr. Paul Work, for their time and input on my thesis and for attending my defense. Thank you to Dr. Jeff List, Dr. John Warner and Brandy Armstrong with USGS and Nirnimesh Kumar with the University of South Carolina for answering questions and providing data essential to completing this work.

Thank you to Brittany and Jack Bruder for constantly leaving words, poor sketches, and paw prints of encouragement on my desk. Also, thank you Brittany, Xiufeng Yang and Brian McFall for helping me through homework assignments and studying for exams in the classes we took together. Lulu also thanks Brittany and Xiufeng for remembering to water her when I was out of the office. I thank Mama and Daddy for constantly praying for me, reminding me that they are proud of me and that I am fulfilling my dreams. I also want to thank Kyle Smallegan for sticking with me through all of this, making difficult sacrifices, but still encouraging me every day that this research is what I love and what I am meant to do. Most of all, I thank my God for the strength, encouragement, wisdom, and knowledge that I needed to complete this work. Thank you for allowing me to understand the difficult concepts and for teaching me how to find peace through your grace.

TABLE OF CONTENTS

LIST OF TABLES

LIST OF FIGURES

SUMMARY

As part of a beach erosion field experiment conducted at Cape Hatteras, NC in February 2010, this study focuses on quantifying longshore currents, which are the basic mechanism that drives longshore sediment transport. Using video imagery, the longshore currents in view of a video camera are estimated with the Optical Current Meter technique and the nearshore morphology is estimated by analyzing breaking wave patterns in standard deviation images.

During a Nor'easter storm event on February 12 and 13, 2010, the video longshore currents are compared to in situ data and it is found that the currents are most affected by the angle of incidence of incoming waves, increasing in magnitude as the angle becomes more oblique due to a larger component of radiation stress forcing in the longshore direction. The magnitude of the radiation stress forcing, which is at least an order of magnitude larger than the surface wind stress, increases as wave height increases or tide level decreases, which causes more wave breaking to occur. The normalized standard deviation images show wave breaking occurring at an inshore and offshore location, corresponding closely to the locations of an inner and outer bar indicated in survey data.

Using two profiles from the survey data, one profile that intersects a trough and one that intersects a terrace, the video currents are also compared to currents simulated in one-dimension using the circulation module, SHORECIRC, and the wave module, REF/DIF-S, as part of the NearCoM system. Although the simulated currents greatly underpredict the video currents when the flow is only driven by radiation stresses, a mean water level difference between the two profiles creates a longshore pressure gradient. Superimposing a pressure gradient forcing term into the longshore momentum balance that assumes an equilibrium state of the flow, the magnitude of the simulated currents are much larger than the magnitude of the video estimated currents. Using analytical solutions of simplified forms of the mass and momentum equations to determine the effects of accelerations on the flow, it is seen that the acceleration term greatly affects the flow due to the relatively large mean water level difference that acts over a relatively short distance. Therefore, the pressure gradient forcing term is modified to include the effects of accelerations. By including the two-dimensional effects of the acceleration in the one-dimensional model through the modified pressure gradient, the quasi two-dimensional model simulated currents are very similar to the video estimated currents, indicating that the currents observed in the video may be pressure gradient driven.

CHAPTER 1

INTRODUCTION

Coastal erosion is a complex process that changes the shorelines of waterfront property and can lead to significant damage of infrastructure. According to the Center for Environment and Population, 17% of the United States landmass is coastal counties and half of the current population resides in these counties (Markham and Steinzor, 2006). The existence of the homes, businesses, and investments of the coastal community is dependent on a stable shoreline. Therefore, it is imperative to develop a better understanding of the processes that drive coastal erosion so that shoreline evolution can be predicted and mitigated.

Changes in coastal morphology, which include erosion by diverging transport and accretion by converging transport, is a result of the action by waves and currents. Coastal sediment transport has two modes: cross-shore transport driven by waves and undertow, and longshore transport primarily driven by currents. Although the shoreline can evolve rapidly in response to cross-shore transport driven by short term events, long term shoreline changes may be related to variations in longshore transport.

The basic mechanism for longshore transport is longshore currents, which is the focus of the present study. Longshore currents are measured and observed for the Cape Hatteras area, which is part of the Outer Banks of North Carolina. The cape and its associated shoal complex, Diamond Shoals, is part of a cuspate foreland, which is a series of gigantic cusps and shoal complexes. Each shoal complex is a huge sink (or possibly source) in the sediment budget, continually shaping the adjacent coastline, but the processes that drive longshore currents and maintain the shoals are mostly unknown.

1.1 Carolina Cuspate Forelands

The coast of the southeastern United States is made up of a series of gigantic cusps and associated shoal complexes, named the cuspate foreland. The cuspate forelands along the Carolina coasts, shown in Figure 1, are large-scale shoreline promontories that are separated by more than 100 km with underwater, seaward projecting shoals that extend over 10 km from the cape (McNinch and Wells, 1999). The formation of these well-developed coastal features has been studied for more than 100 years (Theiler and Ashton, 2011), but remains largely unknown.

However, several theories have been made about the maintenance of the cuspate foreland and shoal complexes for the Carolina coast, specifically for Cape Lookout, mapped in Figure 1. McNinch and Wells (1999) show that the sediment deposited along the shoal is due to longshore drift from the adjacent barrier beach. The shoal, which actively deposits new sediment down its entire length, has significant sediment volumetric fluctuations for short-term events, such as storms, but maintains its morphology over the long term due to persistent accretion. This causes the shoal to act as a sediment sink, limiting the sediment budget available for exchange between the adjacent shorelines.

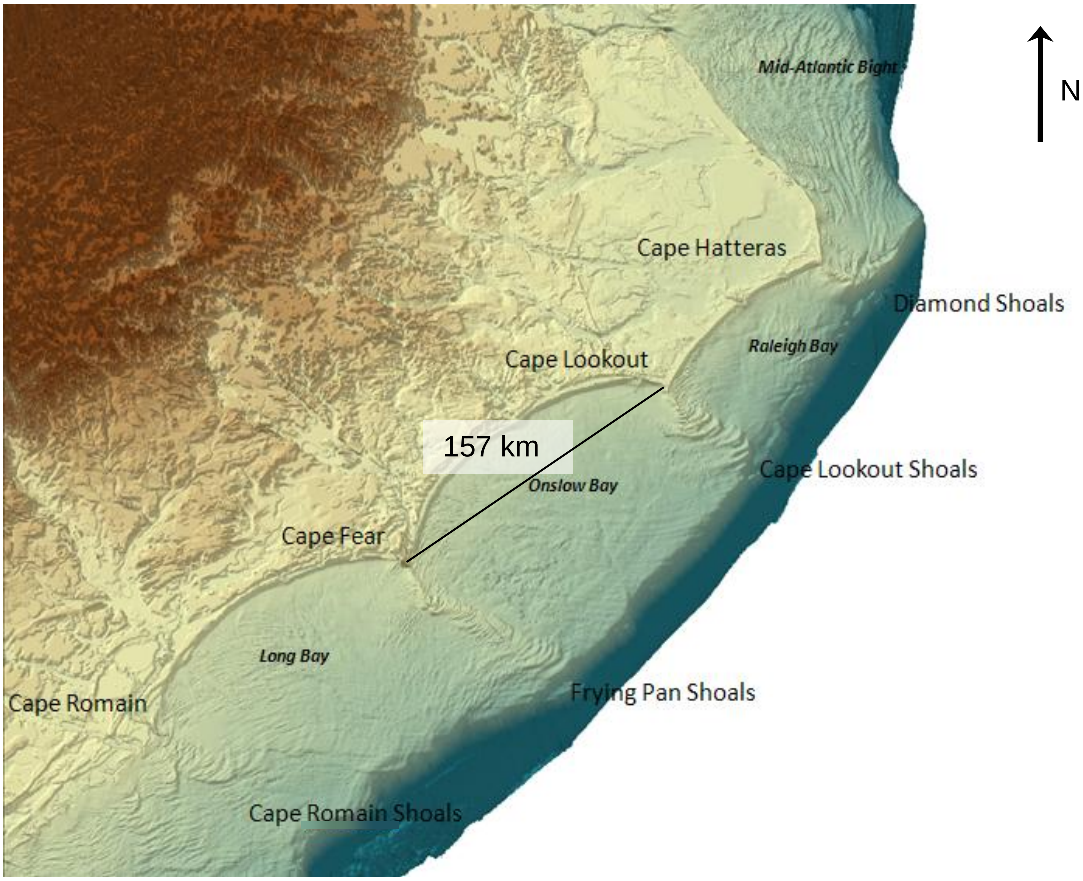

Figure 1: Map of the cuspate forelands along the Carolina coast.

McNinch and Luettich (2000) investigated the physical processes responsible for the sediment transport to Cape Lookout Shoals, and showed that tidal and wave-driven currents continually supply sediment to the shoal such that its morphology is maintained. These currents were modeled by Park and Wells (2005) using the refraction/diffraction modeling system, REF/DIF-1, and show that longshore sediment transport driven by currents are highly dependent on the angle of incidence of incoming waves. The shoal is also seen to cause a sheltering effect between the east and west sides, such that the two sides of the shoal experience completely different wave conditions, depending on the wave angle of incidence, which greatly affects the rates of sediment transport (Park and Wells, 2007).

The sheltering effect observed at Cape Lookout is also evident at the study area for this research, Cape Hatteras. An example of this is shown in Figure 2, where waves are approaching from the southeast toward the southward facing coast located on the left side of Cape Hatteras Point in this photograph. The north coast, located on the right side of the point in Figure 2, is completely sheltered from the southeasterly waves because the waves dissipate their energy through wave breaking along the shoal. Although this sheltering effect greatly affects the sediment transport at Cape Lookout (Park and Wells, 2005), there is a lack of data to support the same conclusion at Cape Hatteras (List et al., 2011).

Therefore, the United States Geological Survey (USGS) conducted a beach erosion study at Cape Hatteras, North Carolina in February 2010 as part of the Carolina Coastal Change Processes Project. The purpose of this project is to investigate the interactions of shoreline, nearshore and offshore sediment transport processes that drive the coastal change in the Carolinas. Specifically, the study at Cape Hatteras focuses on the processes responsible for longshore sediment transport to the cape's point and further offshore (List et al. 2011). The basic mechanism that drives longshore sediment transport is longshore currents, which can be caused by several different processes.

Figure 2: Aerial photograph of Cape Hatteras with waves approaching from the southeast on February 16, 2010.

1.2 Longshore Currents

The excess momentum flux due to waves was first defined as radiation stress by Longuet-Higgins and Stewart (1964). The principal shoreward component of the radiation stress, S_{xx}, consists of contributions from changes in pressure and momentum flux due to the presence of waves. When waves approach the shoreline obliquely, a longshore component of the radiation stress forcing, S_{xy}, is exerted parallel to the shore (Thornton, 1970 and Longuet-Higgins, 1970a,b). Longshore currents are generated as a result of the longshore momentum balance between the gradients in the longshore component of radiation stress, the bottom shear stress and mixing due to internal shear stresses (Bowen, 1969, Thornton, 1970 and Longuet-Higgins, 1970a,b).

However, another mechanism for forcing longshore currents that can be equally as important as the radiation stress gradient forcing was shown by some early studies (Gourlay, 1976, Keeley and Bowen, 1977, Mei and Liu, 1977, and Wu et al., 1985) to be the longshore pressure gradient force. A longshore pressure gradient is caused by longshore variations in mean water level which result from non-uniformities in the bathymetry (Putrevu et al., 1995). The mean water level variation can be a result of wave focusing due to non-uniformities in offshore bathymetry (Benedet and List, 2008, Apotsos et al., 2008, List et al., 2009 and Shi et al., 2011) or from variations in wave set-up from breaking waves due to variations in bathymetry within the surfzone (Putrevu et al., 1995, Haas et al., 2002, and Haller et al., 2002). Since Cape Hatteras and Diamond Shoals have significant non-uniformities in the surrounding bathymetry, pressure gradients are likely present due to these processes.

1.2.1 Pressure Gradients due to Wave Focusing

The first mechanism is explained by the process of refraction. As waves propagate shoreward, they refract to become more shore-normal. In the presence of longshore variations in the offshore bathymetric features, refraction causes areas of wave focusing and defocusing along the shore. Areas of wave focusing have higher wave heights compared to areas of defocusing, which causes a larger gradient in the cross-shore radiation stress at breaking, which is balanced by a larger cross-shore pressure gradient, resulting in a higher wave setup. The area of higher wave setup, when situated next to an area of lower wave set-up associated with an area of defocused waves, generates a longshore pressure gradient.

Recent studies have been conducted to further the understanding of the effects and importance of wave focusing on longshore pressure gradients, longshore currents, and sediment transport. For example, Benedet and List (2008) evaluated the effects of longshore non-uniformities from offshore dredge pits using a numerical modeling approach. Delft3D, a process-based model containing several modules that control physical processes to simulate wave transformation, nearshore currents, sediment transport and morphological change, was used. The simulations showed that longshore variations in bathymetry from the dredge pits cause wave focusing to occur shoreward on either side of the pits. The pressure gradient induced by the variation in water level greatly affects the flow, decelerating it when the pressure gradient component of the flow opposes the radiation stress-driven component and accelerating it when the two forces act in the same direction. While the decelerating flow causes deposition of sediments, or accretion at the shoreline, the accelerating flow transports sediment, causing an erosional hot spot at the shoreline.

A similar study was conducted by Apotsos et al. (2008) near La Jolla, CA. They evaluated the effects of a longshore-variable wave field induced by an offshore submarine canyon. Similar to the dredge pits in Benedet and List (2008), the bathymetric variability in the canyon structure causes wave focusing and defocusing, which leads to longshore variability in the cross-shore momentum balance resulting in pressure gradient-driven flows. The nearshore experiment described in Apotsos et al. (2008) was conducted over a 450 m longshore distance, with wave setup variations of nearly 0.1 m. Comparing data collected by in situ instruments at several longshore locations with numerical simulations, it was shown that longshore currents driven by radiation stress forcing alone yields currents opposite in direction from measured currents. Including the longshore pressure gradient forcing induced by variations in setup yields currents similar in magnitude and direction of the measured currents and suggests that the pressure gradient forcing alone can drive currents up to 2 m/s for the study area considered.

To determine the importance of the longshore pressure gradients on the currents and relate them to sediment transport, List et al. (2009) used a numerical modeling approach to analyze momentum balances. Using Delft3D and idealized model bathymetry of a localized area of deep water offshore, the longshore pressure gradient forcing term, caused by longshore variations in wave height and setup, was shown to be the dominant process controlling the longshore variations of the flow accelerations. The bottom shear stress responds to the sum of the pressure gradient and radiation stress forcing, increasing in magnitude as the forcing increases. Similar to Benedet and List (2008) and Apotsos et al. (2008), the longshore pressure gradient forcing term is the dominating term controlling the longshore varying acceleration term, which results in the longshore sediment transport gradient causing areas of erosion and accretion as the flow accelerates and decelerates.

The effects of accelerations are determined in a most recent study by Shi et al. (2011) by comparing field experiment data from Ocean Beach, California to simulations of waves and currents from the Nearshore Community Model. The simulations show wave focusing caused by an ebb-tidal shoal, which, as shown by the previous case studies, causes a longshore pressure gradient between the area of larger wave heights and the area with smaller wave heights. In the inner and middle surfzones, the longshore momentum balance is seen to be predominately between the pressure gradient forcing, which is significantly larger than the radiation stress forcing, and the bottom friction term. The resulting convective accelerations complete the momentum balance and have the same order of magnitude as the radiation stress forcing.

1.2.2 Pressure Gradients due to Variability in Wave Breaking

Erosion and accretion processes are also present on beaches with longshore uniform offshore bathymetry. Therefore, a second mechanism for generating longshore pressure gradients is considered. Under the circumstances of longshore non-uniformities within the surfzone, longshore variations in wave breaking generate longshore pressure gradients, as opposed to the previous case where wave focusing causes the additional forcing. Because the offshore bathymetry is uniform, the waves shoal and refract uniformly. When the waves enter a surfzone with non-uniform bathymetry, a longshore pressure gradient is generated when waves break over shallow bathymetry that is situated next to an area of deeper bathymetry over which waves do not break. The wave setup from the breaking waves is more than the wave setup from the nonbreaking waves. Therefore, a longshore pressure gradient is generated from the area of more wave breaking (shallower bathymetry and larger wave setup) to the area of less wave breaking (deeper bathymetry and smaller wave setup).

Historically, this type of longshore pressure gradient driven flow has been associated with rip currents, or strong offshore directed flows, since they originate within the surfzone and are caused by longshore variations in incident wave height. Dalrymple (1978) considered the case of a barred beach with periodic rip channel openings and normally incident breaking waves. The longshore pressure gradient is induced by a larger setup of water where waves are breaking on the bar and drives a substantial longshore current in the trough between the shoreline and the longshore bar to the rip channel, where wave setup is less because waves do not break.

Putrevu et al. (1995) expanded upon Dalrymple (1978) by assuming longshore non-uniformities localized to the surfzone and obliquely incident waves. By neglecting the acceleration term and conducting a series of one-dimensional calculations to determine mean cross-shore current, setup, and wave height, the longshore pressure gradient is determined and superimposed in the longshore momentum equation as an additional forcing term. In agreement with Dalrymple (1978), Putrevu et al. (1995) shows that a relatively small longshore pressure gradient (0.015 m setup variation over a longshore distance of 90 m) accounts for nearly half of the longshore current forcing when waves have a small angle of incidence (10°), causing the longshore current to deviate ±30%.

The importance of longshore currents driven by pressure gradients within a rip current system is also shown by Haas et al. (2002). Comparing numerical model simulations to data collected from in situ instruments (including longshore pressure gradient measurements), it is shown that increased wave breaking over a longshore bar causes larger wave setup, inducing a longshore pressure gradient in the trough. The longshore current driven by the pressure gradient is substantial and acts as a “feeder” current for the rip current system. When the tide is high and waves do not break over the longshore bar, the longshore pressure gradient is not induced and the rip current is very weak. This implies that the radiation stress forcing alone is too weak to feed the rip current system and the pressure gradient driven flow is the dominating feeder current.

Haller et al. (2002) shows through a set of laboratory experiments that the feeder currents are due largely to longshore pressure gradient induced flows. The location of the longshore currents, which is in the trough between the shoreline and the longshore bar, is shifted shoreward due to the presence of the longshore pressure gradient, while the current magnitude is dependent on the longshore variability of wave height and water depth. Haller et al. (2002) also relates the rip current system to sediment transport, where the magnitude and direction of transport is due to the rip current which alters the circulation of water within the surfzone.

Based on these previous studies, longshore currents and sediment transport can be driven by longshore pressure gradients due to non-uniformities in nearshore bathymetry. For offshore non-uniformities, wave focusing and defocusing cause a longshore pressure gradient from the area of higher wave setup from focused waves to the area of lower wave setup from defocused waves. However, for bathymetric variations in the surfzone, longshore variations in wave breaking cause areas of higher wave setup to be situated next to areas of lower wave setup, driving a longshore pressure gradient. Both of these processes cause a pressure gradient-driven component to the longshore currents and is shown in several studies to be imperative to include for accurately quantifying current magnitudes and direction. In addition to the longshore current velocities, the accelerations of the flow induced by the additional pressure gradient forcing drives sediment transport, such that accelerating flow causes erosion and decelerating flow causes accretion.

Although the longshore pressure gradient forcing is important for estimating currents and sediment transport, field measurements of longshore pressure gradients are extremely difficult to obtain (Nielsen et al., 2001). Because very small differences in mean water level (O(0.01 m)), can drive substantial currents (O(1 m/s)), such small differences are typically within the accuracy to which pressure sensors can measure pressure variations. The measurements are also affected by sediment movement, such as scouring around the instrument base, which changes the vertical position of the instrument and causes biased pressure measurements. It is also critical that the relative cross-shore position of the pressure sensors be exactly the same so that the pressure gradient being measured is the longshore pressure gradient and not a result of a difference in cross-shore position (Nielsen, 1999).

Lastly, the effects of the convective accelerations on the flow remain unclear. In the previous studies, the distance over which the pressure gradient acts is relatively large and the longshore momentum balance is between the acceleration, radiation stress gradient, pressure gradient, and bottom stress terms. The bottom shear stress has acted as a stabilizer and limiter of the flow accelerations because it has been in a fully developed state. However, for conditions with a relatively large pressure gradient acting over a small distance, the bottom shear stress may not have reached an equilibrium state. Therefore, it is important to evaluate the effects of the accelerations on the flow for a small domain by analyzing the full longshore momentum balance.

1.3 Coastal Video Observations

One of the tools used for observing the processes for driving longshore currents and sediment transport at Cape Hatteras is video imagery. Although pressure gradients cannot be determined directly from the video, the presence of a longshore pressure gradient driving the current can be inferred by the location of the currents, which are shifted shoreward in the presence of a pressure gradient on a bar/trough beach profile.

The bathymetry of the study area is also observed using the statistical video images by noting variability in the breaking patterns. Non-uniformities in the bathymetry are identified by associating deeper depths to areas with less wave breaking and shallower depths to areas with more breaking. The mechanisms that produce a pressure gradient are investigated by the locations of these non-uniformities, such that offshore bathymetric variability causes wave focusing and defocusing and surfzone bathymetric variability causes variability in wave breaking.

1.3.1 Video Estimates of Longshore Currents

Due to the high cost and difficulty of deploying in situ instruments to conduct measurements of nearshore processes, remote sensing techniques have become desirable to use for long-term monitoring, especially in dynamic nearshore environments. One of these techniques is an optically based method that measures surface longshore currents. By using images taken from a video camera that records the littoral zone and offshore area, Chickadel et al. (2003) developed a method that tracks advected residual sea foam from breaking waves down the coast. Using an Optical Current Meter (OCM) technique, the time-space characteristics of foam traces along a longshore array of pixels in the surfzone is used to calculate a two-dimensional frequency-wavenumber spectrum. This is transformed into a wavenumber-velocity spectrum, then integrated to obtain a velocity spectrum, which is used to estimate a single most representative velocity. When compared to synthetic data, the longshore currents estimated with OCM have a maximum root mean square (RMS) error of 0.033 m/s for velocities up to 1 m/s indicating good agreement.

The OCM technique is used in another study described by Haas and Cambazoglu (2006) to estimate longshore currents from video collected at Myrtle Beach, SC. Comparing the video estimated currents to currents measured by an in situ instrument, the general magnitude and low-frequency variations are very similar, but the infragravity portion of the current varies significantly. However, the cross-shore variation of the hourly averaged, video-estimated currents clearly shows an increase in current magnitudes as the angle of incidence of breaking waves increases and a seaward shift of the currents as tides fall.

Perkovic et al. (2009) also used video-based remote sensing to estimate longshore currents at Black’s Beach near La Jolla, CA. Using particle image velocimetry (PIV) techniques, the surface currents are estimated by comparing two successive frames. Assuming that advection of surface foam is optically visible in the video frames, a motion estimation processor (MEP) is used to track pixel intensities from one frame to the next. The currents estimated with MEP, which have a magnitude up to 1.5 m/s, are compared to currents measured with radar, showing good agreement with a RMS error of 0.05 m/s.

Although the studies that have been conducted using optically based remote sensing techniques are limited, they have shown to have good agreement with synthetic data (Chickadel et al., 2003) and with radar based remote sensing techniques (Perkovic et al., 2009). However, the robustness of current estimates made using video imagery can be improved with additional data comparisons from nearshore studies, including in situ instrument measurements.

1.3.2 Bathymetric Variability Using Image Statistics

Since bathymetry data is often very limited and greatly needed in nearshore studies, remote sensing techniques have also been used to determine morphology using image statistics. The morphology of a sand bar using video imagery was first determined by Lippmann and Holman (1989) who used long time-exposure images of the nearshore region at Duck, NC to provide a statistically stable image of the wave breaking patterns. Using data collected during the 1986 nearshore study, SUPERDUCK, a random wave model is used to calculate wave parameters, including dissipation. By assuming that the bright pixel intensities vary with wave dissipation, the presence of an offshore sand bar is shown most clearly when waves are small enough to just break over the bar. When waves are large, the maximum pixel intensities are located shoreward of the location of maximum wave dissipation. However, video imagery is shown to be very useful in determining the presence of a bar system without conducting any bathymetric surveys.

A technique was developed by Stockdon and Holman (2000) to quantitatively estimate bar morphology at Duck during a field experiment in October 1997. Representing the cross-shore structure of Fourier transformed pixel intensities by the first complex empirical orthogonal function (CEOF) mode, the wavenumber is calculated and used to estimate water depth. For October 14, 1997, the daily averaged bathymetric profile, obtained by averaging the hourly estimates of water depth, which varied with changing lighting conditions, tide level, and wave conditions, is compared to survey data. Although the general trend of the estimated depth was similar to the survey data, the estimated bathymetry was shown to be much less accurate than survey data with a maximum RMS error of nearly 1 m.

The relationship between offshore bar migration and annual cycles of wave height was investigated by Alexander and Holman (2004) using video imaging. Although no quantitative analysis is presented, three images are extracted at high, mid, and low tide stages from each site and are compared to hourly averaged wave conditions corresponding to the site and time that the images were taken. By specifying a viewing window in the images from each site, the shoreward-biased locations of the sand bars that result from lack of wave breaking are removed. The locations of the sand bars are then cross-correlated to wave height and show, at every site, an offshore migration of the bar during larger waves. For a beach with multiple bars, the annual signal and correlations of the outer bar locations with wave height data are stronger than the innermost bar and show an increase in spacing between bars with larger wave heights.

A recent study by Guedes et al. (2011) compares the use of averaged images and variance images from Cassino Beach, Brazil to estimate the locations of offshore bars and wave energy dissipation. These estimates are compared to bathymetry data, in situ wave data, and wave model results and show that the bar location estimated from average images to be closer to actual bar location than estimated from variance images. The main hydrodynamic variable in estimating the bar location for either type of image is shown to be wave height, with smaller waves that just break over the bar estimating the bar location most accurately. However, the location of wave energy dissipation is dependent on the type of image used, with the variance image providing estimates closer to the modeled dissipation location than the average image.

Clearly, optically-based remote sensing techniques provide a qualitative analysis of bathymetry, although a robust method for calculating detailed features and exact locations of the bar has yet to be created. Keen et al. (2012) is developing a method for quantitatively estimating wave energy dissipation from video by relating dissipation to fraction of wave breaking, although results from this analysis are still premature.

However, video images are still very useful for determining large-scale features, such as offshore bars, breaks in the bar system, and their general locations. Also, breaking patterns observed in the images are used to estimate the locations of persistently breaking waves and the relative amount of energy dissipation from wave breaking for a given data set.

1.4 Present Work

The focus of the present study is to develop a better understanding of the relationships between radiation stress and pressure gradient forcing the longshore currents and sediment transport at Cape Hatteras, NC. Using video images that were collected during a beach erosion study in February 2010, the OCM technique is used to estimate longshore currents. The resulting currents are also compared to wind and wave conditions to determine the effect of changing parameters, such as wave height, water depth and angle of incidence of incoming waves. Morphology and breaking wave patterns are observed using image statistics and are used to determine longshore non-uniformities in bathymetry or variability in wave breaking, which could indicate the presence of a longshore pressure gradient. Lastly, a numerical model is used to simulate longshore currents to develop a better understanding of the mechanisms that drive the currents observed by the video.

CHAPTER 2

METHODOLOGY

As part of the USGS Coastal Change Processes Project, a field experiment was conducted in February 2010 at Cape Hatteras, North Carolina (CH2010). Several types of instruments were utilized to collect data which is being used to quantify the hydrodynamic processes on the proximal part of Diamond Shoals and the adjacent coasts. The data collected from a lighthouse camera is described in detail. Then, post-processing procedures on the acquired video are discussed so that it may be used for estimating physical parameters of interest.

2.1 Overview of Data Collection

To test the hypotheses related to Diamond Shoals as a sink in the regional sediment budget and to provide data for evaluating numerical models, the nearshore hydrodynamics of Diamond Shoals and the adjacent coast were measured using several types of in situ and remote sensing instruments. These instruments and the parameters they measure are described in detail in List et al. (2011). Table 1 lists the instrument types that were used, the site name and location of each instrument as shown in Figure 3, and dates of actively recording data during CH2010.

Nearshore hydrodynamic measurements were obtained using Nortek Aquadopp current meters (Aquadopp) and Teledyne RDI Workhorse Acoustic Doppler Current Profilers (ADCP). These were mounted to 4 m long, aluminum poles and jetted into the seafloor using a Light Amphibious Resupply Cargo (LARC) vessel. The near-bed pressure and the three-dimensional (3D) vertical structure of the currents on the north and south sides of the cape (eastward and southern facing coast, respectively, as shown in Figure 3) were measured continuously at 1 Hz in 0.4 m bins from 0.4 m above the seafloor to the surface. Site N13, located on the south side of the cape (Figure 3), featured an Aquatec AQUAscat Acoustic Backscatter Sensor (ABS) to measure sediment concentration using 0.1 m resolution and a Sontek – YSI Triton Acoustic Doppler Velocimeter (ADV) to measure currents at a single elevation within the water column.

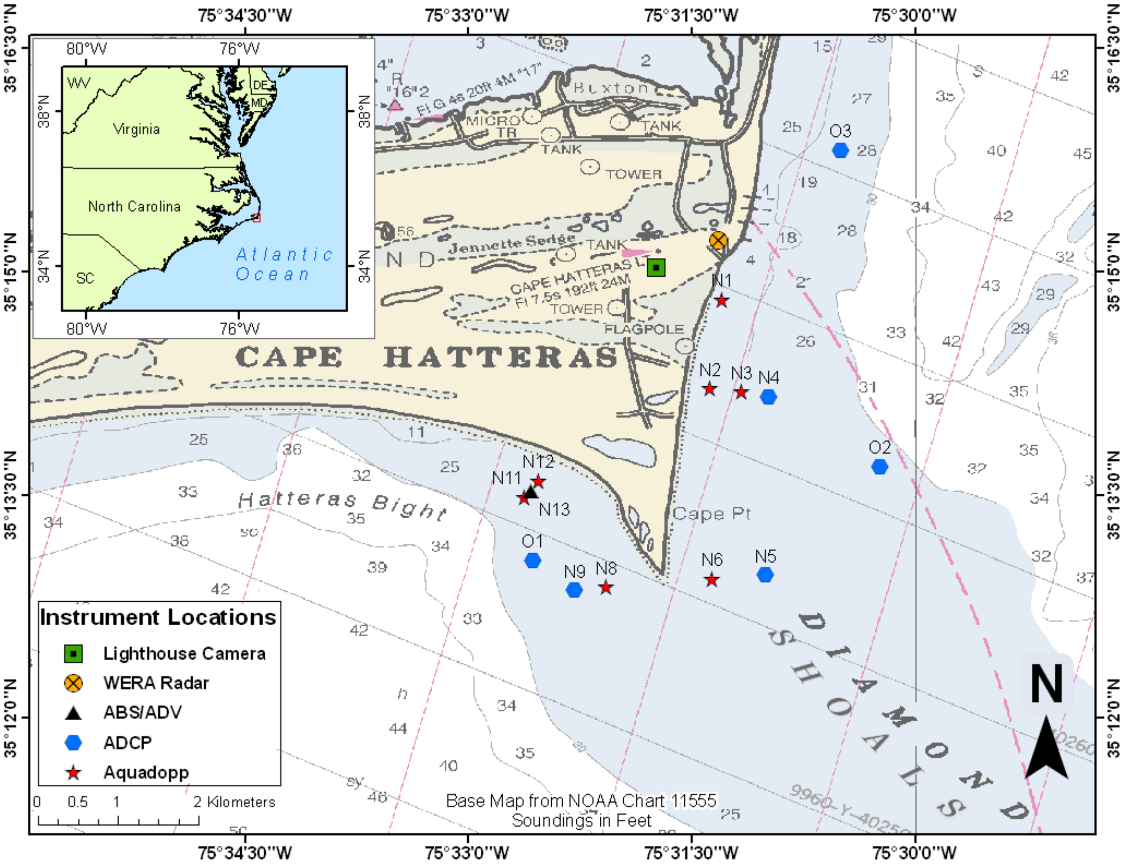

Figure 3: Instrument locations during CH2010.

Table 1: The types, names, locations, and dates of data for instruments used in CH2010.

Type	Name	Longitude W (deg)	Latitude N (deg)	Nominal Water Depth (m)	Dates (2010)
Aquadopp	N1	75.5216	35.2469	3.9	Feb. 9 – 21
	N2	75.5230	35.2369	6.0	Feb. 9 – 21
	N3	75.5193	35.2365	4.9	Feb. 9 – 22
	N6	75.5227	35.2156	4.7	Feb. 2 – 21
	N8	75.5345	35.2147	4.8	Feb. 4 – 22
	N11	75.5437	35.2247	4.9	Feb. 3 – 22
	N12	75.5421	35.2266	2.9	Feb. 3 – 22
ADCP	N4	75.5164	35.2360	7.8	Feb. 9 – 22
	N5	75.5167	35.2160	7.1	Feb. 2 – 21
	N9	75.5381	35.2143	7.0	Feb. 4 – 22
	O1	75.5427	35.2177	9.4	Feb. 4 – Mar. 20
	O2	75.5039	35.2282	9.8	Feb. 4 – Mar. 20
	O3	75.5083	35.2636	9.4	Feb. 4 – Mar. 20
ABS/ADV	N13	75.5430	35.2254	3.5	Feb. 8 – 22
CLARIS	CLARIS	mobile	mobile	remote sensing	Feb. 4, Feb. 6, Mar. 3
LARC	LARC	mobile	mobile	amphibious surveying	Feb. 12, Feb. 20, Feb. 21
WERA Radar	WERA	75.5220	35.2536	remote sensing	Feb. 3 – 25
Lighthouse Camera	Camera	75.5290	35.2505	remote sensing	Feb. 2 – 21

In addition to in situ instruments, several remote sensing techniques were used to measure beach morphology, bathymetry, surface currents, and wave breaking intensity. The Coastal Lidar and Radar Imaging System (CLARIS) is a vehicle-based coastal surveying tool that measures topography, breaking wave intensity, wave direction, and estimates bathymetry by inverting the linear dispersion relationship to solve for depth from wave celerity observations.

To directly obtain bathymetric data, a 200 kHz echo sounder mounted to the LARC was used to collect single-beam bathymetry over Diamond Shoals and the adjacent coast. A composite image, shown in Figure 4, is formed from data collected on February 12, 20, and 21, consisting of tracklines approximately 300 m apart extending about 2 km offshore, 4 km along the coast north and 2 km along the coast west of Cape Hatteras Point. It is clearly seen that a sand bar exists along the north side of the cape.

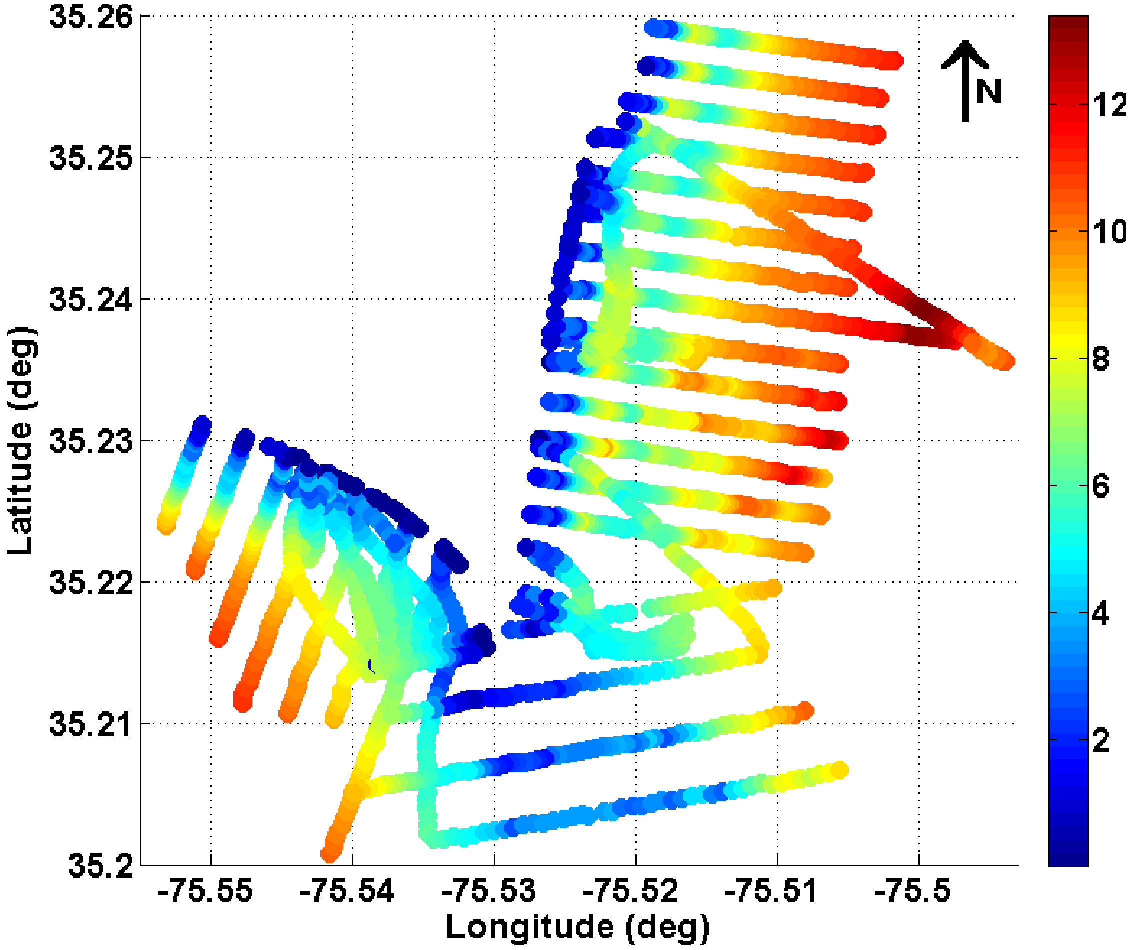

Figure 4: Bathymetric data obtained from the LARC surveys where the scale is the mean water depth (m).

A Helzel Messtechnik GmbH 48MHz Wellen Radar (WERA) station was used to quantify the regional field of surface currents and wave characteristics. Four transmitting arrays emitted electromagnetic (EM) waves along the conductive sea surface every 30 minutes for a continuous period of 17.7 minutes. The signal is backscattered from the surface ocean waves with wavelength equal to half of the emitted EM wavelength and received by twelve receiving arrays. Using a direction-finding algorithm, radial currents are estimated with a spatial resolution of 150 m over an area spanning 120 degrees from the WERA station site, with a varying range of 10 to 15 km.

Lastly, video observations were collected near instrument N1 using a camera system set up on the railing of the Cape Hatteras Lighthouse. A custom camera mount was fabricated and securely attached to the Lighthouse railing, as shown in Figure 5, with the camera in a weather resistant housing. The mount was made of wood, steel, and aluminum and was designed to fit within the dimensions of the bottom horizontal railing. It caused no damage to any part of the historic structure, allowed pan and tilt capabilities, was weather resistant, and minimized movement, including vibrations, except when strong winds shook the entire lighthouse.

Figure 5: Camera securely attached to the railing of the Cape Hatteras Lighthouse using a custom fabricated mount.

A Photron Fastcam with a pixel resolution of 1024 width by 1024 height and a Nikon 80-200mm lens was used to record a 100 m longshore section of the nearshore region near instrument N1. A 3.3 Hz frame rate was used to digitally record six minute bursts continuously each day, where the number of bursts depended heavily on weather conditions. The start time in Greenwich Mean Time (GMT) of the first and last bursts for each day is given in Table 2, with the total number of bursts recorded for that day also listed. On sunny days, such as February 2, 3, 11, 12, and 14 – 21, fewer bursts were recorded since the eastward facing camera was overexposed from sunrise until mid-morning; otherwise, recording began at sunrise. Prior to recording each day, the iris was adjusted based on the weather forecast for that day so that the amount of useable video was optimized. As lighting conditions changed throughout the day, the sensitivity setting, which is analogous to the camera's iris, was adjusted in the Photron Fastcam viewer program used to control the quality of camera recordings.

Table 2: Start time of first and last bursts given in GMT and total number of bursts recorded for each day.

Date (Feb. 2010)	Start (GMT)	End (GMT)	Total Bursts
2	15:35:59	20:06:25	46
3	19:26:26	22:08:41	28
4	13:16:52	22:11:44	90
5	13:31:38	22:04:47	85
6	13:55:34	22:20:34	85
7	13:46:13	22:29:24	88
8	12:26:46	22:21:52	100
9	12:44:28	22:03:30	94
10	13:18:52	22:14:18	90
11	15:21:45	22:16:52	70
12	15:21:00	21:58:14	67
13	13:24:31	22:07:45	88
14	15:13:13	22:08:06	70
15	15:31:16	21:56:35	65
16	15:24:32	22:19:31	70
17	15:21:23	22:16:14	70
18	15:25:28	22:20:46	70
19	15:17:43	22:12:32	70
20	15:24:28	22:19:22	70
21	15:20:35	22:15:21	70

2.2 Video Rectification

Several steps are involved in processing the video data so that the images can be used effectively to estimate physical parameters. The first step is that the images must be rectified, or transformed from a coordinate system in pixels to a coordinate system in meters described below.

2.2.1 Survey Data in a Local Coordinate System

To provide the most accurate data for rectifying the video recordings, daily surveys were conducted of semi-permanently anchored aerial targets on the beach in view of the camera, circled in red in Figure 6. In addition to the six stationary targets, fifteen roving targets, one of which is circled in blue in Figure 6, were surveyed using a survey-grade, Ashtech Z-12, dual-frequency Global Positioning System (GPS). Therefore, each day has a total of twenty-one ground control points to be used for processing the video data. A GPS base station was set up on a platform near the survey area, to provide data from a fixed point for post-processing of the GPS data acquired by the roving receiver. All GPS data are post-processed with GraphNav software with the locations given in Universal Transverse Mercator (UTM) Zone 18 coordinate system.

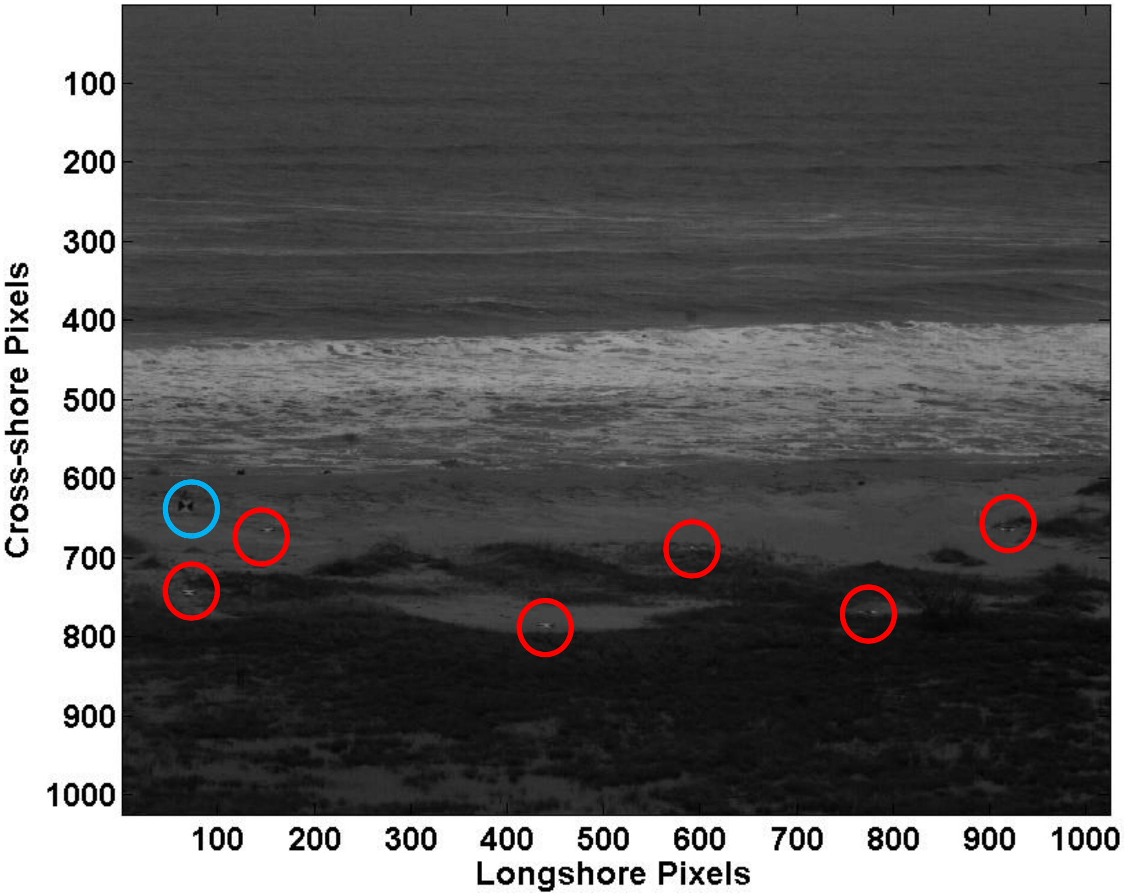

Figure 6: Camera view of six stationary targets (red) and one roving target (blue).

The survey data are translated to a local coordinate system with the origin located on the beach. The entire coordinate system is rotated seven degrees counter-clockwise, such that the shoreline is aligned in the y-direction. The scaled and rotated topographic survey from February 3 is plotted in Figure 7 where the elevation is in meters with the mean tidal level defined at z=0. The daily surveys of the targets are also scaled and rotated to obtain the data in the local coordinate system.

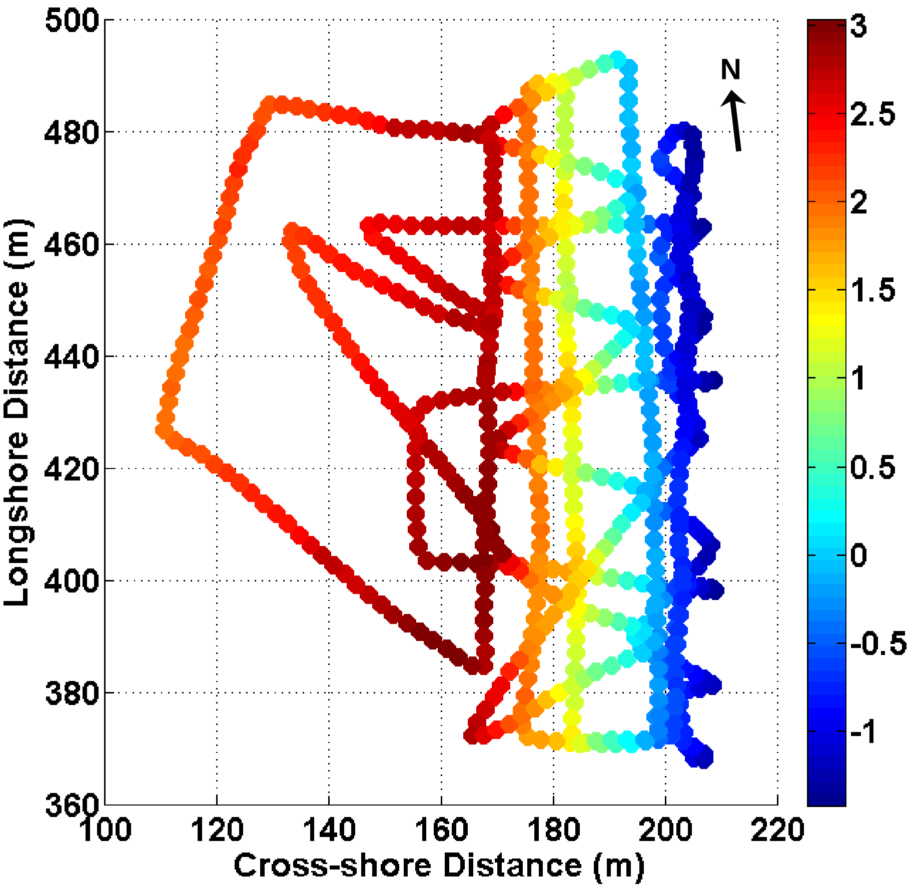

Figure 7: Scaled and rotated topographic survey conducted on February 3, 2010 where warmer colors indicate higher elevation (m) above the mean tidal level at z=0.

2.2.2 Rectification Using Intrinsic and Extrinsic Camera Properties

To quantify physical parameters from the video, the images must first be translated to a real-world coordinate system. Direct linear transformation (DLT) coefficients are used to represent combinations of intrinsic and extrinsic parameters that allow the projection of real-world coordinates to image coordinates. The coefficients are found using the DLT equations described by Holland et al. (1997)

$$u = \frac{L_1 x + L_2 y + L_3 z + L_4}{L_9 x + L_{10} y + L_{11} z + 1} \tag{1}$$

and

$$v = \frac{L_5 x + L_6 y + L_7 z + L_8}{L_9 x + L_{10} y + L_{11} z + 1} \tag{2}$$

where (x, y, z) are the real-world coordinates and (u, v) are the image coordinates. The coefficients, which have no physical meaning, are defined as

$$L_1 = (u_o m_{31} - f m_{11})/\lambda_u L \tag{3a}$$

$$L_2 = (u_o m_{32} - f m_{12})/\lambda_u L \tag{3b}$$

$$L_3 = (u_o m_{33} - f m_{13})/\lambda_u L \tag{3c}$$

$$L_4 = -(L_1 x_c + L_2 y_c + L_3 z_c) \tag{3d}$$

$$L_5 = (v_o m_{31} - f m_{21})/\lambda_v L \tag{3e}$$

$$L_6 = (v_o m_{32} - f m_{22})/\lambda_v L \tag{3f}$$

$$L_7 = (v_o m_{33} - f m_{23})/\lambda_v L \tag{3g}$$

$$L_8 = -(L_5 x_c + L_6 y_c + L_7 z_c) \tag{3h}$$

$$L_9 = m_{31}/L \tag{3i}$$

$$L_{10} = m_{32}/L \tag{3j}$$

$$L_{11} = m_{33}/L\,. \tag{3k}$$

L is given by

$$L = -(x_c m_{31} + y_c m_{31} + z_c m_{33}) \tag{4}$$

(u_o, v_o) is the image center, f is the effective focal length, (x_c, y_c, z_c) are the camera coordinates and $m_{i,j}$ are the direction cosines defined as

$$m_{11} = \cos\varphi\cos\sigma + \sin\varphi\cos\tau\sin\sigma \tag{5a}$$

$$m_{12} = -\sin\varphi\cos\sigma + \cos\varphi\cos\tau\sin\sigma \tag{5b}$$

$$m_{13} = \sin\tau\sin\sigma \tag{5c}$$

$$m_{21} = -\cos\varphi\sin\sigma + \sin\varphi\cos\tau\cos\sigma \tag{5d}$$

$$m_{22} = \sin\varphi\sin\sigma + \cos\varphi\cos\tau\cos\sigma \tag{5e}$$

$$m_{23} = \sin\tau\cos\sigma \tag{5f}$$

$$m_{31} = \sin\varphi\sin\tau \tag{5g}$$

$$m_{32} = \cos\varphi\sin\tau \tag{5h}$$

$$m_{31} = -\cos\tau \tag{5i}$$

where τ is the camera tilt, φ is the camera azimuth and σ is the camera roll which are shown in Figure 8.

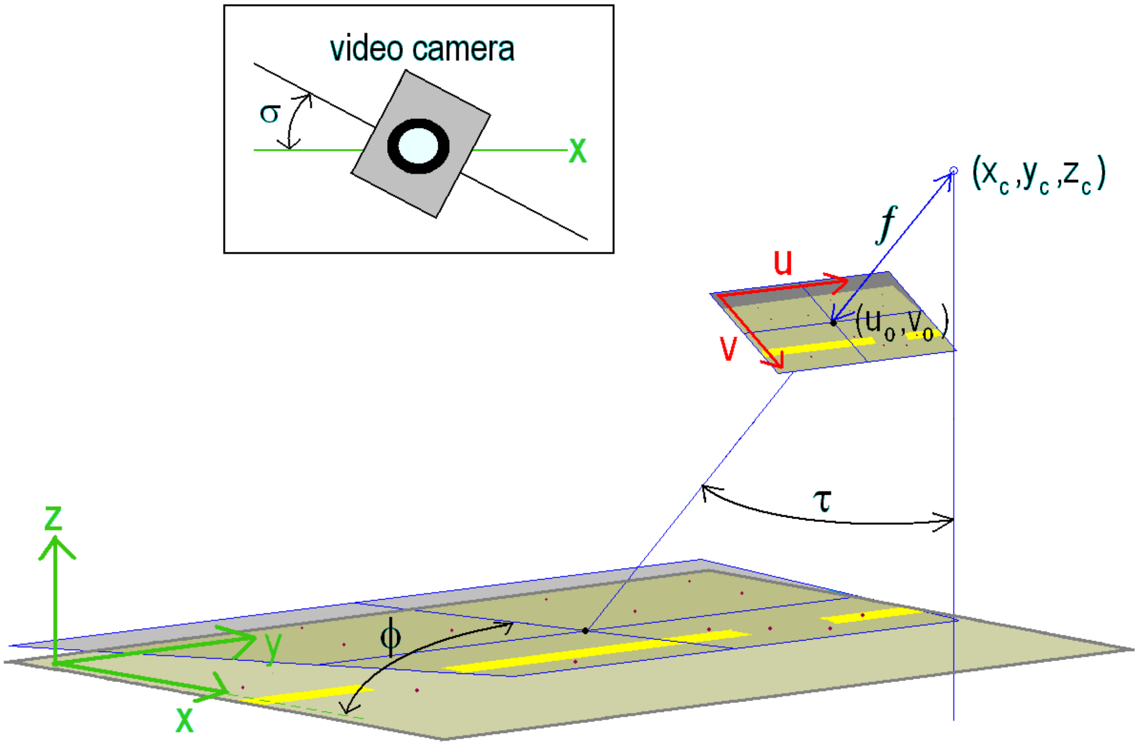

Figure 8: Schematic of the relationship between the image plane, real-world plane, and the video camera showing the rotation angles and focal length.

The image center, (u_o, v_o), is found by following the center of field of view method given by Willson and Shafer (1994). This requires two strings to be stretched from one corner of the video image to the opposite corner, forming an "X" at the center of the field of view. This is done using the same camera system used in CH2010 and the center of the image is determined to be a horizontal pixel distance, u_o, of 512 pixels and a vertical pixel distance, v_o, of 517 pixels.

Calibrations under laboratory conditions are used to correct video images for radial distortion of the camera lens. Following the laboratory calibrations method described by Holland et al. (1997), the same camera system used in CH2010 is used to record a black poster board with uniformly spaced, equal size white dots. The poster is mounted perpendicular to the camera view such that z_c can be assumed to be zero, simplifying the DLT equations. Then, the distorted pixel coordinates of the center of each dot (u_d, v_d) on the raw image is determined by calculating its centroid. To relate u_d and v_d to the known "real-world" location of each dot (x_r, y_r), the constrained, distorted DLT coefficients are found using a system of equations formed by plugging in the real-world coordinates (x_r, y_r) and the pixel coordinates (u_d, v_d) of each dot into Equations (1) and (2) and solved using a least squares solution. The undistorted pixel locations of the centers (u_p, v_p) of the dots are then found using Equations (1) and (2) with the DLT coefficients and the real-world coordinates. The distance from the center of the image to a given distorted pixel location, r, is given by

$$r = \sqrt{(u_d - u_o)^2 + (v_d - v_o)^2} \tag{6}$$

and the pixel displacement due to distortion, Δr, is defined as

$$\Delta r = \sqrt{(u_d - u_o)^2 + (v_d - v_o)^2} - \sqrt{\left(u_p - u_o\right)^2 + \left(v_p - v_o\right)^2}\,. \tag{7}$$

By modeling the radial distortion as the two-coefficient odd-order polynomial

$$\Delta r = k_1 r^3 + k_2 r \tag{8}$$

a best fit solution to Equations (3a-k), shown in Figure 9, is calculated based on the r and Δr observations. The distortion coefficients, k_1 and k_2, determined from the best fit solution are applied to every pixel in raw images to correct for any radial distortion in the camera lens. For the lens used in this study, the distortion coefficients are calculated as $k_1 = 6.05 \times 10^{-9}$ and $k_2 = 1.30 \times 10^{-3}$.

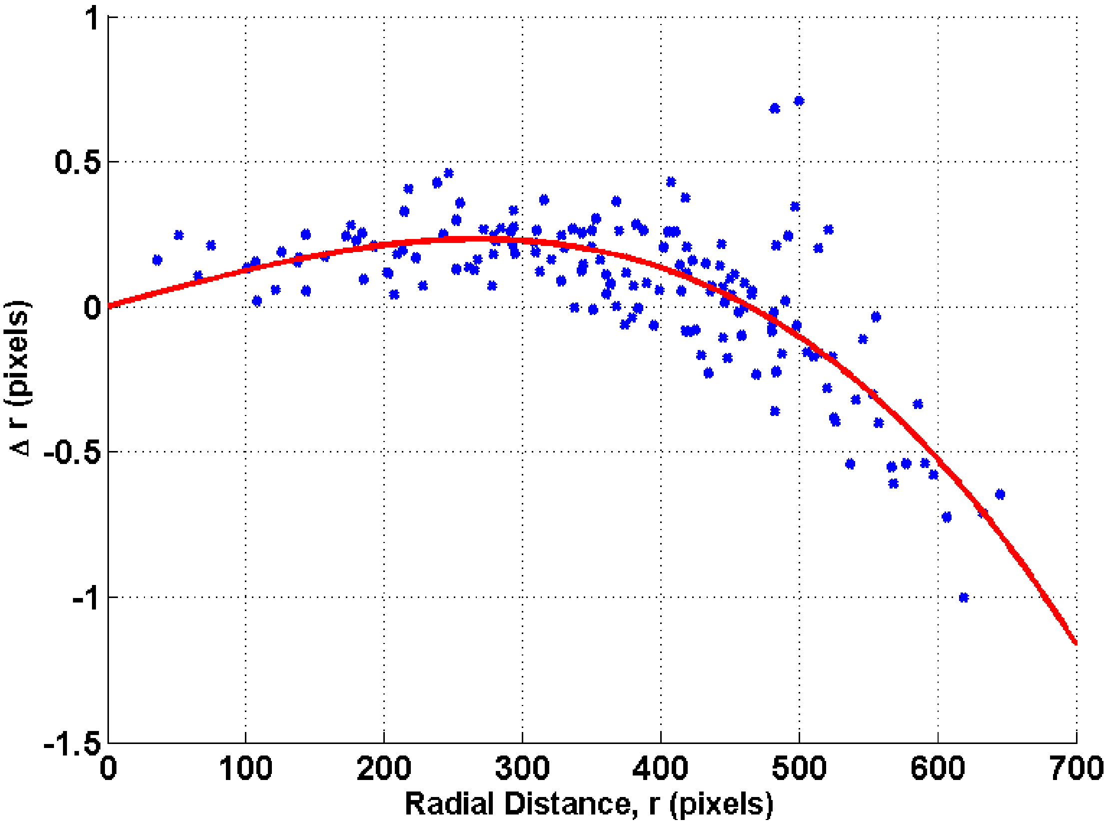

Figure 9: A least-squares fit (red line) to the pixel displacement (blue dots) as a function of radial distance for radial distortion corrections.

Rectified images are created by defining a grid that assumes a horizontal plane for the sea surface and a sloping plane for the beach with a grid spacing of every 0.25 m in the cross-shore and longshore directions. The DLT coefficients are then used to predict a corresponding image coordinate for every grid point created, and the pixel intensity at that point is extracted from the raw video image.

A technique, described in Holland et al. (1997) as the field calibrations method, is used to calculate a set of DLT coefficients. This method is different than the rectification method previously used, described by Haas and Cambazoglu (2006), because higher accuracy is needed in the DLT coefficients for the large camera setback. To obtain higher accuracy, several intrinsic and extrinsic camera properties are specified using this new method, such that only the camera angles, τ, φ and σ, are unknowns.

For every ground control point, two functions, F and G, are written as

$$F(u^*, \varphi, \tau, \sigma, f, x_c, y_c, z_c) = qu^* + of \equiv 0 \tag{9a}$$

$$G(v^*, \varphi, \tau, \sigma, f, x_c, y_c, z_c) = qv^* + pf \equiv 0 \tag{9b}$$

where (u^*, v^*) are the undistorted, scale corrected image coordinates given by

$$u^* = (u - u_o)\lambda_u \tag{10a}$$

$$v^* = (v - v_o)\lambda_v \tag{10b}$$

and

$$q = m_{31}(x - x_c) + m_{32}(y - y_c) + m_{33}(z - z_c) \tag{11a}$$

$$o = m_{11}(x - x_c) + m_{12}(y - y_c) + m_{13}(z - z_c) \tag{11b}$$

$$p = m_{21}(x - x_c) + m_{22}(y - y_c) + m_{23}(z - z_c)\,. \tag{11c}$$

The vertical and horizontal scale factors, λ_v and λ_u which are determined during image acquisition by the computer image frame buffer and control the “squareness” of the pixels, are calculated. The vertical scale factor is assumed to equal a value of one because the rows in the computer frame buffer typically correspond exactly to the scanlines in the video image (Holland et al., 1997). However, the horizontal scale factor is affected by the differences in sampling frequencies between the camera and the image acquisition software and may vary significantly from a value of one. Using the undistorted pixel locations $(u_{p,}v_p)$ of the centers of the dots, λ_u is found by

$$\lambda_u = \frac{\sum_{i=2,j=1}^{m,n}\left(v_p^{i,j} - v_p^{i-1,j}\right)}{\sum_{i=1,j=2}^{m,n}\left(u_p^{i,j} - u_p^{i,j-1}\right)} \tag{12}$$

which is the ratio of the mean vertical pixel distance between adjacent target points within the row m to the mean horizontal pixel distance between adjacent points within the column n. For the camera system and video acquisition software used in this study, λ_u is found to equal 0.9993.

Performing a Taylor Series Expansion on Equations (9a) and (9b) and specifying initial approximations for all parameters to the functions to obtain F_o and G_o, corrections to the unknowns, $\partial\varphi$, $\partial\tau$, and $\partial\sigma$, are determined using a standard iterative minimization technique. The finite approximation of the residual errors of the image coordinates, Δu and Δv, is found by

$$\Delta u - \frac{F_o}{q} = b_{11}\partial\varphi + b_{12}\partial\tau + b_{13}\partial\sigma \tag{13a}$$

$$\Delta v - \frac{G_o}{q} = b_{21}\partial\varphi + b_{22}\partial\tau + b_{23}\partial\sigma \tag{13b}$$

where only the terms that contain the unknown parameters are included and

$$\begin{aligned} b_{11} = {} & \frac{u^*}{q}[(x - x_c)m_{32} - (y - y_c)m_{31}] \\ & + \frac{f}{q}[(x - x_c)m_{12} - (y - y_c)m_{11}] \end{aligned} \tag{14a}$$

$$\begin{aligned} b_{12} = {} & \frac{u^*}{q}[(x - x_c)\cos\tau\sin\varphi + (y - y_c)\cos\varphi\cos\tau + (z - z_c)\sin\tau] \\ & + \frac{f}{q}[-(x - x_c)\sin\varphi\sin\tau\sin\sigma \\ & - (y - y_c)\cos\varphi\sin\tau\sin\sigma + (z - z_c)\cos\tau\sin\sigma] \end{aligned} \tag{14b}$$

$$b_{13} = \frac{f}{q}[(x - x_c)m_{21} + (y - y_c)m_{22} + (z - z_c)m_{23}] \tag{14c}$$

$$\begin{aligned} b_{21} = {} & \frac{v^*}{q}[(x - x_c)m_{32} - (y - y_c)m_{31}] \\ & + \frac{f}{q}[(x - x_c)m_{22} - (y - y_c)m_{21}] \end{aligned} \tag{14d}$$

$$\begin{aligned} b_{22} = {} & \frac{v^*}{q}[(x - x_c)\cos\tau\sin\varphi + (y - y_c)\cos\varphi\cos\tau + (z - z_c)\sin\tau] \\ & + \frac{f}{q}[-(x - x_c)\sin\varphi\sin\tau\sin\sigma \\ & - (y - y_c)\cos\varphi\sin\tau\cos\sigma + (z - z_c)\cos\tau\cos\sigma] \end{aligned} \tag{14e}$$

$$b_{23} = -\frac{f}{q}\left[(x - x_c)m_{11} + (y - y_c)m_{12} + (z - z_c)m_{13}\right]. \tag{14f}$$

Obtaining a solution to Equations (14a-f) in a least-squares sense using every combination of data points yields the corrections to the initial values until the corrections become negligible. The estimates of the unknown angles are determined, and Equations (3a-k), (4) and (5a-i) are used to calculate the DLT coefficients.

For the camera setup used in CH2010, the known parameters are specified as the determined values of u_o, v_o, k_1, k_2, f, λ_v, λ_u, x_c, y_c, z_c given in Table 3 and the initial approximations of the unknowns are $\tau = 80°$, $\varphi = 120°$, and $\sigma = 0°$. Calculating a set of DLT coefficients specific to each day of data collection allows the rectification scheme to use the most accurate set of data points available. This method is seen to be effective to use by comparing the location of the offshore breaking wave in Figure 10 to Figure 11. The offshore breaking wave occurs around 800 m, which is the shallowest location over the offshore bar, indicating that the rectification scheme is predicting relatively accurate real-world locations of the pixel coordinates. The wave appears to be "smeared" because of the assumption that the sea surface is a flat plane.

Table 3: Camera properties and coordinates for the setup used in CH2010.

u_o	512 pixels	λ_v	1
v_o	517 pixels	λ_u	0.9993
k_1	6.05×10^{-9}	x_c	-289.15 m
k_2	1.30×10^{-3}	y_c	671.92 m
f	6.67×10^{3}	z_c	16.16 m

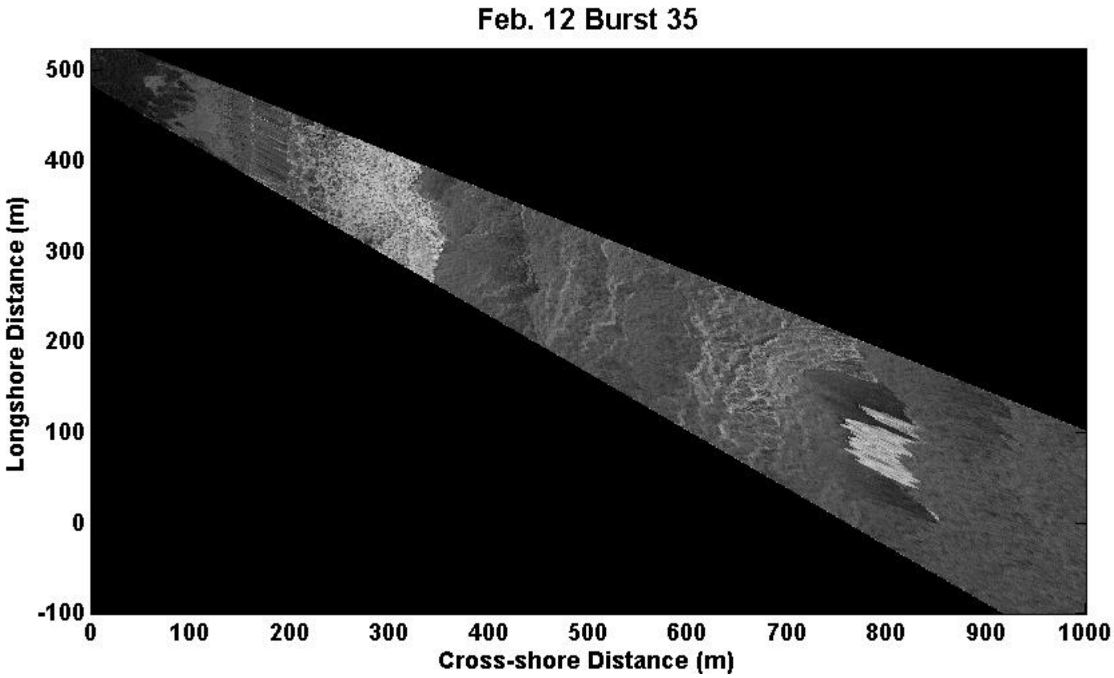

Figure 10: Rectified image using the final scheme from February 12, Burst 35 that shows an offshore breaking wave.

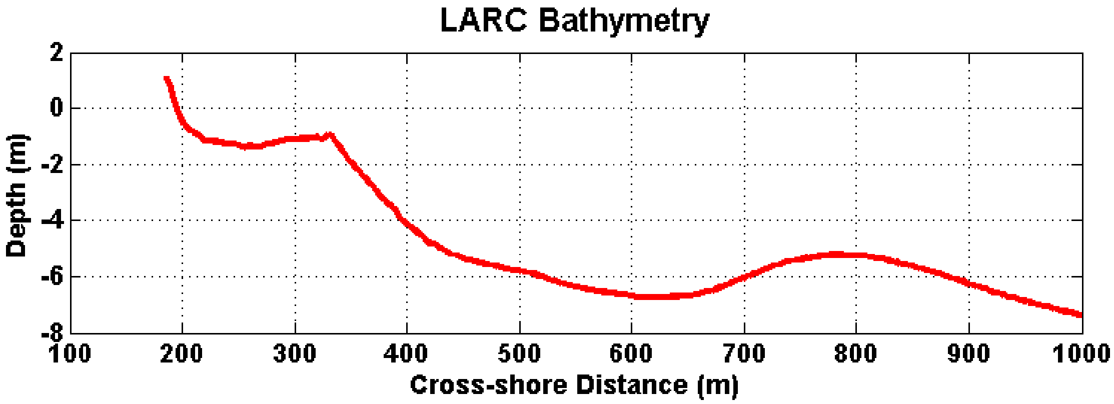

Figure 11: Bathymetry data from the LARC at a cross-shore profile in view of the camera.

2.3 Image Statistics

A qualitative assessment of the breaking patterns can be deduced from statistical analysis of the raw images. In this study, the average, maximum, and standard deviation of the video images are calculated for every burst. The average image is found by averaging the pixel intensities at every location in the raw images for the 1200 frames taken for each burst. The raw image is then rectified and normalized by the maximum pixel intensity and an example of a burst averaged rectified image is shown in Figure 12. Because the foam from a breaking wave tends to be brighter, the higher pixel intensities shown in this image represent locations where wave breaking has commonly occurred with the brightest pixel intensities, such as around cross-shore location 300 m. Comparing this figure to the bathymetry shown in Figure 11, the initiation of wave breaking, occurring at cross-shore location 350 m, corresponds to the peak of the crest of an inner bar.

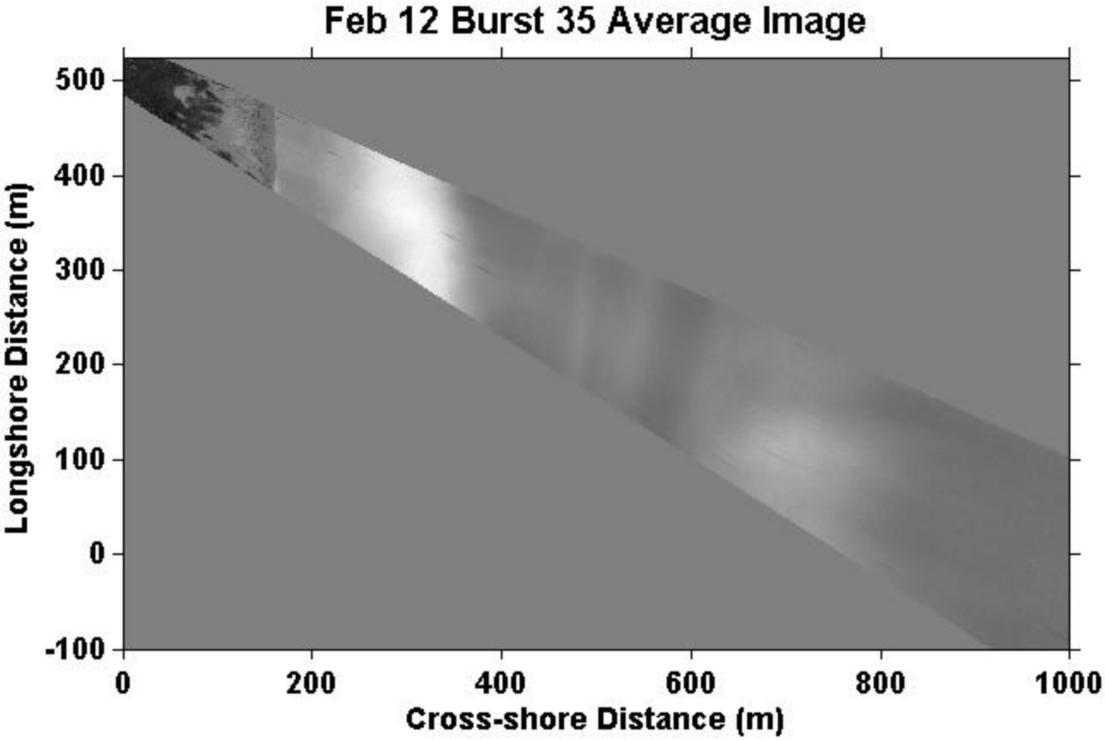

Figure 12: Rectified average image from February 12 Burst 35.

Similarly, the maximum image is created by taking the maximum pixel intensity at every location of the raw image throughout the duration of the burst. An example image, called the “brightest image”, is shown in Figure 13 and shows every location that a breaking wave has occurred for that burst. The brightest image more clearly shows the existence of the offshore bar over which waves are breaking compared to Figure 12, because only a small fraction of the largest waves break on the outer bar, preventing them from being obvious in the average image.

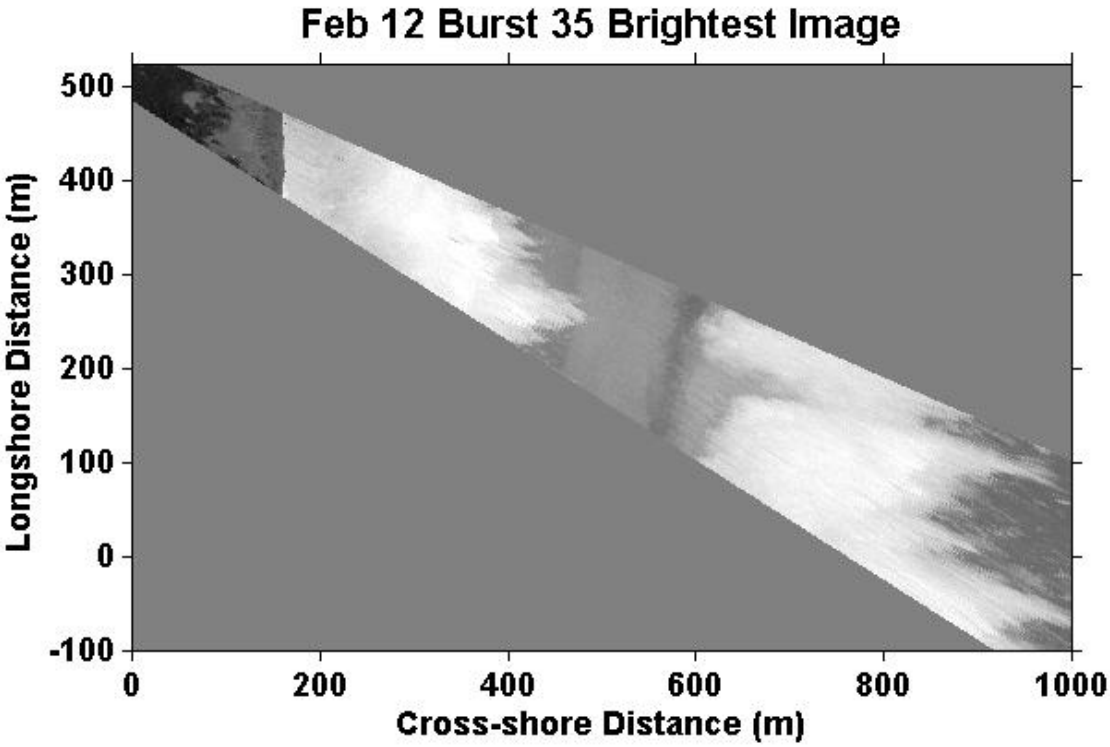

Figure 13: Rectified brightest image from February 12 Burst 35.

Perhaps the most useful statistical image is the standard deviation image because it removes much of the bias seen in the average and brightest images by showing the persistent locations of wave breaking. However, because the standard deviation is very sensitive to changes in pixel intensities, changes in lighting throughout a burst can significantly affect the image. Therefore, a linear trend is fit to the pixel intensities at each location for every burst and removed from the intensity values. Then, the standard deviation image is calculated by finding the square root of the variance of the pixel intensities at every location in the raw image throughout the burst. This image, shown in Figure 14, more clearly shows breaking on the outer bar compared to the average image in Figure 12; however, it also shows preferential breaking on the inner bar more clearly than the brightest image in Figure 13.

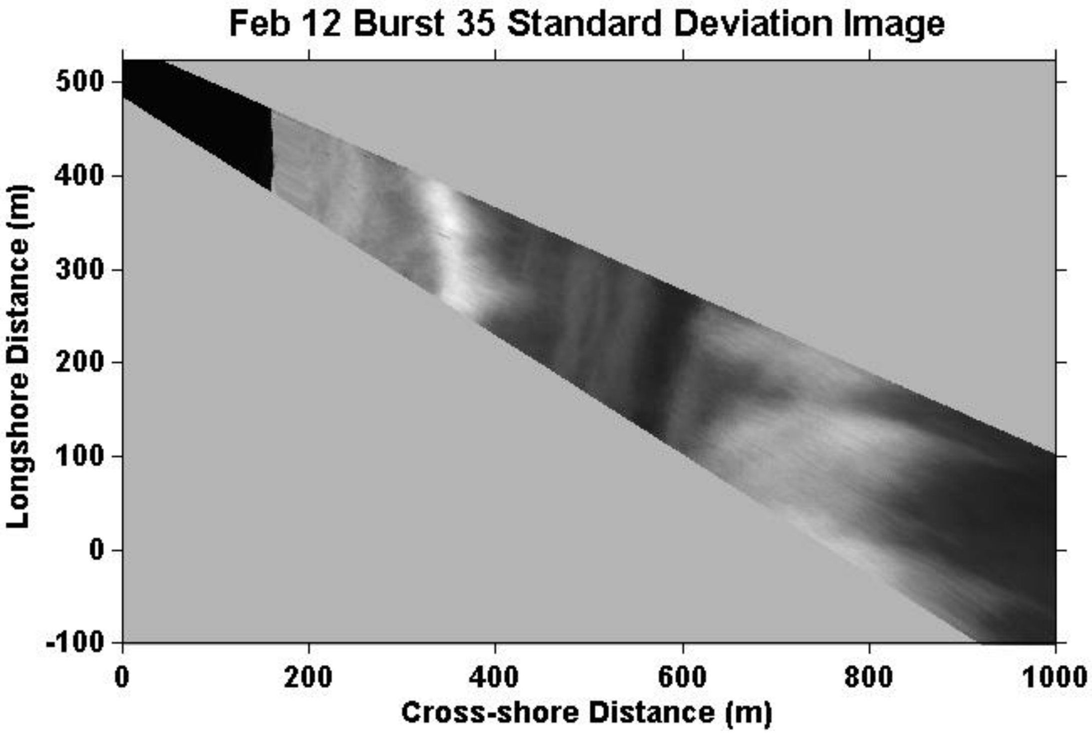

Figure 14: Rectified standard deviation image from February 12 Burst 35.

Because the burst calculated statistical images are often misleading due to fluctuations in the breaking patterns from one burst to the next, group calculated statistical images are useful for providing a comprehensive assessment of the patterns over time. The group images can be calculated using as few as two up to any number of bursts but typically five bursts, or thirty minute statistics, adequately represent wave conditions. Using the burst calculated raw images, the group average and maximum raw images are calculated as before. However, the standard deviation image uses the definition of the burst variance, σ_b^2, at every pixel location

$$\sigma_b^2 = \frac{1}{N-1}\sum_{i=1}^{N}(x_i - \overline{x_b})^2 \tag{15}$$

where x_i is the pixel intensity of frame i, $N = 1200$ frames, and $\overline{x_b}$ is the average pixel intensity for the burst. Manipulating Equation (15) gives

$$\sum_{i=1}^{N} {x_i}^2 = (N-1)\sigma_b^2 + N\,{\overline{x_b}}^2\,. \tag{16}$$

Next, the group variance, σ_g^2, can be found as

$$\sigma_g^2 = \frac{1}{N_g - 1}\left(\sum_{i=1}^{N_g} {x_i}^2 - N_g\,{\overline{x_g}}^2\right) \tag{17}$$

where N_g is the number of total frames, and $\overline{x_g}$ is the average pixel intensity for the group of bursts. Defining M as the number of bursts, Equation (17) can be re-written as

$$\sigma_g^2 = \frac{1}{(MN-1)}\left(\sum_{b=1}^{M}\sum_{i=1}^{N} {x_{i,b}}^2 - MN\left(\frac{\sum_{b=1}^{M}\overline{x_b}}{M}\right)^2\right) \tag{18}$$

where $x_{i,b}$ is the pixel intensity for frame i of burst b. This allows for the group variance to be found with Equations (16) and (18) in terms of parameters solved from individual bursts. The standard deviation image is found by taking the square root of the group variance pixel intensity at each pixel location. Calculating the standard deviation image for a group of five bursts, as shown in Figure 15, is similar to the burst variance image but has much smoother features, especially on the outer bar and the edge of the surfzone due to the larger sampling size available for calculating the statistic.

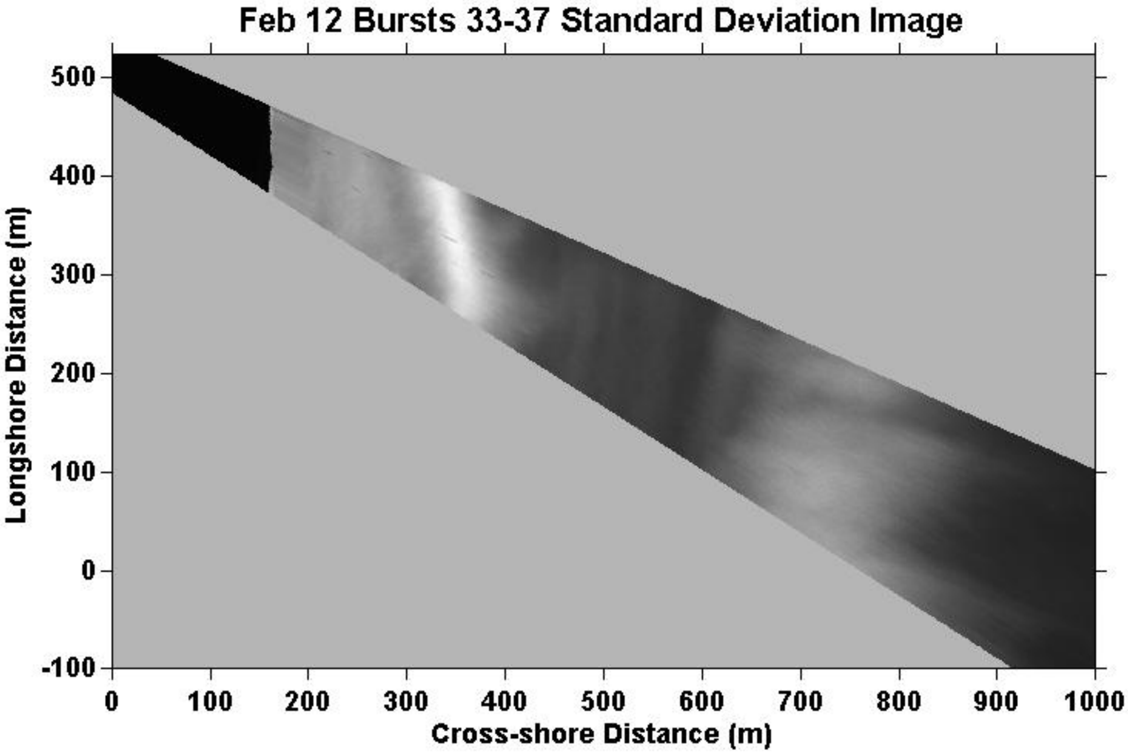

Figure 15: Rectified group standard deviation image from February 12 Bursts 33 – 37.

2.4 Method for Quantifying Longshore Currents

An advantage of transforming raw video images to a real-world coordinate system is the ability to relate pixel intensities to a physical location. This allows nearshore flow properties, such as longshore currents, to be quantified by tracking the surface foam from breaking waves, represented by bright pixel intensities, through the video domain. The velocities are determined using the Optical Current Meter technique developed by Chickadel et al. (2003), which estimates the currents from a pixel intensity spectrum created from a timestack.

2.4.1 Timestack Generation

The first step in creating a timestack is to specify longshore arrays throughout the surfzone of rectified images. Each of these arrays has longshore spacing of 0.25 m with cross-shore resolution of every 5 m, as shown in Figure 16. The array resolution allows the foam wavelengths observed by the camera to be represented by an adequate number of pixel intensities such that the foam patterns are resolved.

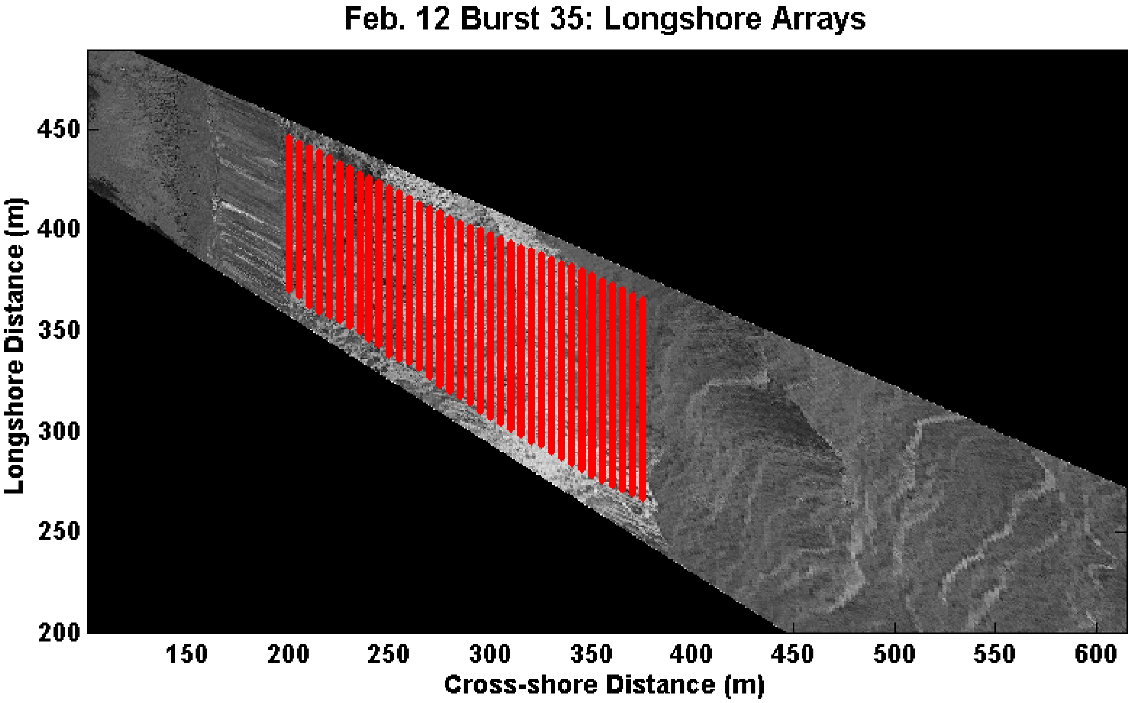

Figure 16: Longshore arrays (red lines) defined throughout the surfzone for February 12 Burst 35.

For every array, a timestack, or time series of pixel intensities along the array, is created. First, a filter is applied to the raw image to enhance the signals of the advected foam. The filters tested include an unsharp filter that sharpens the image by subtracting a blurred version of the image from itself, a one-dimensional (1D) median filter that removes noise while preserving edges in the image, and a combination of the unsharp and median filters. The median filter alone is selected as the best option. Then, the timestacks are created by extracting the pixel intensities from each array point in the raw image and stacking them frame-by-frame for each six minute burst using a time step of

0.60 seconds such that time (t) increases down on the y-axis and the distance across the longshore array increases right on the x-axis, as shown in Figure 17.

Before using the timestacks to quantify longshore currents or to make any physical interpretations about them, the dark, completely vertical artifacts, shown in the timestack on the left in Figure 17, are removed. These artifacts result from “dead” pixels that create a black spot on the raw image, and appear as vertical lines on the timestack because their longshore position on the array length does not change with time. Because timestacks are created such that distance is on the x-axis and time is on the y-axis, the slope of the vertical lines is the inverse of velocity. Since a completely vertical line has an infinite slope, the velocity is zero, which causes the estimation of longshore currents from timestacks to be biased low. Therefore, the cleaned timestacks, such as the one on the right in Figure 17, are used for estimating longshore currents.

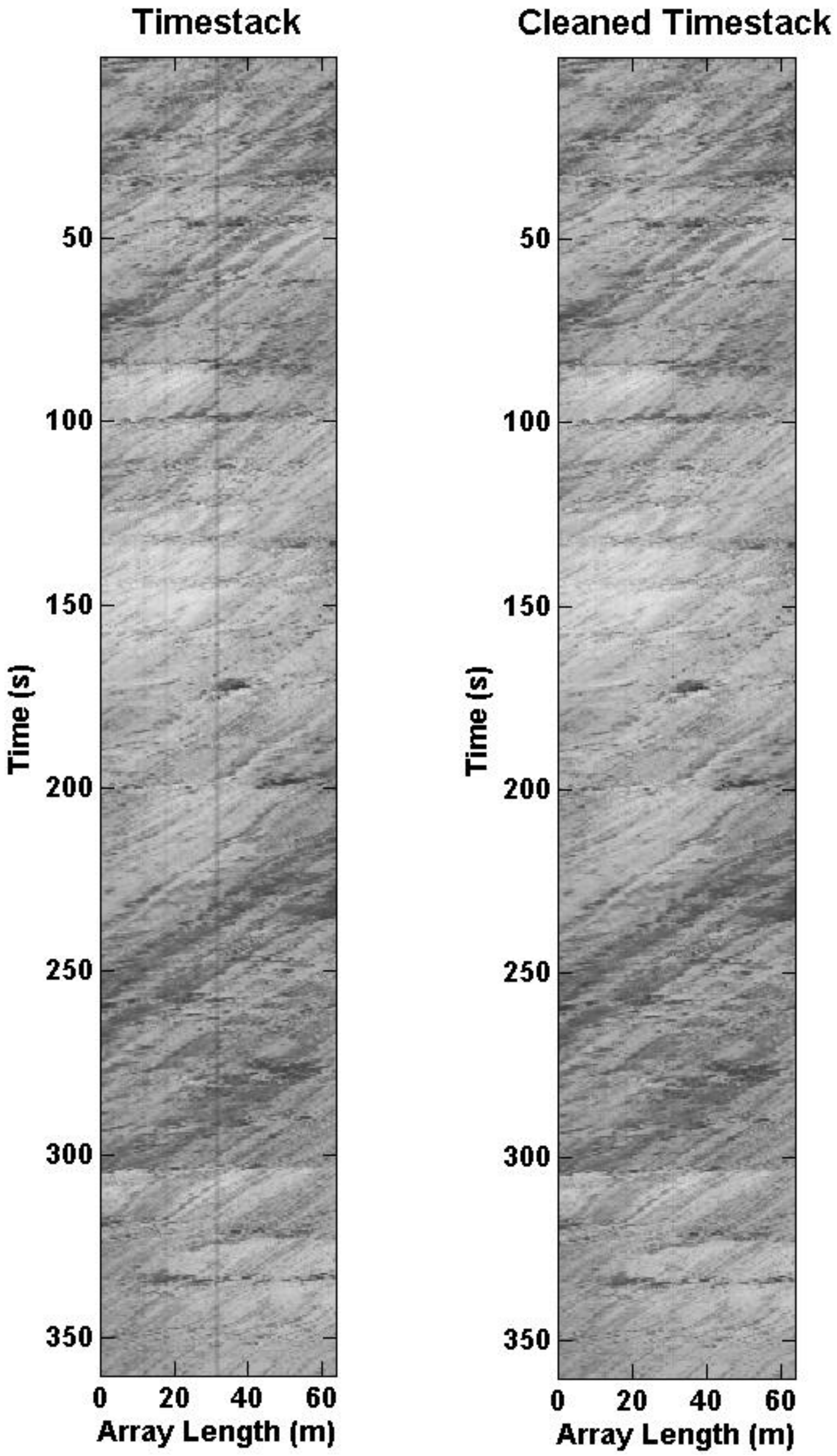

Figure 17: Timestack generated from the tenth longshore array for February 12, Burst 35 (left) prior to removing artifacts and (right) after removing artifacts.

2.4.2 Optical Current Meter Technique

Although an estimate of longshore currents can be obtained from timestacks by manually calculating the slope of the foam streaks, it is a very tedious and crude method that is unfeasible to use. Therefore, a technique developed by Chickadel et al. (2003), named the Optical Current Meter (OCM) technique, is used to estimate longshore currents by analyzing segments of a timestack. First, a window size, or length and height of the segment, is specified. The number of segments resulting from a divided timestack is dependent on the window size and amount of overlap. A filter is also applied to the timestack to eliminate noise so that the trackable foam signal is enhanced. The filters tested are the same filters tested on the raw images, with the addition of a Matlab image filter, imadjust, that maps the intensity values to new values such that 1% of the data is saturated at low and high intensities of the image, thereby increasing the contrast of the output image. However, the best results are obtained by applying the median filter to the individual segments. The effect of this filter is shown in Figure 18, where the original segment is shown on the left and the filtered segment is shown on the right. Clearly, the median filtering smoothes the small scale features, which are difficult to track due to the oblique camera angle, such that the large scale foam patterns are the dominant signal in the segments.

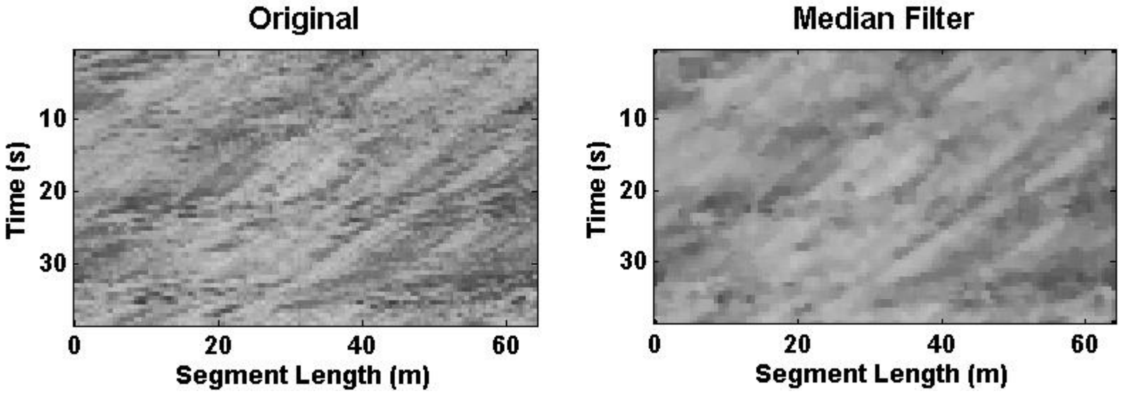

Figure 18: The original timestack segment (left) and the filtered timestack segment (right).

Using the median filtered segments, a two-dimensional (2D) frequency (f_l) – longshore wavenumber (k_y) spectrum, $\hat{I}(f_l, k_y)$, is created using a 2D Fourier transform,

$$\hat{I}(f_l, k_y) = \iint B(t,y) I(t,y;x) e^{-i2\pi f_l t} e^{-i2\pi k_y y}\, dt\, dy \tag{19}$$

where $I(t,y)$ represents the intensity data for the timestack segment and $B(t,y)$ is a 2D Bartlett multiplicative filter used to window the input data to reduce noise in the spectrum. The 2D spectrum, $S(f_l, k_y)$ is defined as

$$S(f_l, k_y) = \hat{I}(f_l, k_y) \hat{I}(f_l, k_y) * \tag{20}$$

where $\hat{I}(f_l, k_y) *$ is the complex conjugate. An example of this spectrum is shown in Figure 19, where longshore velocity is represented by the ratio of frequency to wavenumber and is shown by the diagonal ray of high intensity pixels extending from the origin toward the upper right.

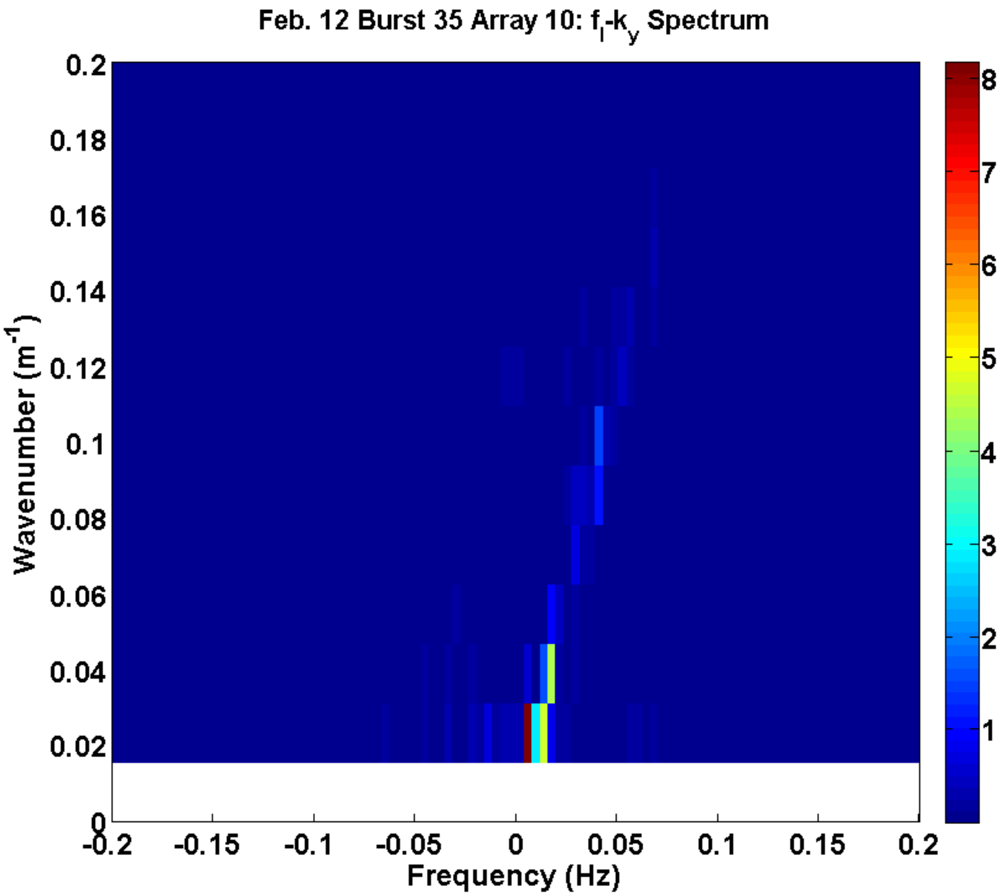

Figure 19: The frequency – wavenumber spectrum calculated from a timestack segment.

The frequency – wavenumber spectrum is then transformed into a velocity – wavenumber spectrum, $S(v_y, k_y)$, by defining the longshore current, v_y, as

$$v_y = \frac{f_l}{k_y}. \tag{21}$$

The transformation requires that the variance is conserved as

$$var\{S(f_l, k_y)\} = \iint S(v_y, k_y)|k|\, dv_y\, dk_y \tag{22}$$

where $|k|$ is the Jacobian determinant. Although 1D and 2D interpolation schemes were tested to create this spectrum, the 1D Piecewise Cubic Hermite Interpolating Polynomial (PCHIP) scheme proved to be the most useful in creating a smooth spectrum. The velocity – wavenumber spectrum is shown in Figure 20 and is bound between -3 m/s and +3 m/s to eliminate signals from passing wave crests. In this spectrum, the longshore velocity is represented by a vertical ray of concentrated energy and indicates a southerly current with a magnitude around 0.5 m/s.

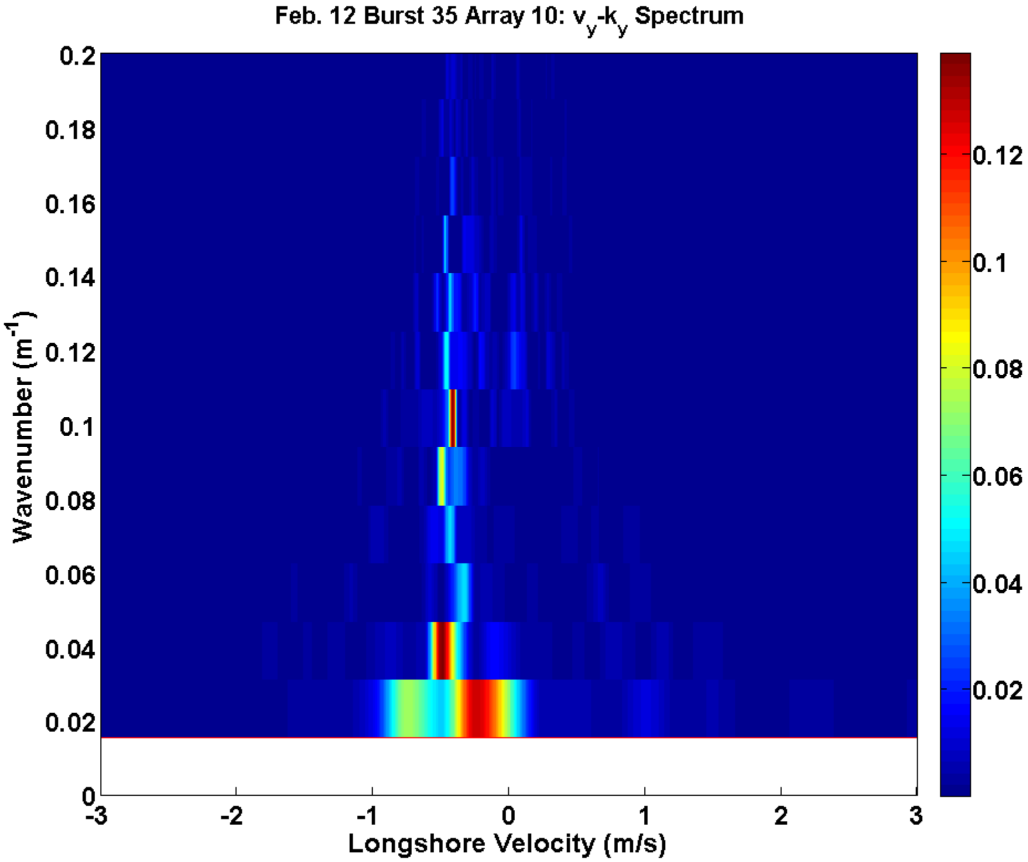

Figure 20: The velocity – wavenumber spectrum transformed from the frequency – wavenumber spectrum.

Lastly, the velocity – wavenumber spectrum is integrated from a minimum specified wavenumber (k_{min}) to a Nyquist wavenumber (k_{nyq}) to yield a velocity spectrum, $S(v_y)$, defined as

$$S(v_y) = \int_{k_{min}}^{k_{nyq}} S(v_y, k_y)\, dk_y \,. \tag{23}$$

An example of this spectrum is shown in Figure 21 by the black pluses and clearly indicates a peak in the integrated spectrum. However, the single value for surface longshore velocity is not equal to this peak because $S(v_y)$ is made of a broad range of energies that convolute the spectrum. Therefore, the representative longshore velocity is determined by using a nonlinear least squares method to fit a model spectrum, $S_m(v_y)$, to $S(v_y)$. The model spectrum contains a signal from foam traces, $S_{foam}(v_y)$, and a signal from background noise, $S_{noise}(v_y)$, and is given by

$$S_m(v_y) = S_{foam}(v_y) + S_{noise}(v_y)\,. \tag{24}$$

$S_{foam}(v_y)$ is assumed to be Gaussian with an amplitude of A_{foam}, an average velocity of $\overline{v_y}$, and a width of σ_{foam}. The noise is modeled by assuming a uniformly distributed white noise pixel intensity time series over $S(f_l, k_y)$ and transforming it to the velocity spectrum. The modeled velocity is shown in Figure 21 by the blue line, where the peak in the curve is the representative longshore current.

To control the quality of the results obtained from using the OCM technique, a "goodness of fit" test is performed on $S(v_y)$ and $S_m(v_y)$. This statistical test describes the quality of the model fit to the data by a Chi-squared test, χ^2, such that

$$\chi^2 = \sum_{i=1}^{N} \left[\frac{S\left(v_y(i)\right) - S_m\left(v_y(i); \hat{\beta}\right)}{\sigma(i)} \right]^2 \tag{25}$$

where $\hat{\beta}$ are the set of "best fit" parameters $\left(\sigma_{foam}, \overline{v_y}, A_{noise}, A_{foam}\right)$ and $\sigma(i)$ is the standard deviation of the measurement error at each point i. Following the same criteria as Chickadel et al. (2003), the velocity estimated from the $S(v_y)$ spectrum is accepted if it has greater than a 90% significance fit and if the 95% confidence range for $\overline{v_y}$, named crange, is less than 0.2 m/s. Figure 21 represents a spectrum that estimates a velocity within these criteria and is accepted.

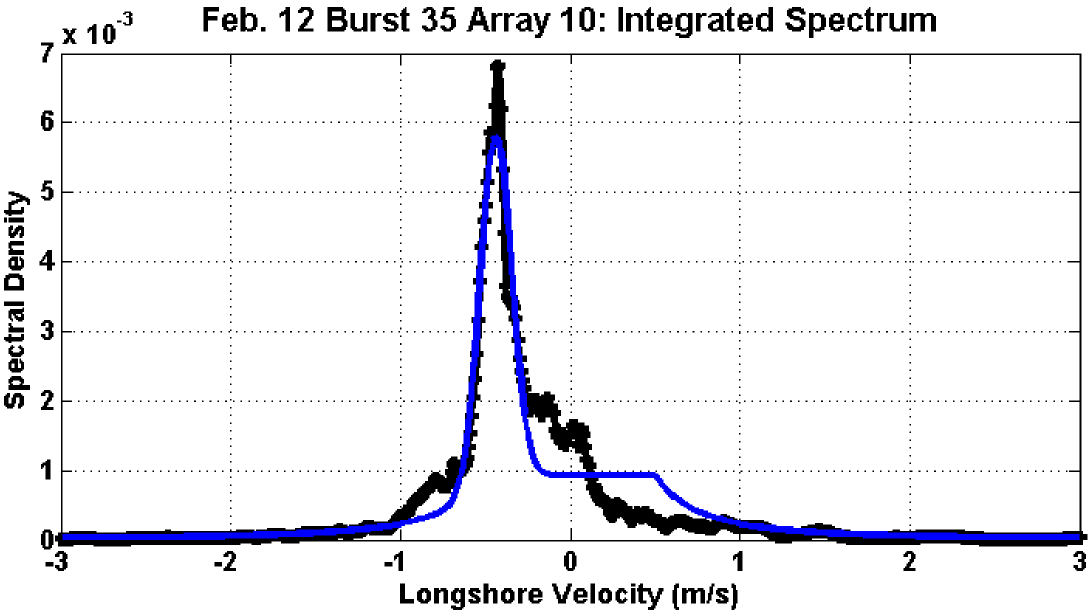

Figure 21: The longshore velocity spectrum (black pluses) obtained from integrating $S(v_y, k_y)$ with respect to wavenumber with the modeled velocity spectrum (blue line).

Because passing wave crests are associated with high velocities and small wavenumbers, Chickadel et al. (2003) specify k_{min} to be $0.125\,m^{-1}$ and k_{nyq} to be $1/(2dy)$ where dy is the longshore spacing. However, due to the flat angle of the camera view, only large scale foam patterns, which have small wavenumbers, are trackable. After testing several values of k_{min} and k_{nyq}, the minimum wavenumber is reduced to $0.03\,m^{-1}$ and the Nyquist wavenumber is specified as $1/(4dy)$ to obtain realistic current magnitudes and cross-shore profile variation.

In addition to k_{min} and k_{nyq}, several values for other parameters, such as f_{min} and f_{nyq}, the window size, and timestack resolution, were tested to eliminate noise in the spectrum. Changing f_{min} or f_{nyq} had no effect on the noise in the spectrum and the resulting velocities estimated by OCM were almost identical. However, a reduction in window size negatively affected the OCM results because the window was too small to resolve the large scale foam patterns. Therefore, a typical window size of 64 m by 38.4 s with a resolution of 0.5 m and a 19.2 s overlap is used, which corresponds to 128 pixels in length by 64 pixels in time with a 2 pixel resolution 32 pixel overlap of segments.

2.4.3 Error Assessment

Since the sea surface is assumed to be a flat plane of constant elevation, an apparent velocity is induced from vertical sea surface motion. The apparent velocity results from the 2D horizontal video interpreting the third dimension, vertical motion, as horizontal motion. For the viewing angle of the camera used in this study, an additional positive horizontal velocity component in the video estimated currents is induced by a positive vertical velocity in the real world coordinate system. Therefore, a new analysis was performed to quantify the apparent velocity to determine its relative magnitude to the final current estimates obtained from the OCM technique.

First, a coordinate system is defined in Figure 22 that relates the camera location, (x_c, y_c, z_c), to a point on the sea surface, (x_p, y_p, z_p), where the distance between them, $\vec{r}$, is given as

$$\vec{r} = \Delta x\hat{\imath} + \Delta y\hat{\jmath} + \Delta z\hat{k} \tag{26}$$

and

$$\Delta x = x_p - x_c \tag{27a}$$

$$\Delta y = y_p - y_c \tag{27b}$$

$$\Delta z = z_p - z_c\ . \tag{27c}$$

The location of the x, y, and z axis in Figure 22 are given in the rescaled coordinate system used for all survey data and $z_p = -38$ m which corresponds to the ellipsoid height of the plane specified as mean sea level.

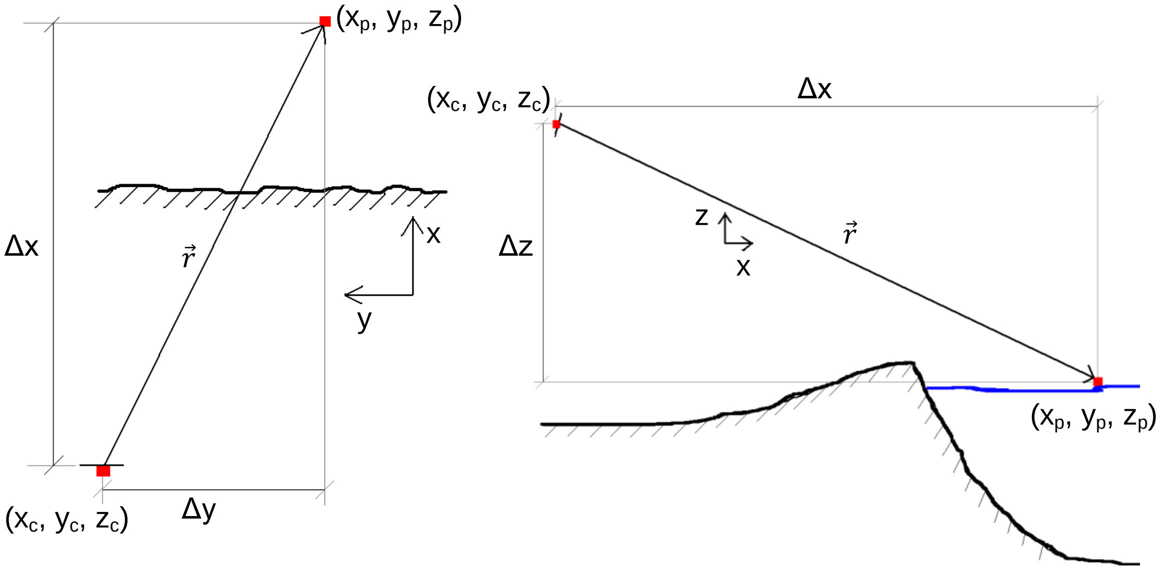

Figure 22: The coordinate system relating the camera location to a location on the sea surface in (left) plan view and (right) side view.

Defining the real world vertical motion by the vector, $\boldsymbol{A} = \hat{k}$, shown in Figure 23 where $\hat{k}$ is the vertical unit vector, the horizontal component induced in the video can be determined by projecting this vector onto the image plane. Since the camera's line of sight, given by $\vec{r}$, is normal to the image plane, the orientation of the image plane can be found by normalizing $\vec{r}$ by n which is given by

$$n = \sqrt{\Delta x^2 + \Delta y^2 + \Delta z^2} \tag{28}$$

such that $\vec{r}/n$ is defined as

$$\frac{\vec{r}}{n} = \boldsymbol{B} = \langle \frac{\Delta x}{n}, \frac{\Delta y}{n}, \frac{\Delta z}{n} \rangle = \langle a, b, c \rangle \tag{29}$$

The plane normal to the camera's line of site, $\boldsymbol{P}$**,** is defined by the unit normal vector $\boldsymbol{B} = a\hat{\imath} + b\hat{\jmath} + c\hat{k}$, where $a^2 + b^2 + c^2 = 1$, as

$$ax + by + cz + d = 0 \tag{30}$$

where d defines the specific location of the plane and is not important for this analysis. The projection of $\boldsymbol{A}$ onto $\boldsymbol{P}$, $\vec{k}_p$ illustrated in Figure 23, is found by

$$\vec{k}_p = \boldsymbol{B} \times (\boldsymbol{A} \times \boldsymbol{B}) = -ac\hat{\imath} - bc\hat{\jmath} + (a^2 + b^2)\hat{k}. \tag{31}$$

To translate the apparent velocity observed in the video into the real world coordinate system so that the error can be assessed, the projection of the horizontal vector, $\boldsymbol{C} = \hat{\jmath}$, onto $\boldsymbol{B}$ is

$$\vec{\jmath}_p = \boldsymbol{B} \times (\boldsymbol{C} \times \boldsymbol{B}) = -ab\hat{\imath} + (a^2 + c^2)\hat{\jmath} - bc\hat{k} \tag{32}$$

and is illustrated in Figure 23. Defining $\vec{k}_p$ as the velocity, or the line of interest projected onto the image plane, and $\vec{\jmath}_p$ as the y-direction, or the source line projected onto the image plane, the magnitude of the horizontal motion, y_p**,** is found by the projection of $\vec{k}_p$ onto $\vec{\jmath}_p$, which is shown in Figure 23 and is defined as

$$y_p = \vec{k}_p || \vec{\jmath}_p = \frac{\vec{k}_p \cdot \vec{\jmath}_p}{\left|\vec{\jmath}_p\right|} = \frac{-bc}{\sqrt{(a^2 + b^2)}}. \tag{33}$$

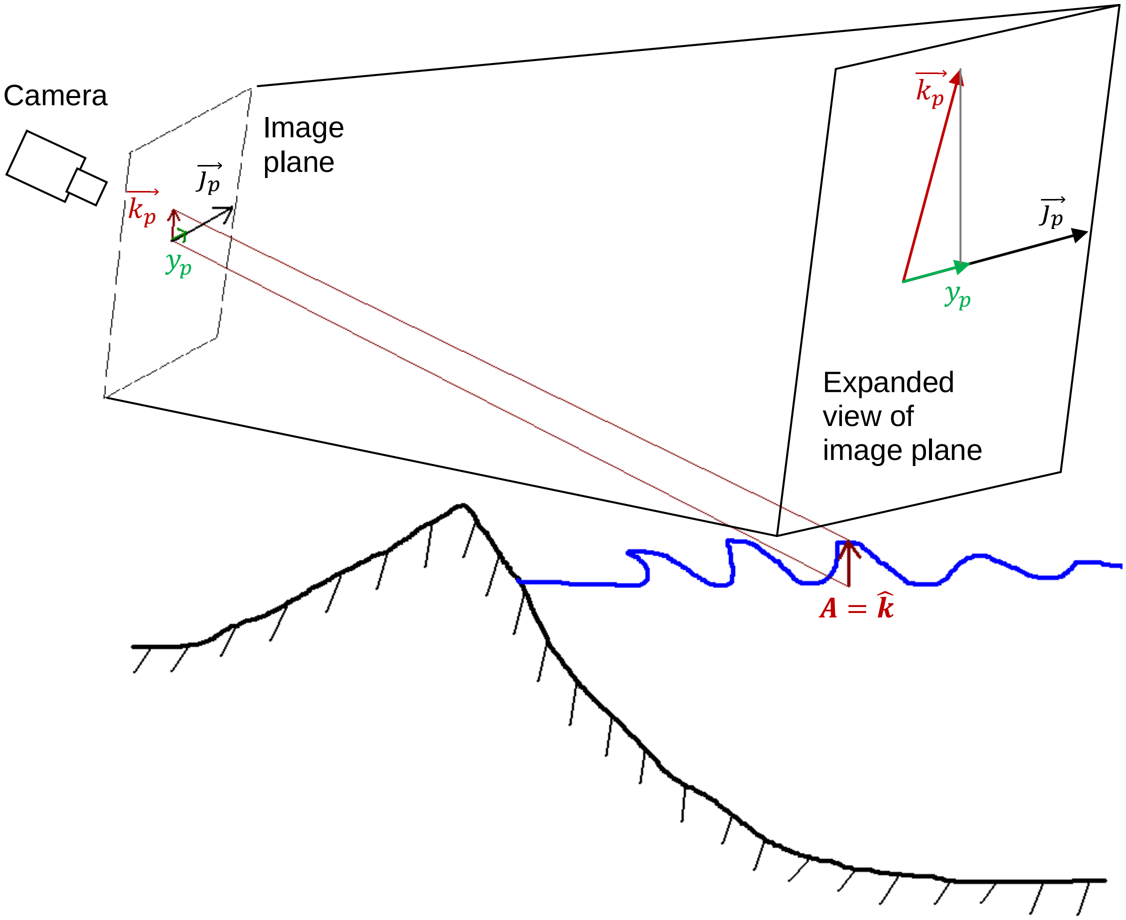

Figure 23: Schematic of the vector projections used to estimate the apparent velocity.

Assuming that the vertical motion of the sea surface, z_s, can be represented as a regular sawtooth wave, z_s is defined as

$$z_s = \frac{-H}{L} C_w t + \frac{H}{2} \tag{34}$$

where H is the wave height, L is the wave length, C_w is the wave celerity and t is time. Since the foam on the backside of the wave is being tracked by the video, the decrease in surface elevation, or the diagonal portion of the sawtooth shape, is the only vertical motion used for this error assessment. Therefore, the horizontal component of the vertical motion, y_a, is found by combining Equations (33) and (34) to obtain

$$y_a = \frac{-bcH\left(\frac{1}{2} - \frac{C_w t}{L}\right)}{\sqrt{a^2 + c^2}}. \tag{35}$$

The apparent velocity, v_{app}, is defined as the rate of change of the vertical motion

$$v_{app} = \frac{dy_a}{dt} = \frac{bcHC_w}{L\sqrt{a^2 + c^2}} = \frac{H\left(\frac{\Delta y}{n}\right)\left(\frac{\Delta z}{n}\right)(C_w)}{L\sqrt{\left(\frac{(\Delta x)}{n}\right)^2 + \left(\frac{(\Delta z)}{n}\right)^2}}. \tag{36}$$

This equation shows that as the longshore distance from the camera to the survey point becomes large, the apparent velocity increases. However, the apparent velocity decreases as the cross-shore distance between the two points increases. This indicates that the apparent velocity is a function of the angle formed by the longshore and cross-shore distances from the camera to the survey point found as $\tan^{-1}(\Delta y/\Delta x)$ such that the apparent velocity decreases as the angle decreases. Due to the distance that the camera is set back from the shore, Δx, which ranges from 490 m to 670 m, is generally larger than Δy, which ranges from 226 m to 405 m, causing the angle and, thus, the apparent velocity to be smaller. A larger Δz gives a smaller apparent velocity; however, in this case the sea surface is assumed to be a horizontal plane and the camera has a fixed location, producing a constant Δz.

Using shallow water approximations to find celerity and wave length from the maximum surfzone wave height and period measured by in situ instrument, N1, the maximum apparent velocity observed by the video throughout the duration of the experiment is calculated. For $H = 1.76$ m and $T = 9.40$ s, the apparent velocity is calculated at every point along the longshore arrays used for creating timestacks and is shown in Figure 24. The largest apparent velocity is observed to have a maximum value of 0.01 m/s along the first array at the leftward-most point located at $\Delta x = 490$ m,

$\Delta y = -300$ m. Because the observed longshore velocities range between 0.1 m/s and 1.5 m/s, this part of the error for the OCM technique is obviously quite small.

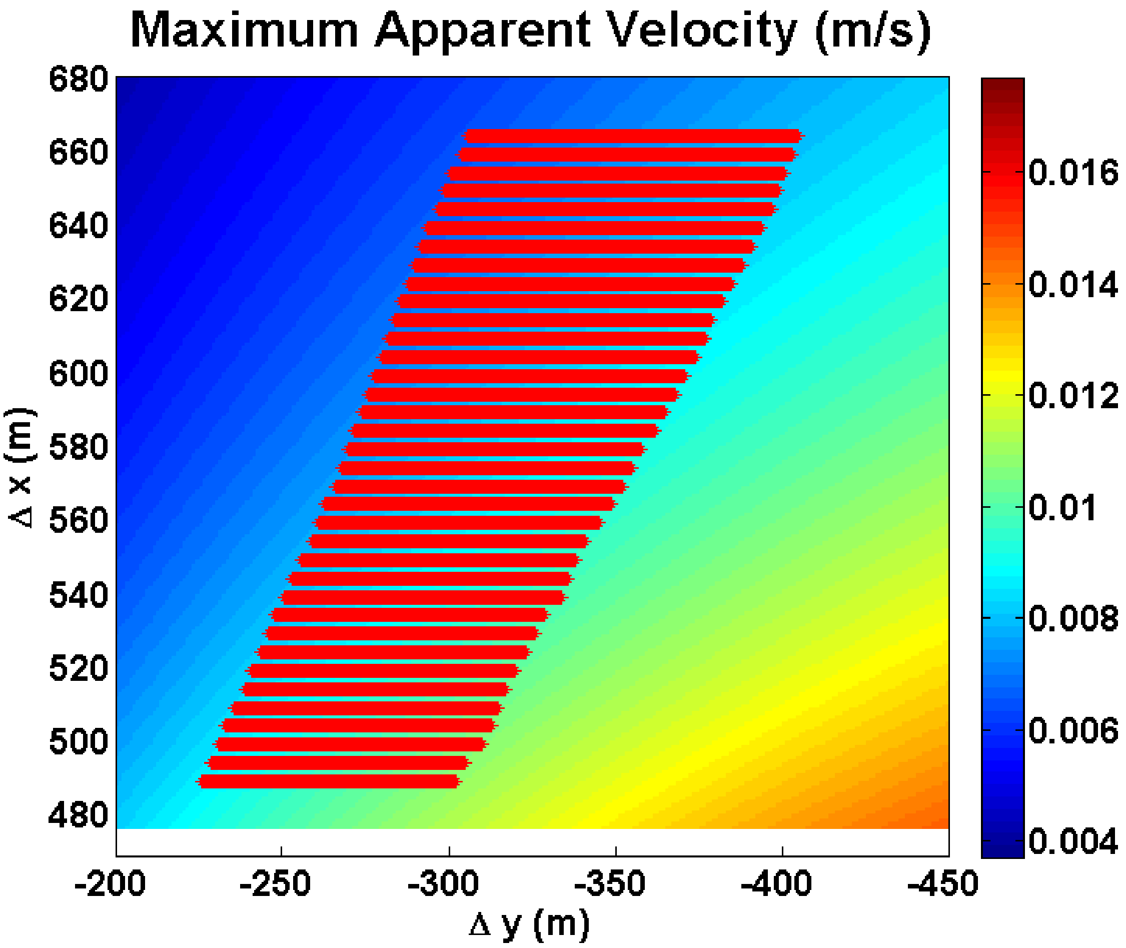

Figure 24: Maximum apparent velocity (m/s) observed by the video for the CH2010 study for every array location (red solid), where the warmer colors indicate a larger apparent velocity.

Although an in situ instrument was deployed in view of the camera, it was located outside the surfzone so longshore velocity measurements cannot be directly compared to video estimated currents, which are located inside the surfzone. To ensure that the velocities estimated using the OCM technique are realistic and representative of the currents observed in the video, the foam is tracked manually for several bursts. This is done by plotting two cross-shore arrays 20 m apart on the video images as shown in Figure 25 by the green lines, and measuring how long it takes for foam to be advected from one array to the next. Using the software program Adobe Premiere, the foam is tracked between the arrays at 50 m intervals in the cross-shore direction, indicated by the blue dots in Figure 25, and the time taken for the foam to be advected 20 m is recorded. Dividing the distance by the time yields the longshore current.

This process is repeated for a total of five tests at each cross-shore location and averaged together to yield the currents listed as Manual in Table 4. The cross-shore locations in the real-world coordinate system are given, where x = 215 m is the shoreward-most location of estimated currents, x = 365 m is the offshore edge of the inner surfzone, and x = 775 m represents the outer surfzone at the offshore bar.

For comparison, the currents estimated using the OCM technique are also given, where NaN indicates currents that are rejected, and are generally weaker than the manually tracked currents. This may be due to a difference in sampling size since OCM averages currents for 17 segments but only 5 sets are tracked manually. Also, tracking the foam in the video is somewhat subjective since the signals such as passing wave crests interfere with the user's visibility of the foam while the OCM technique eliminates this interference from wave crests in the spectra used to estimate currents. However, the general trend of the currents from manual tracking and OCM is similar, with weaker currents observed at the edges of the surfzone and maximum currents in the center. The cross-shore variation and magnitude of the currents estimated manually are given in Figure 25 and show maximum currents shoreward of the initiation of breaking.

Although in most cases the OCM technique rejects the currents on the outer bar, the accepted estimated currents at that location are unrealistically large and vary significantly from the manual estimates. This is due to the flat angle of the camera view which causes only wave crests to be visible and the waves propagate in so quickly that residual foam cannot be tracked. Because of the difficulty in manually tracking foam and the high number of rejected OCM estimated currents, estimates of currents outside the inner surfzone are neglected.

Table 4: Longshore currents estimated by manually tracking foam and using the OCM technique at five cross-shore locations for six bursts.

Feb. 7, 2010		**x = 215 m**	**x = 265 m**	**x = 315 m**	**x = 365 m**	**x = 775 m**
Burst 14	Manual (m/s)	0.98	1.14	1.55	1.26	1.73
	OCM (m/s)	0.54	0.93	NaN	0.63	NaN
Burst 19	Manual (m/s)	1.10	1.24	1.19	0.98	1.37
	OCM (m/s)	0.52	1.07	0.72	0.60	NaN
Burst 34	Manual (m/s)	0.85	1.36	1.34	0.95	1.31
	OCM (m/s)	0.66	0.88	0.65	0.46	0.59
Burst 39	Manual (m/s)	0.89	1.19	1.34	1.01	1.45
	OCM (m/s)	0.80	1.10	0.78	0.80	NaN
Burst 54	Manual (m/s)	0.88	1.39	1.20	0.91	1.43
	OCM (m/s)	0.35	1.15	0.73	0.46	NaN
Burst 59	Manual (m/s)	1.07	1.25	1.41	0.84	1.35
	OCM (m/s)	0.56	NaN	NaN	0.57	NaN

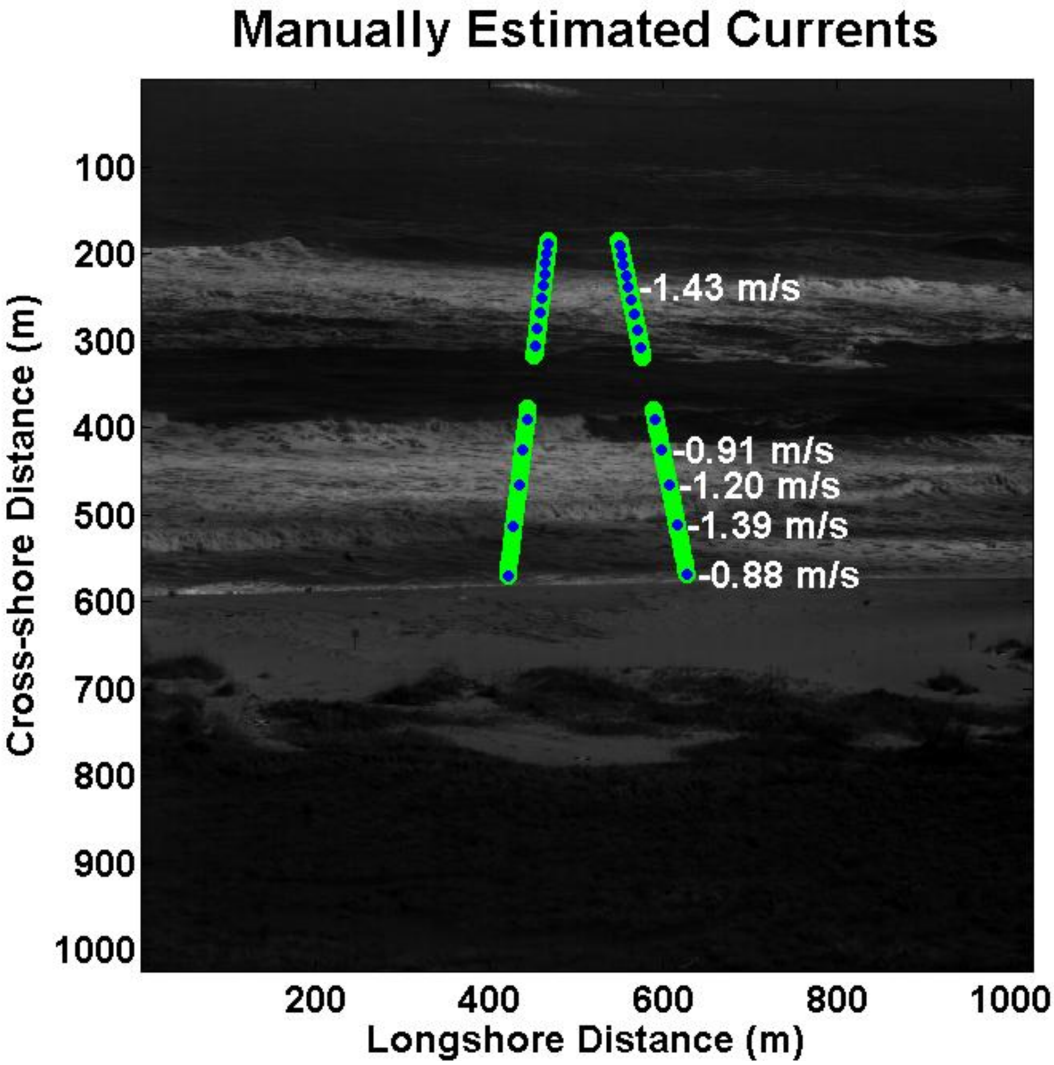

Figure 25: Cross-shore variation of estimated longshore current velocities that are manually tracked between two cross-shore arrays (green solid) separated by 20 m at cross-shore locations (blue dots) separated by 50 m for February 7, Burst 54.

CHAPTER 3

EXPERIMENTAL RESULTS

This chapter presents the experimental data consisting of meteorological observations, in situ measurements and video observations of morphology and longshore currents. Storm events are identified from the meteorological data and a Nor'easter event is isolated for estimating currents. The in situ and video data collected during this storm is used to estimate morphological features of the nearshore using image statistics and longshore currents using the Optical Current Meter technique.

3.1 In Situ Data

The wind, wave and longshore current data for the duration of the experiment is given in Figure 26. The wind data were obtained from National Oceanic and Atmospheric Administration (NOAA) buoy station 41025 located offshore from Diamond Shoals at 35.006 N 75.402 W and the wave and longshore current data were obtained from instruments N6 and N8 located on the north and south sides of the cape, respectively (Figure 3). Throughout the duration of the experiment, five storm events occurred and are numbered in Figure 26 (c). These events are identified by a significant increase in wave height and the wind speed and direction varies greatly between storms (Figure 26 (a) and (b)). The north/south component of the velocity is shown in Figure 26 (d), where the maximum of the south component is larger than the maximum of the north component.

Of the five events identified from the data, the focus of this study is on Event 4, which is a Nor'easter storm occurring on February 12 and 13. This event is chosen because the north side of the cape, which is the side that the camera records a 100 m longshore section, is affected by the wind and wave conditions. Video data collected during this storm is good quality and the instrument in view of the camera, N1, had been deployed prior to this event. Also, the wind and wave conditions change significantly throughout the duration of the storm, and the effects of these changing conditions on the wave breaking patterns and video estimated currents are analyzed.

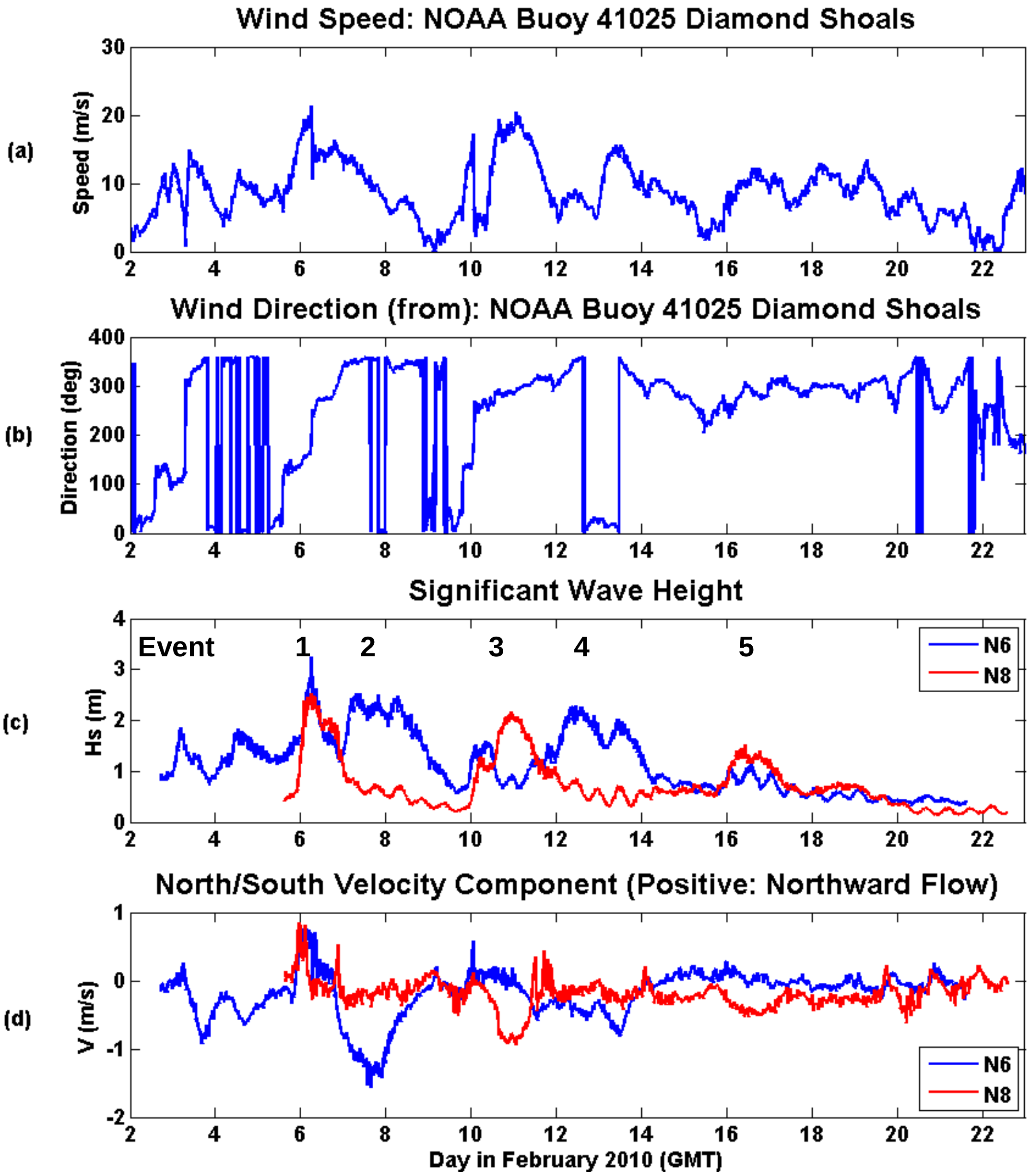
Wind Speed: NOAA Buoy 41025 Diamond Shoals

Wind Direction (from): NOAA Buoy 41025 Diamond Shoals

Significant Wave Height

North/South Velocity Component (Positive: Northward Flow)

Figure 26: (a) 8 minute averaged wind speed, (b) wind direction (positive counter-clockwise from west), (c) significant wave height (Hs), and (d) 17 minute averaged north/south velocity component (v) 0.4 m above the seafloor.

The hour-averaged conditions for February 12, listed in Table 5, and February 13, listed in Table 6, represent the storm event conditions for the hours with available video estimates of currents. For the specified day and hour, wave data were obtained from in situ instrument N1 and the 15 minute bursts were averaged over an hour. The parameters include significant wave height, H_s, peak wave period, T, water depth, h, tide level, and surface longshore current, V_s. The angle of incidence of incoming waves, θ, is given in the local coordinate system such that an angle of zero is orthogonal to the coast aligned with the x-axis. Positive angles are measured counter-clockwise. Wind speed and direction were extracted from meteorological data from the NOAA buoy station 41025, and the 10 minute bursts were averaged over an hour. The wind direction is given such that an angle of zero is coming from the west and is measured counter-clockwise from the x-axis.

Table 5: Hour averaged wind data from NOAA buoy station 41025 and wave data from N1 for February 12.

Feb. 12 (GMT)	**16:00**	**17:00**	**18:00**	**19:00**	**20:00**
$\boldsymbol{H_s\ (m)}$	2.18	2.15	1.88	2.00	1.95
$\boldsymbol{\theta\ (deg)}$	4.29	6.43	8.69	8.34	6.80
$\boldsymbol{T\ (sec)}$	8.52	8.70	8.34	8.81	8.92
$\boldsymbol{h\ (m)}$	4.76	4.60	4.60	4.68	4.86
Tide Level $\boldsymbol{(m)}$	0.03	-0.13	-0.13	-0.05	0.13
$\boldsymbol{V_s\ (m/s)}$	0.50	0.45	0.51	0.53	0.53
Wind Velocity $\boldsymbol{(m/s)}$	6.90	6.63	6.15	6.43	6.35
Wind Direction $\boldsymbol{(deg)}$	271°	267°	260°	251°	255°
$\boldsymbol{dSxx/dx\ \ (kg/ms^2)}$	43.0	42.0	31.6	36.2	34.5
$\boldsymbol{dSxy/dx\ (kg/ms^2)}$	2.2	3.2	3.3	3.6	2.8
$\boldsymbol{\tau_w^s\ (kg/ms^2)}$	0.08	0.07	0.06	0.07	0.07

Table 6: Hour averaged wind data from NOAA buoy station 41025 and wave data from N1 for February 13.

Feb. 13 (GMT)	**13:00**	**14:00**	**19:00**	**20:00**	**21:00**
$H_s\ (m)$	1.69	1.72	1.40	1.39	1.27
$\theta\ (deg)$	17.8	17.0	14.7	14.5	14.3
$T\ (sec)$	7.10	7.30	7.51	7.66	7.82
$h\ (m)$	5.48	5.29	4.59	4.74	4.88
Tide Level (m)	0.74	0.56	-0.14	0.01	0.15
$V_s\ (m/s)$	0.61	0.53	0.40	0.37	0.30
Wind Velocity (m/s)	14.9	13.7	11.0	9.77	9.85
Wind Direction (deg)	290°	296°	314°	319°	327°
$dSxx/dx\ \ (kg/ms^2)$	22.4	23.7	16.5	16.3	13.7
$dSxy/dx\ (kg/ms^2)$	4.9	4.9	2.9	2.9	2.4
$\tau_w^s\ (kg/ms^2)$	0.37	0.31	0.20	0.16	0.16

Using the parameters listed in Tables 5 and 6, the cross-shore component and the longshore component of the cross-shore radiation stress, S_{xx} and S_{xy} respectively, are calculated by

$$S_{xx} = \frac{1}{16}\rho g H_s^2 [(1+G)\cos^2\theta + G] \tag{37}$$

$$S_{xy} = \frac{1}{16}\rho g H_s^2 \cos\theta \sin\theta\,(1+G) \tag{38}$$

where $G = 2kh/sinh2kh$, the wavenumber $k = 2\pi/L$ and is found using linear dispersion, fluid density $\rho = 1030\ kg/m^3$, and gravitational acceleration $g = 9.81\ m/s^2$. To estimate the radiation stress forcing in the surfzone, the gradient of both components of radiation stress are determined by dividing S_{xx} and S_{xy} by the surfzone width which is estimated to be 200 m. The gradient in the cross-shore component, $dSxx/dx$, is an order of magnitude larger than the gradient of the longshore component, $dSxy/dx$ for both days.

The surface wind stress, τ_w^s, is determined by

$$\tau_w^s = C_D \rho_w W^2 \tag{39}$$

where $C_D = 1.3915 \times 10^{-3}$, the air density $\rho_w = 1.2\, kg/m^3$, and W is the wind speed (Svendsen et al., 2002). Comparing the surface wind stress to the gradient in the radiation stress, it is seen that on February 12, τ_w^s is three orders of magnitude less than $dSxx/dx$ and two orders of magnitude less than $dSxy/dx$. Due to stronger winds on February 13, τ_w^s is only two and one orders of magnitude smaller than $dSxx/dx$ and $dSxy/dx$, respectively.

3.2 Morphology from Standard Deviation Images

To qualitatively assess the breaking patterns in the surfzone, image statistics are used. First, the good quality bursts, which are listed in Table 7, are determined to eliminate misleading standard deviation images due to overexposure in the video images. Any image with overexposure cannot be used for calculating image statistics because the bright washed-out bands show very little variance although breaking may be occurring. However, three half hourly based statistical images, which are calculated using a combination of 5 consecutive bursts as described in Section 2.3, are able to be obtained for February 12, 18:00 – 20:00 and February 13, 13:00 and 20:00 – 21:00. The maximum pixel intensity of the three images collectively is used to normalize the statistical images for each day, such that the images corresponding to the three hours are normalized by the same value.

It is noted that the bursts are detrended to correct for lighting changes on a burst by burst basis, as explained in Section 2.3. However, the actual variance between breaking and non-breaking is still expected to be a function of lighting conditions. The raw video is observed to have similar lighting conditions on February 12 between 18:00 and 20:00 making the assumption of consistent variance justified.

Table 7: Bursts useable for calculating image statistics from February 12 and 13.

Useable Bursts for Image Statistics				
Date: Bursts		**Start (GMT)**	**End (GMT)**	**Total Bursts**
Feb. 12:	**32 – 46**	18:27:18	19:51:27	15
	48 – 61	20:03:52	21:22:01	14
Feb. 13:	**2 – 6**	13:30:33	13:54:35	5
	71 – 82	20:25:13	21:31:21	12
	84 – 88	21:43:34	22:07:46	5

Standard deviation images are used to estimate the location of submerged bathymetric features, such as sand bars, by analyzing breaking patterns. Because wave breaking occurs in the surfzone as depth decreases, bright pixel intensities that result from breaking wave crests indicate shallower depth. For the camera setup used in this study, breaking at the shoreline could not be seen due to the oblique viewing angle and the slope of the shoreface. However, wave breaking is seen to occur at an offshore location and an inshore location, as shown in Figure 27. By finding the longshore mean of the pixel intensity, the cross-shore variation of the average standard deviation image is determined. This profile is shown in the top panel of Figure 28, with the bottom panel showing the average bathymetric profile in view of the camera, which is obtained by averaging two LARC surveyed profiles on either side of the camera view. Comparing the breaking patterns to the bathymetry, the seaward breaking occurs over an offshore bar and the shoreward breaking occurs over an inner bar.

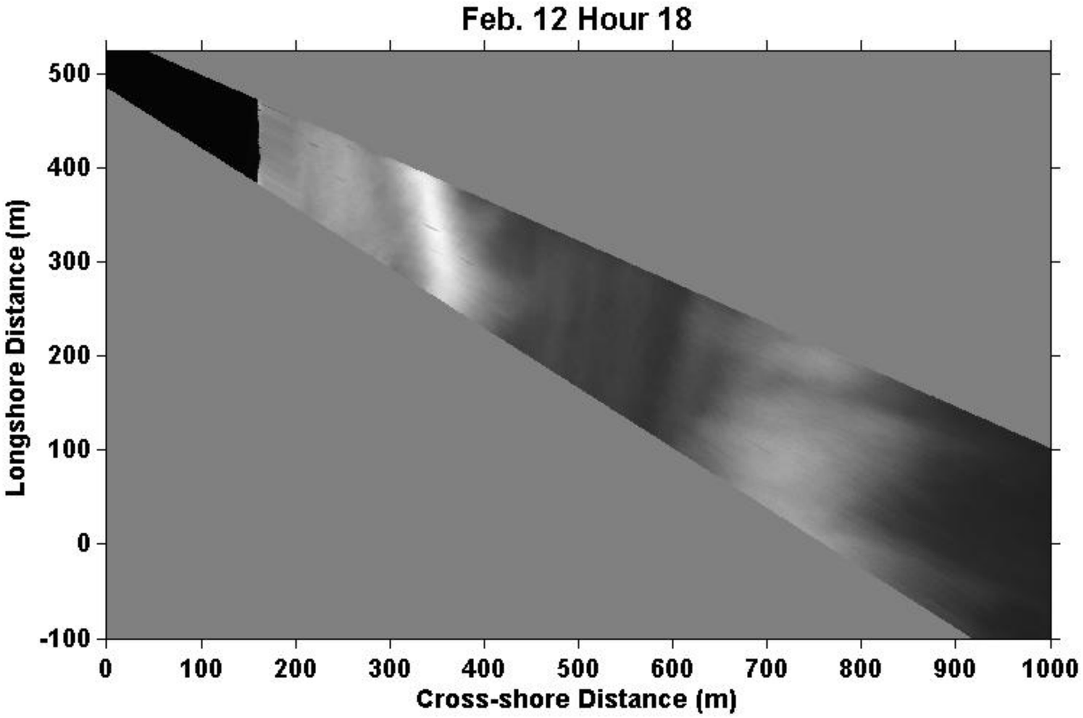

Figure 27: Standard deviation image from February 12 Hour 18 normalized by the maximum pixel intensity of all the variance images.

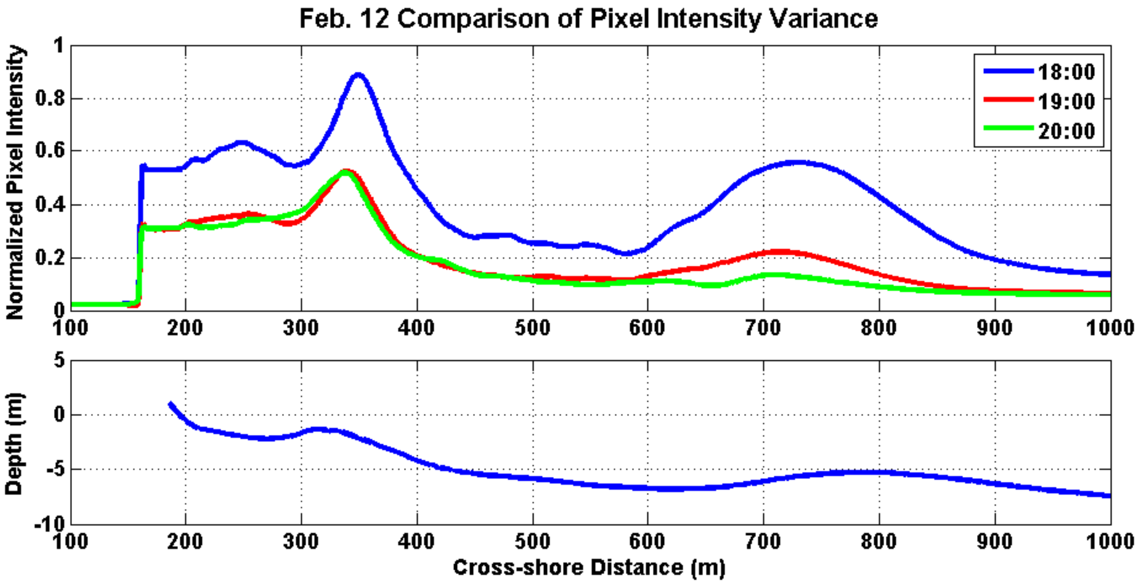

Figure 28: (top) Cross-shore variation of the average pixel intensities of the normalized standard deviation image for February 12, 18:00 – 20:00 (bottom) average bathymetric profile in view of the camera.

Another characteristic of wave breaking observed in standard deviation images is the amount of breaking that occurs. Because the images are normalized by the same maximum pixel intensity, it is assumed that the larger magnitude of intensity during 18:00 indicates more wave breaking than during 20:00. Although the wave heights observed at N1 are similar in magnitude, the tide level causes a significant difference in the breaking patterns as seen in Figure 28, where there is much less wave breaking on the outer bar for 20:00. In the surfzone, dissipation is dominated by wave breaking (Ruessink et al., 2001) and Reniers et al. (2002) shows that the longshore current velocity profile is strongly affected by the amount of dissipation, where more dissipation causes more wave forcing. Therefore, it is deduced that more dissipation and hence more wave forcing is occurring during 18:00.

The standard deviation images corresponding to 13:00 and 21:00 on February 13 can also be used to qualitatively estimate the relative amount and locations of maximum wave breaking. Although the longshore average of the standard deviation in the surfzone during 13:00, shown in Figure 29 is similar during 21:00, the initiation of breaking at the inner bar is located farther offshore during 13:00 than 21:00. This indicates that the larger waves during 13:00 break further offshore than the smaller waves during 21:00. Lastly, very few waves break on the outer bar during 13:00, as shown by the brightest image in Figure 30, and none break offshore of the inner bar during 21:00 as shown by the brightest image in Figure 31. This indicates much smaller wave heights than on February 12 where significant breaking occurs on the outer bar.

Using the assumption that the brighter pixel intensities indicate more wave breaking, Figure 29 shows that the wave breaking between 13:00 and 21:00 on February 13 is nearly the same. From Table 6, the wave height to water depth ratio indicates that the amount of breaking may be very similar between the two hours.

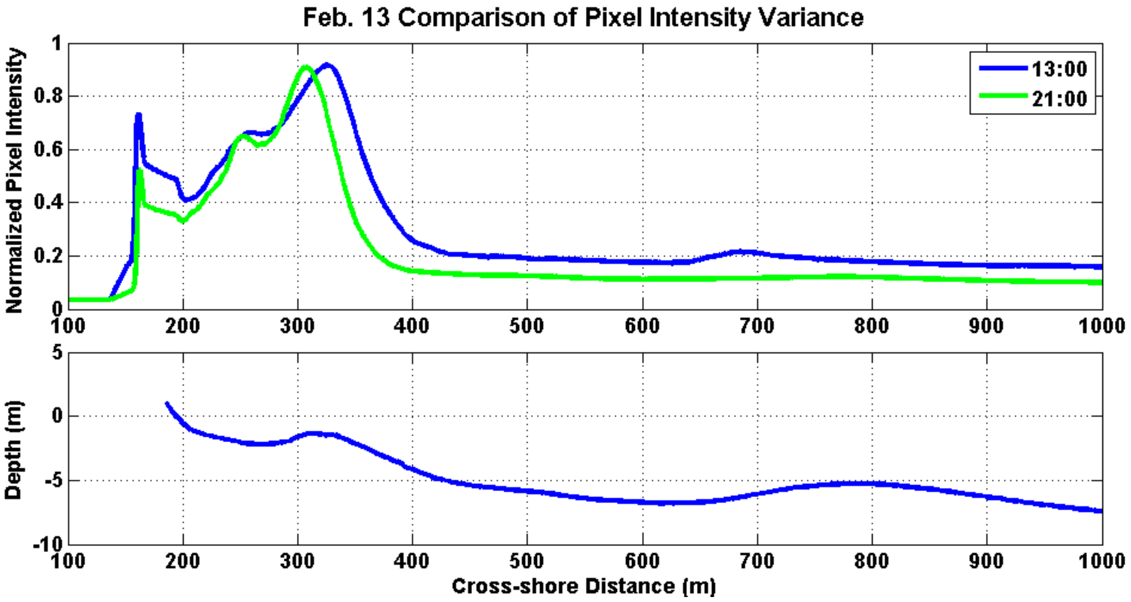

Figure 29: (top) Cross-shore variation of the average pixel intensities of the normalized standard deviation image for February 13, 13:00 and 21:00 (bottom) average bathymetric profile in view of the camera.

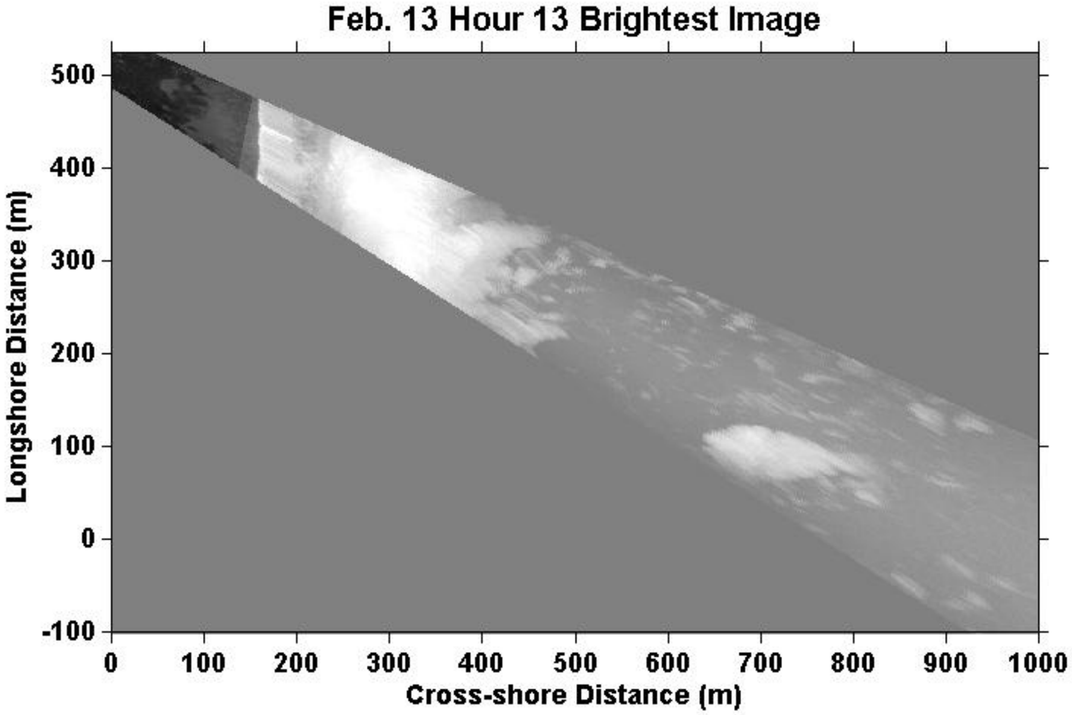

Figure 30: Brightest image from February 13 Hour 13 normalized by the maximum pixel intensity of this image.

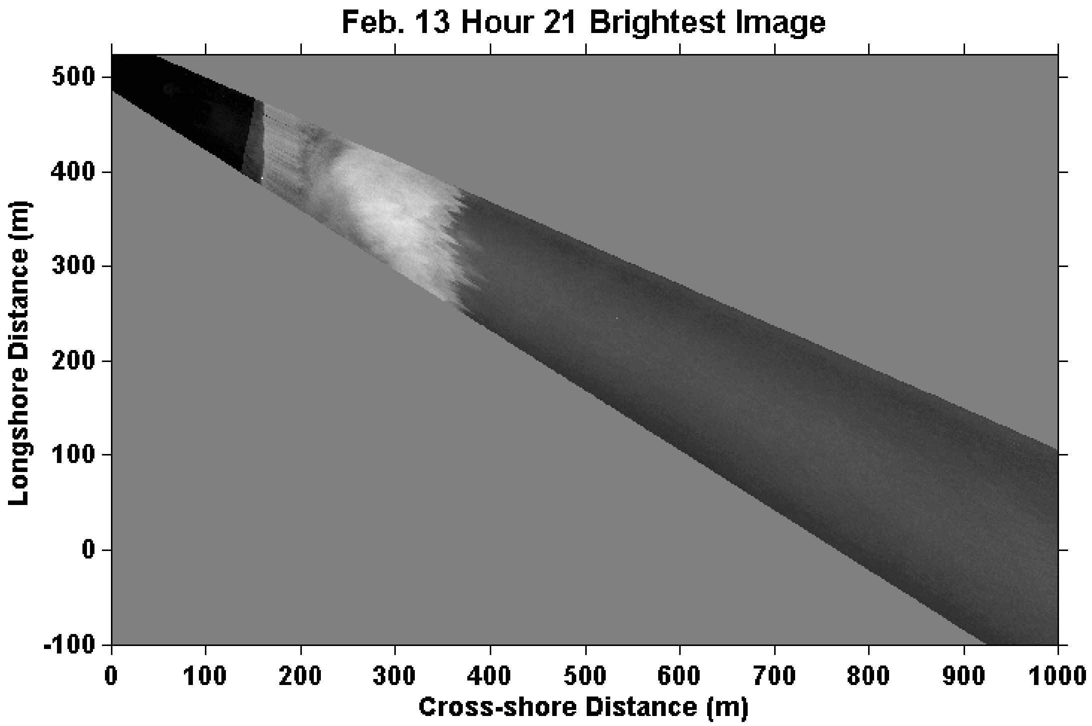

Figure 31: Brightest image from February 13 Hour 21 normalized by the maximum pixel intensity of this variance images.

3.3 Video Estimated Longshore Currents

Longshore currents estimated from the video taken on February 12 and 13 were used to observe how changing wind and wave conditions affect the currents. To reduce biased current estimates from the Optical Current Meter technique due to overexposure in the video images, only the good quality bursts as listed in Table 8 are used. As the video becomes overexposed, the images wash out but the large scale foam features are often present in the timestacks, allowing the OCM technique to be used effectively. Because the OCM technique uses signals in the timestacks of large scale foam features, the quality of the images used for estimating currents is assessed on how well these signals appear in the spectra.

For each of the bursts, 36 longshore arrays are defined in the surfzone and a timestack is created at each array. Then, each of the timestacks is divided into 17 segments, with each segment being 64 m by 38.4 s with 19.2 s overlap, and the OCM technique is applied to each segment to obtain a longshore velocity estimate. A burst average estimate is obtained by averaging the resulting velocities from the 17 segments of the timestack at each longshore array location, resulting in 36 current estimates with 5 m cross-shore spacing throughout the surfzone. To reduce bias estimates from using only a small percentage of the timestack to estimate velocities, a minimum acceptance percentage of 50% of the segments is set for each array.

Table 8: Bursts used for estimating video currents from February 12 and 13.

Useable Bursts for Video Current Estimates				
Date: Bursts		**Start (GMT)**	**End (GMT)**	**Total Bursts**
Feb. 12:	**2 – 57**	15:24:01	20:57:59	56
Feb. 13:	**2 – 13**	13:30:33	14:36:39	12
	59 – 86	19:13:06	21:55:36	28

An example of the burst averaged longshore velocities is given in Figure 32, where the cross-shore variation is realistic but has significant variability between bursts. Hour averaged longshore velocities, which include much less noise than burst averaged velocities due to the larger data set being averaged, are calculated by averaging the burst averaged currents that correspond to that hour. The cross-shore profile for hour averaged velocities is also shown in Figure 32 and is smoother than the burst averaged current profile. The maximum longshore current velocity shown in Figure 33 is located well shoreward of the most persistent breaking, which is indicated by the bright pixel intensities around cross-shore location 350 m. Based on results from Haller et al. (2002), the shoreward shift to the trough of the longshore currents could be indicative of an additional pressure gradient forcing.

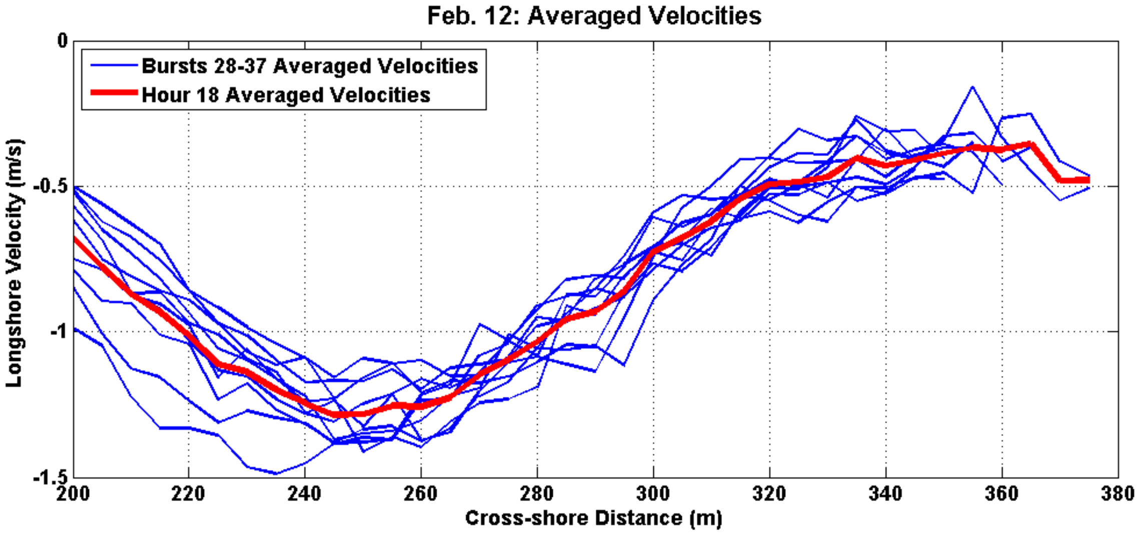

Figure 32: Cross-shore variation of burst averaged and hour averaged longshore current velocities for February 12, Bursts 28 – 37 corresponding to Hour 18.

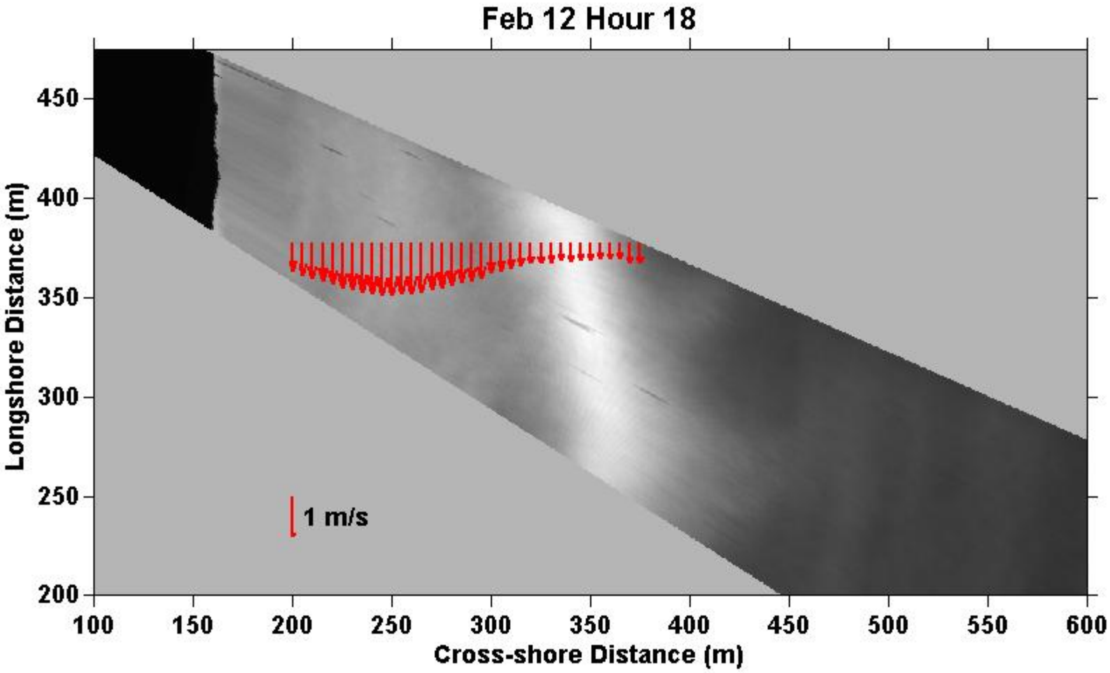

Figure 33: Cross-shore variation of hour averaged longshore current velocities for February 12, Hour 18 on the corresponding standard deviation image.

The longshore current estimates from the video for February 12 are shown in Figure 34. The strongest hour averaged currents occur at 18:00 peaking at nearly 1.3 m/s while the weakest hour averaged currents occur at 20:00 with a peak magnitude of about 1.15 m/s. Analyzing the wind and wave conditions from Table 5, 18:00 has the smallest wave height, the largest angle of incidence, the shortest period, the weakest wind velocity, and a water level near low tide. These parameters cause 18:00 to have the smallest gradient of the cross-shore component of radiation stress and surface wind stress, but the gradient of the longshore component of radiation stress is relatively large causing stronger longshore currents. This result suggests that the magnitude of the currents is more strongly dependent on wave angle than on wave height.

Analyzing the conditions for 16:00, which has the largest H_s and wind velocity but the smallest θ, it is seen that $dSxx/dx$ is the largest of any other hour, but $dSxy/dx$, which drives longshore currents, is the smallest. Because the currents estimated during 16:00 are the second weakest currents of any other hour, it may be deduced that the magnitude of the currents are weaker due to smaller $dSxy/dx$ which seems to be a stronger function of wave angle than of wave height. Looking at the other hours, similar trends for the relationship between the wave angle and the magnitude of the longshore currents are apparent.

From this analysis, it is concluded that the currents have the strongest dependence on wave angle, which was also determined by Park and Wells (2005), and wave height, which creates more wave forcing in the surfzone.

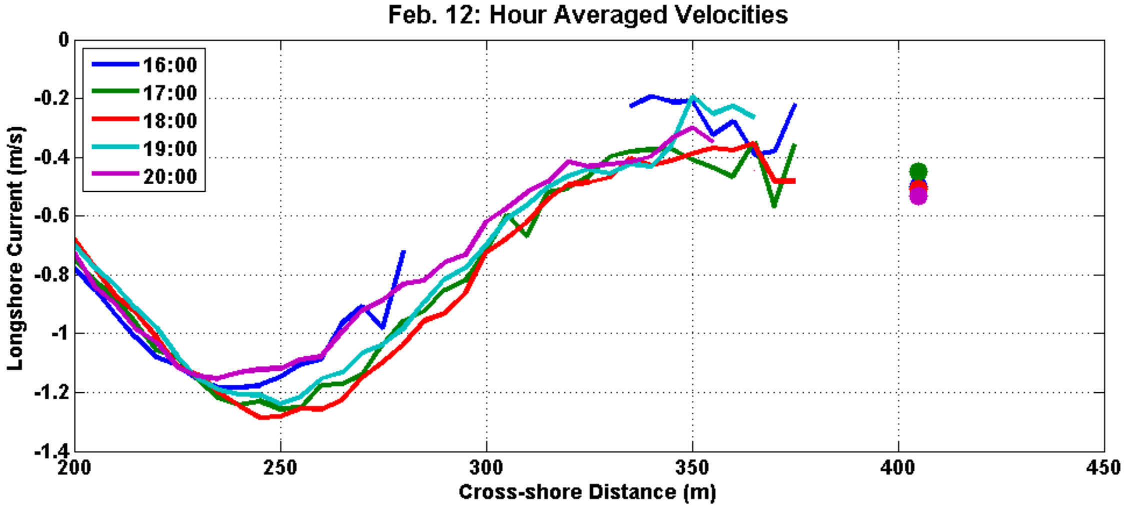

Figure 34: Hour averaged longshore velocities estimated from video for February 12 given in GMT where lines are video estimated currents and dots are instrument measured currents.

As the Nor'easter storm continued on February 13, the wind and wave conditions changed significantly from February 12 as shown in Table 6. Although wave heights are much smaller and decrease throughout the day, incoming waves approach from a much more oblique angle. Although the wind velocity is stronger, the surface wind stress is still very small compared to the gradients of radiation stress forcing.

From Figure 35, the strongest currents estimated by video and measured by N1 are during 13:00 while the weakest currents are during 21:00. During 13:00, the relatively large H_s, the largest θ, strongest wind velocity, and the highest water level are experienced compared to the other hours for which currents are estimated. The gradient of the longshore component of the radiation stress during 13:00 is also seen to be a maximum for the day, indicating that the strong currents estimated are due to the larger wave height and wave angle. However, 21:00 has the smallest H_s and the smallest wave angle, causing $dSxy/dx$ to be a minimum. Therefore, the currents estimated on February 13 behave similarly to the currents on February 12 since they increase with an increase in $dSxy/dx$, which is caused by larger wave height and wave angle.

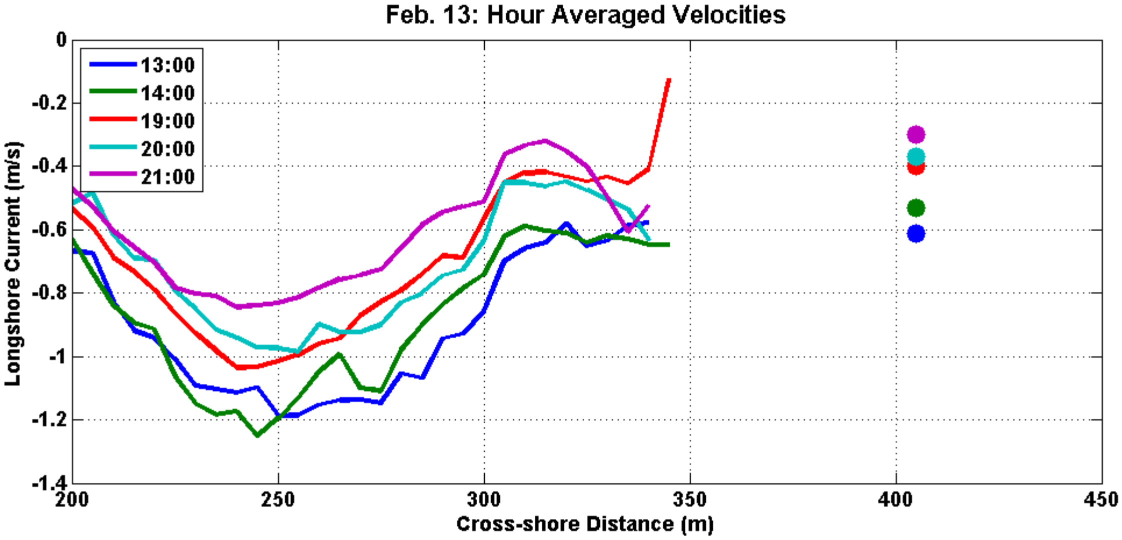

Figure 35: Hour averaged longshore velocities estimated from video for February 13 given in GMT where lines are video estimated currents and dots are instrument measured currents.

Comparing the maximum current on February 12 to the maximum current on February 13, February 12 has larger currents shoreward of about 300 m but February 13 has larger currents seaward of this location. Figure 33 shows the preferential wave breaking location, which is representative of the location of maximum radiation stress forcing, to be around 350 m. The estimated longshore radiation stress gradient for February 13 (Table 6) is larger than the longshore radiation stress gradient for February 12 (Table 5). Therefore, the video estimated currents seaward of 300 m are assumed to be driven by radiation stress gradients, but the currents shoreward of that location are assumed to be driven by another forcing mechanism.

3.4 Summary

Using in situ data for the duration of the experiment, a Nor'easter storm event occurring on February 12 and 13 is isolated. This event is chosen because the north side of Cape Hatteras Point is strongly affected by the wind and wave conditions, good quality video is available during this event, and the nearshore instrument, N1, was deployed prior to the arrival of the storm. The hour averaged wind and wave conditions are used to calculate the gradients in cross-shore and longshore radiation stress and the surface wind stress. The surface wind stress for February 12 and 13 is at least one order of magnitude less than the wave forcing and is neglected in the analysis.

Standard deviation images are used to indicate the presence of an inner and outer bar in view of the camera through wave breaking patterns and to qualitatively assess the amount of wave breaking from one hour to the next on a given day. Because waves are larger on February 12, the outer bar is clearly indicated by wave breaking around 720 m and the location of an inner bar is determined to be 350 m, which is similar to the locations of the bars shown in LARC bathymetry data. February 12 also shows that more wave breaking occurs during the hour with greatest longshore velocities than during the hour with the weakest longshore velocities because the average pixel intensities are greater. However, February 13 shows about the same amount of wave breaking for the hours of strongest and weakest currents, but a greater wave angle, which is not observed by pixel intensities, is the cause of the stronger currents.

Comparing the in situ data to video estimated currents, the video estimated longshore currents are greatly influenced by $dSxy/dx$. Although larger wave height and lower water depth increase the amount of forcing available to drive currents, the angle of incidence of incoming waves is shown to greatly increase $dSxy/dx$ and longshore currents as the angle becomes more oblique. The currents seaward of location 300 m is assumed to be radiation stress driven since preferential breaking occurs near that location and the larger radiation stress gradient on February 13 forces larger currents. Shoreward of 300 m, the currents are assumed to be driven by another mechanism since February 12 has larger currents in that region, but smaller radiation stress forcing compared to February 13.

CHAPTER 4

MODEL RESULTS

Although the wave height, water depth, and wave angle are shown to greatly affect the gradient in cross-shore and longshore radiation stress, the location of the maximum currents also suggests an additional longshore pressure gradient force driving the flow. To more robustly evaluate the forcing of the currents observed in the video and to evaluate the presence of a longshore pressure gradient, a numerical model is used to simulate nearshore waves and currents. The observed offshore wind and wave conditions during CH 2010 and two bathymetric profiles, one which intersects a trough and one which crosses a terrace, are used as inputs into the model to quantify a longshore pressure gradient due to differences in wave set-up.

4.1 Model Description

The Nearshore Community Model (NearCoM) developed by the National Oceanographic Partnership Program (NOPP) simulates waves, currents, sediment transport and bathymetric change. A master program acts as the “backbone” of the model system, governing the time stepping as well as application and information transfer between a suite of modules. Each module is used to simulate a different subset of physical processes and is used collectively to simulate the nearshore ocean. Since sediment transport and bathymetric changes are not included in this study, only the wave module REF/DIF-S and the circulation module SHORECIRC (SC) are utilized to simulate currents and mean water level variations. Further details on the NearCoM master program may be found in Shi et al. (2005).

4.1.1 Wave Module REF/DIF-S

REF/DIF-S (Kirby et al., 2004) is an extension of the combined refraction/diffraction model, REF/DIF-1 by Kirby and Dalrymple (1994). To represent a random sea, REF/DIF-S generates a 2D spectrum consisting of frequency and direction components that evolves as the model progresses forward in space to account for refraction, shoaling, energy dissipation and diffraction processes. The module initializes with user specified wave conditions at the offshore boundary of the domain and solves the mild slope equation for each possible combination of frequency and direction as the model progresses forward in space until the shoreward end of the grid is reached.

The energy dissipation in a breaking wave is modeled as a periodic bore using the mechanism by Thornton and Guza (1983). This method estimates the breaking wave dissipation by assuming a Rayleigh distribution for the waves and weighting it to find the probability of wave breaking at that given wave height. The dissipation per unit area, D, is calculated as

$$D = \frac{3\sqrt{\pi}}{16}\rho g B^3 \bar{f}\frac{H_{rms}^3}{h}Q_b \tag{40}$$

where ρ is fluid density, g is gravitational acceleration, B is a breaking wave coefficient representing the intensity of breaking, $\bar{f}$ is the average wave frequency, H_{rms} is root mean square wave height and h is the water depth. The fraction of breaking waves due to the local water depth, Q_b, is defined as

$$Q_b = \frac{H_{rms}^4}{\gamma^4 h^4} \tag{41}$$

where γ is the wave height to water depth ratio for breaking waves.

To account for wave persistence or the gradual decrease in dissipation as the water depth increases (such as on a bar/trough system), the persistence length method as described in Cambazoglu and Haas (2011) is used. To accomplish this, Q_b is modified to include the dissipation contribution of any newly breaking wave within a distance, defined as the persistence length

$$L_b = C_p \frac{8\pi^4(1+G)(H_s)^2}{g^2 k T^4} \tag{42}$$

where L_b is the persistence length, C_p is the persistence length calibration constant, $G = 2kh/sinh2kh$, k is the wavenumber, T is wave period and H_s is the significant wave height. This new value of Q_b is substituted into Equation (40) allowing for a gradual decrease in dissipation as the water depth increases in the trough.

The fraction of breaking waves is also modified for the contribution of the wave roller to the radiation stresses and short-wave mass fluxes. Using the roller model as described in Cambazoglu and Haas (2011), the distance over which the roller is developing, or the transition zone in which a wave transforms from a non-breaking state to a fully developed bore, is specified by a roller lag length, L_r, given by

$$L_r = C_r h \left(\frac{H_{rms}}{L}\right)^3 \tag{43}$$

where C_r is the roller lag length calibration constant and H_{rms}/L is the wave steepness. Q_b is then modified proportional to L_r such that the momentum transfer to the waves from the roller is reduced throughout the transition zone, varying from zero at the initiation of breaking to full contribution at the end of the roller lag length.

Further details of the wave module may be found in Kirby et al. (2004) with the modifications described further in Cambazoglu and Haas (2011).

4.1.2 Circulation Module SHORECIRC

To describe the governing equations for the circulation module, the definitions illustrated in Figure 36 are used. The coordinate system is such that x and u are the cross-shore direction and velocity increasing positively shoreward, y and v are the longshore direction and velocity which increases positively into the page, and z and w are the vertical direction and velocity increasing positively upward. The local water depth, h, is defined as

$$h = h_o + \bar{\zeta} \tag{44}$$

where h_o is the still water depth, $\bar{\zeta}$ represents the mean water level (MWL) and the overbar denotes short wave averaging. The current velocity as defined in SC consists of a depth uniform component and a depth-varying component. The wave height is given by H, the volume flux due to short wave motion is defined as $Q_{w\alpha}$ and ζ is the instantaneous free water surface relative to the still water level (SWL).

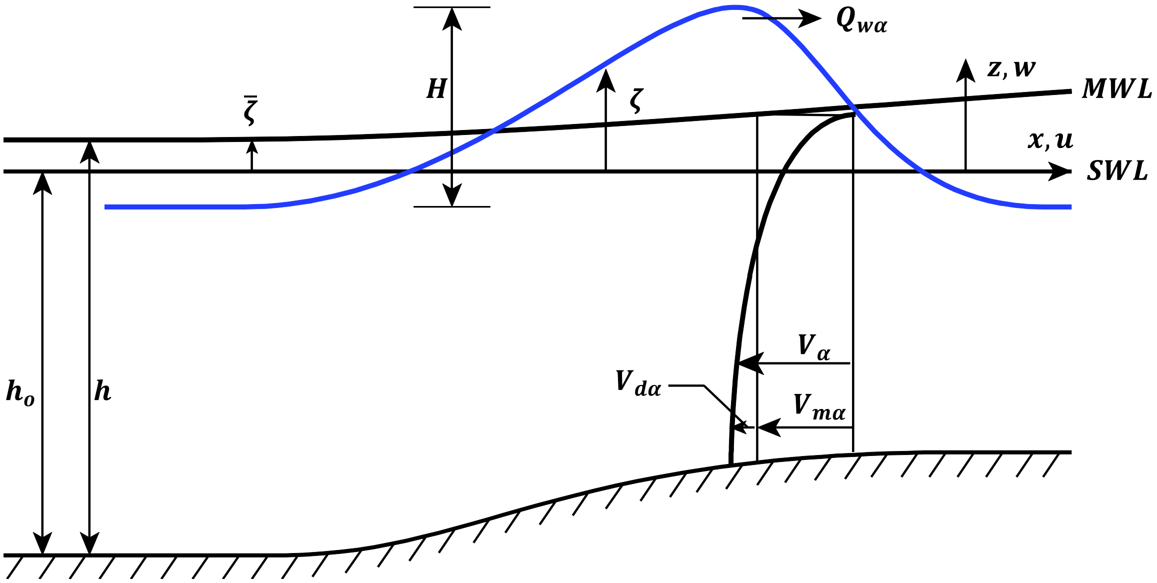

Figure 36: Definition sketch for the SC governing equations.

The quasi three-dimensional nearshore circulation model SHORECIRC solves the short wave-averaged nearshore flow equations for the mean water level and nearshore currents. The instantaneous total fluid velocity has contributions from the turbulent fluid velocity, the short wave velocity (u_w), the depth-averaged current, and the depth-varying current (V_d).

The depth-integrated wave-averaged shallow water equations which SC solves are continuity given by

$$\frac{\partial \bar{\zeta}}{\partial t} + \frac{\partial \overline{Q_\alpha}}{\partial x_\alpha} = 0 \tag{45}$$

and the horizontal momentum equations defined as

$$\begin{aligned} \frac{\partial \overline{Q_\alpha}}{\partial t} + \frac{\partial}{\partial x_\beta}\left(\frac{\overline{Q_\alpha}\,\overline{Q_\beta}}{h}\right) + \frac{\partial}{\partial x_\beta}\overline{\int_{-h_o}^{\zeta} V_{d\alpha} V_{d\beta}\, dz} + \frac{\partial}{\partial x_\beta}\overline{\int_{\zeta_t}^{\zeta} u_{w\alpha} V_{d\beta} + u_{w\beta} V_{d\alpha}\, dz} &= \\ -gh\frac{\partial \bar{\zeta}}{\partial x_\alpha} - \frac{1}{\rho}\frac{\partial}{\partial x_\beta}\left(S_{\alpha\beta} - \overline{\int_{-h_o}^{\zeta} T_{\alpha\beta}\, dz} \right) - \frac{\tau_\alpha^B}{\rho} \end{aligned} \tag{46}$$

where $\partial/\partial t$ is the derivative with respect to time, Q_α is the total volume flux, β denotes x or y, $S_{\alpha\beta}$ is the radiation stress, $T_{\alpha\beta}$ is the Reynolds stress and τ_α^B is the bottom shear stress. In SC, the spatial derivatives are represented by a central finite difference scheme while the time derivatives are solved using a Predictor-Corrector scheme with the Adams-Bashforth predictor and the Adams-Moulton corrector (Svendsen et al., 2002).

The eddy viscosity, ν_t, is determined from combined contributions from Svendsen and Putrevu (1994) and Coffey and Nielsen (1984) for outside the surfzone and from a modified form of Battjes (1975) inside the surf zone. The resulting equation is

$$\nu_t = C_1 \kappa \sqrt{\frac{f_w}{2}} u_0 h + MH\left(\frac{D}{\rho}\right)^{1/3} + \nu_{t,0} + \nu_s \tag{47}$$

where κ is the von Karman constant ($\kappa \cong 0.4$), f_w is the friction factor, u_0 is the short-wave particle velocity amplitude evaluated at the bottom, $\nu_{t,0}$ is the background eddy viscosity, ν_s is the Smagorinsky eddy viscosity, and C_1 and M are eddy viscosity coefficients (Svendsen et al., 2002).

The short wave-averaged bottom shear stress is defined as

$$\bar{\tau}_{\alpha}^{B} = \frac{1}{2}\rho f_w u_0(\beta_1 V_{b\alpha} + \beta_2 u_{0\alpha}) \tag{48}$$

where $V_{b\alpha}$ is the bottom velocity in the current motion. β_1 is the weight factor for the current motion defined as

$$\beta_1 = \overline{\left[\left(\frac{V_b}{u_0}\right)^2 + 2\frac{V_b}{u_0}\cos\theta\cos\mu + \cos^2\theta\right]^{1/2}} \tag{49}$$

and β_2 is the weight factor for the wave motion defined as

$$\beta_2 = \overline{\cos\theta\left[\left(\frac{V_b}{u_0}\right)^2 + 2\frac{V_b}{u_0}\cos\theta\cos\mu + \cos^2\theta\right]^{1/2}} \tag{50}$$

where θ is the short-wave phase angle and μ is the angle between the short-wave direction and the current velocity at the bottom (Svendsen 2006).

The friction factor, f_w which is user defined and assumed constant, can be determined from the Jonsson diagram (Jonsson, 1966) for the grain size and velocities measured during CH2010. To properly use this diagram, the method described in Svendsen (2006) is followed. The velocity amplitude, U_o, which is defined as $U_o = H/2\sinh kh$ and the particle excursion amplitude, a_b which is defined as $a_b = U_o/\omega$ where $\omega = 2\pi/T$ or wave frequency, are determined from in situ instrument data. The wall roughness, k_n, is related to grain size, d_{50}, by assuming a flat smoothed sand bed as a lower limit such that $k_n = d_{50}$ and assuming a more rough bed as an upper bound such that $k_n = 2.5d_{50}$ (Johns, 1983). The viscosity, ν, is assumed to be $1.05 \times 10^{-6}\, m^2/s$ for saltwater at 20°C and the Reynolds number, RE, is determined by $RE = U_o a_b/\nu$. The range is calculated to be from 0.007 to 0.02 by using the extreme values given in Table 9 to obtain a minimum and maximum friction factor.

Table 9: Extreme values used with the Jonsson diagram to determine the friction factor range.

	Minimum	**Maximum**
$\boldsymbol{H(m)}$	1	0.5
$\boldsymbol{h_o\ (m)}$	2	3
$\boldsymbol{T\ (s)}$	8	6
$\boldsymbol{U_o\ (m/s)}$	0.52	0.09
$\boldsymbol{d_{50}\ (mm)}$	0.2	0.2
$\boldsymbol{k_n\ (mm)}$	0.2	0.5
$\boldsymbol{RE\ (-)}$	3.3×10^5	8.0×10^3
$\boldsymbol{a_b/k_n\ (-)}$	3.3×10^3	179
$\boldsymbol{f_w\ (-)}$	**0.007**	**0.02**

The offshore boundary condition is an absorbing/generating boundary condition while the shoreline boundary condition specifies no flux following the still water line. The location of the shoreline is identified by finding the last grid point where the depth exceeds the minimum depth. Periodicity is required for the lateral boundaries such that the flows at these boundaries are equivalent (Svendsen et al., 2002).

SHORECIRC is a quasi three-dimensional model because it accounts for lateral mixing from the vertical variation of the currents, by combining the numerical solution for the depth-integrated 2D horizontal equations with a semi-analytical solution for depth-varying currents. This approach allows the 3D dispersive mixing coefficients to be expressed in terms of depth uniform flow properties. The turbulent stresses are determined by an eddy viscosity model that assumes quasi-steady flow to represent the solution in a polynomial expression for the depth-varying currents in terms of the depth-integrated currents. Further details of SC may be found in Svendsen et al. (2002).

4.2 One-Dimensional Modeling

The nearshore flows for four cases in which video and in-situ instrumentation measurements exist are simulated using one-dimensional (1D) SC and REF/DIF-S. The hour-averaged conditions for each case, listed in Table 10, are used as model inputs representative of actual storm event conditions. For the specified day and hour, wave data is obtained from in situ instrument O3, located at 35.264 N 75.508 W and shown in Figure 3, and is shoaled in to the offshore model boundary using Snell's Law and linear wave shoaling. These parameters include significant wave height, H_s, wave period, T, and tidal level. The angle of incidence of incoming waves, θ, is determined using Snell's Law from the in situ instrument N1, also shown in Figure 3, and is given in the local coordinate system such that an angle of zero is orthogonal to the coast aligned with the model x-axis. Positive angles are measured counter-clockwise. Wind speed and direction are extracted from meteorological data from NOAA buoy station 41025 where wind direction is given in the SC coordinate system such that an angle of zero is coming from the west and is measured counter clockwise from the x-axis.

Cases 1 and 2 represent data from February 12, hours 18 and 16 respectively, and have larger wave heights and longer periods than cases 3 and 4. Winds are from the north – northeast and are relatively weak at 6 to 7 m/s. Cases 3 and 4 are representative of conditions from February 13, hours 14 and 19 respectively, with waves approaching much more obliquely than on February 12.

Table 10: Wind and wave data defining four cases.

	Case 1	**Case 2**	**Case 3**	**Case 4**
Time (GMT)	Feb 12, Hr 18	Feb 12, Hr 16	Feb 13, Hr 14	Feb 13, Hr 19
H_s (m)	2.45	2.54	2.13	1.93
θ (deg)	10.6°	5.19°	20.1°	17.8°
T (sec)	9.56	9.75	6.73	7.27
Tide Level (m)	-0.19	-0.04	0.49	-0.19
Wind Velocity (m/s)	6.15	6.90	13.7	11.0
Wind Direction (deg)	260°	271°	296°	314°

Bathymetric profiles are isolated from survey data at two locations on either side of the camera view and are shown in Figure 37. The standard deviation image shows longshore variability in breaking, indicating a longshore non-uniform inner bar. The northern-most profile on the left side of the camera view is represented by the blue line in Figure 37 and intersects a terrace as shown in Figure 38. The southern-most profile on the right side of the camera view is represented by the green line in Figure 37 and intersects a trough as shown in Figure 38. The average distance between the terrace and trough profiles is 65 m and the offshore bathymetry is assumed to be the same for both.

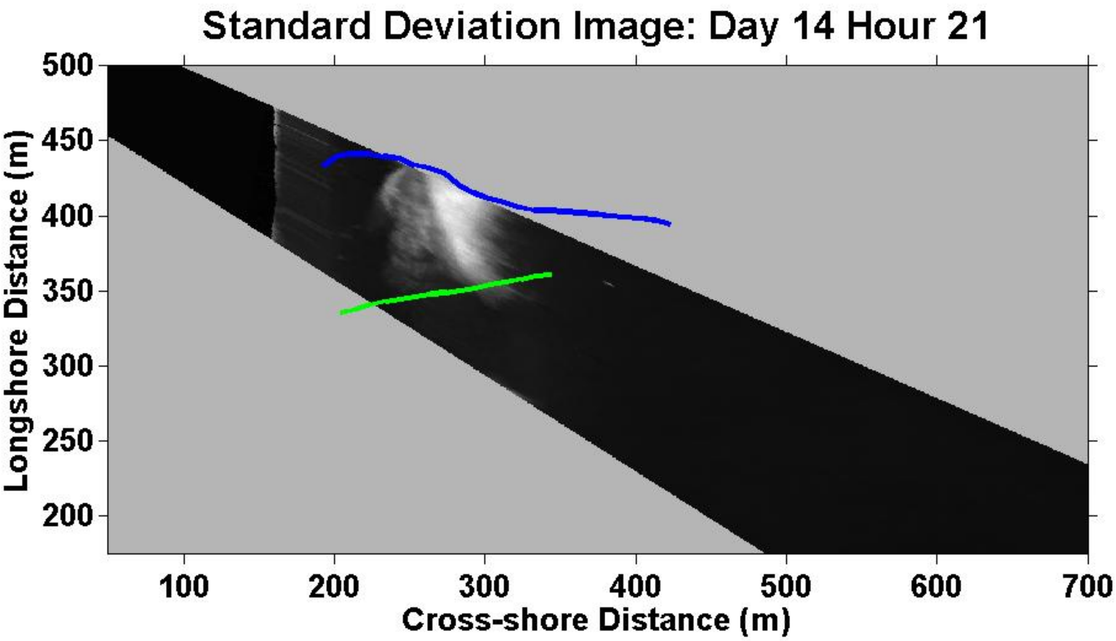

Figure 37: Bathymetric profiles on the north (blue) and south (green) sides of the camera view overlay a standard deviation image from February 14, Hour 21.

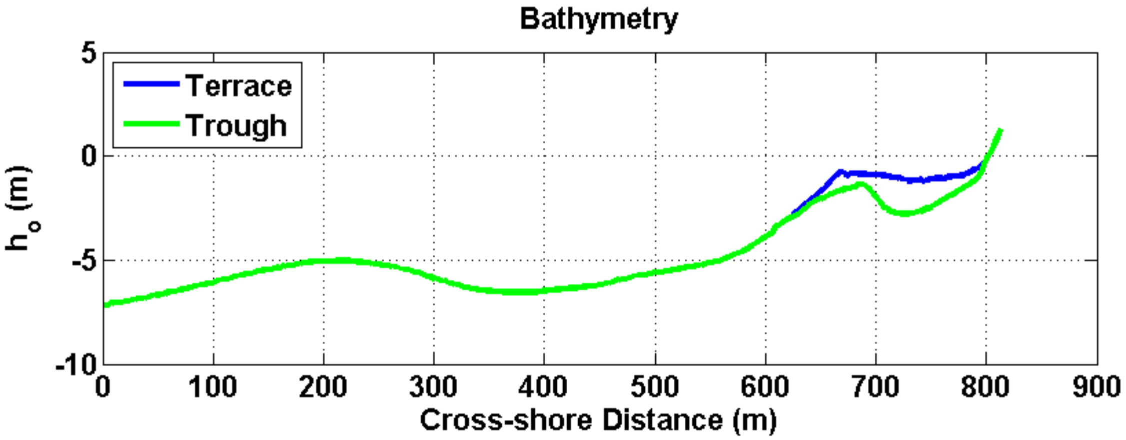

Figure 38: Bathymetric profiles that represent a terrace (blue) and a trough (green).

A moving shoreline boundary condition is used with a minimum depth criterion of 0.1 m to determine the last wet point for numerical computations. The numerical grid has 3 m spacing and a total of 272 points in the x-direction and 5 m spacing and a total of 11 points in the y-direction. The model is forced to be longshore uniform to produce a 1D result. The eddy viscosity coefficients, C_1 and M, are set as 0.06 and 0.075, while $C_r = 1$, $C_p = 4800$, $f_w = 0.007$ and $\gamma = 0.6$. The total time for model simulation is 3600 s with a time step of 0.15 s, which allows the model to achieve steady state conditions.

The results of the simulations for case 1 are shown in Figure 39. For both profiles, the model clearly overpredicts the wave height (Figure 39 (a)) compared to the instrument (black star). The magnitude of the currents, shown in Figure 39 (b) are significantly underpredicted, particularly in the trough, compared to the video (black line) and at the offshore edge of the inner bar, or cross-shore location about 600 m, compared to the instrument (black star).

The root mean square (RMS) difference between the video and model currents, RMS_v, is found by

$$RMS_v = \sqrt{\frac{1}{N}\sum_{j=1}^{N}[V_{vid}(j) - V_{mod}(j)]^2} \tag{51}$$

where N is the total number of points, j is the indices, V_{vid} are the video estimated currents and V_{mod} are the model simulated currents. The cross-shore spacing is taken to match the video at 5 m. As shown in Table 11, for case 1, $RMS_v = 0.74$ m/s for the terrace profile and $RMS_v = 0.64$ m/s for the trough profile, showing slightly better agreement for currents from the video and trough profile compared to the video and terrace profile. In the trough area only, which corresponds to cross-shore distance 700 m to the shoreline, the RMS difference for the terrace profile is found to be 0.97 m/s and the trough profile is 0.85 m/s. The agreement is decreased significantly for both profiles, indicating the simulated currents in the trough differ greatly from the video observed currents, as seen in Figure 39 (b).

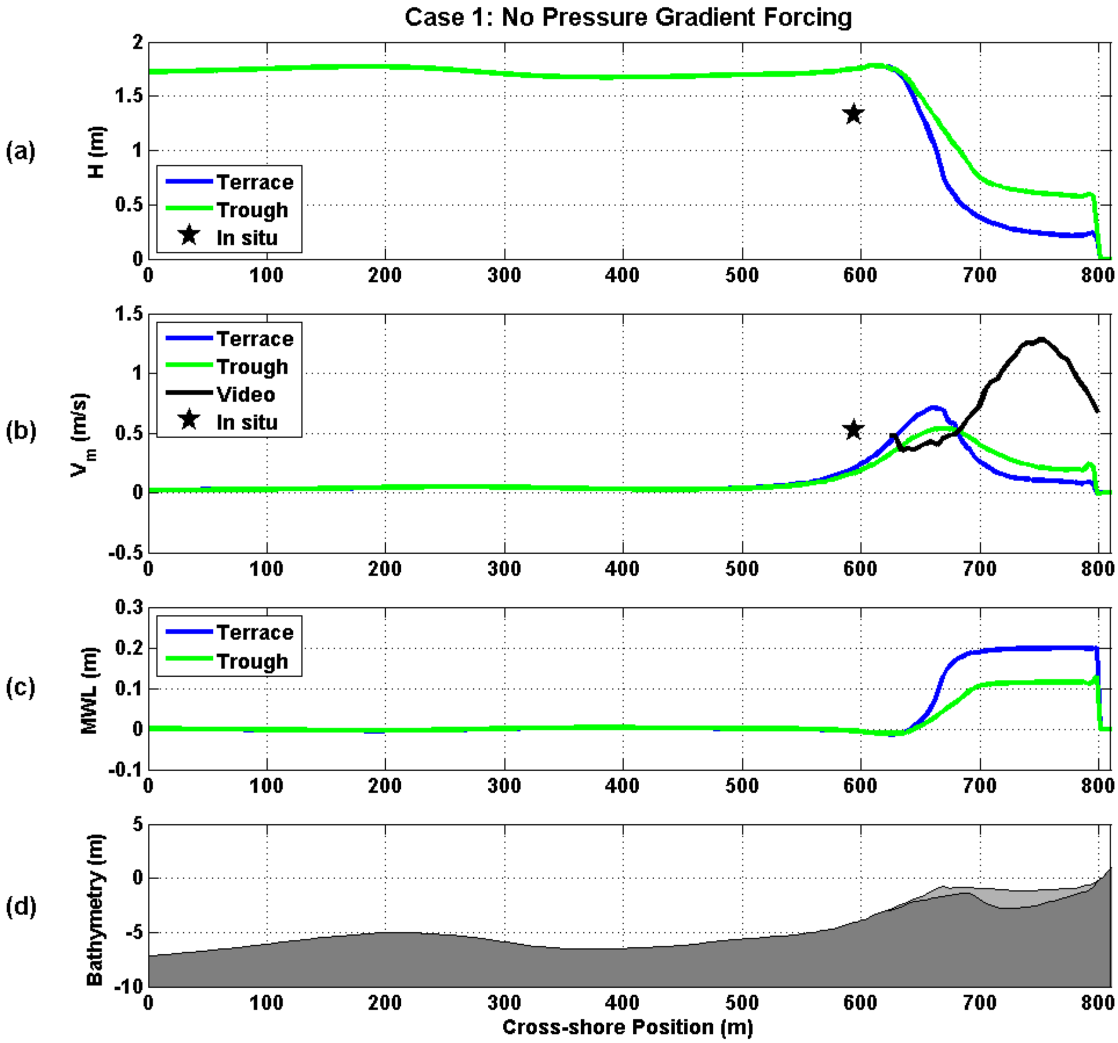

Figure 39: Cross-shore variation of (a) H, (b) V_m, (c) MWL, and (d) h_o for the terrace (light gray) and trough (dark gray) profiles for case 1.

The MWL variation for the terrace and trough profiles is shown in Figure 39 (c). The MWL differs because the terrace bathymetric profile, which is shown in Figure 39 (d) as the light gray shaded area, is shallower than the trough profile in the nearshore region, which is the dark gray shaded area. To illustrate the connection between the bathymetry and the MWL, the dominant terms in the cross-shore momentum balance are shown in the top panel of Figure 40. The primary balance is between the radiation stress forcing and the pressure gradient, which means more radiation stress forcing will cause a larger pressure gradient. Figure 41 compares the radiation stress forcing at both profiles and shows that there is more forcing along the terrace profile than along the trough profile. Consequently, this larger radiation stress forcing is balanced by a larger cross-shore pressure gradient, which is also shown in Figure 41. The increase in radiation stress forcing is due to more energy dissipation, which is generated by wave breaking, for the terrace profile as shown in Figure 42. More dissipation results from shallower depth because it is inversely proportional to the water depth as defined in Equation (40). Therefore, the MWL is higher for the terrace profile than the trough profile, because of the stronger cross-shore pressure gradient generated from the balance between the larger radiation stress forcing due to higher dissipation induced by the shallower bathymetry.

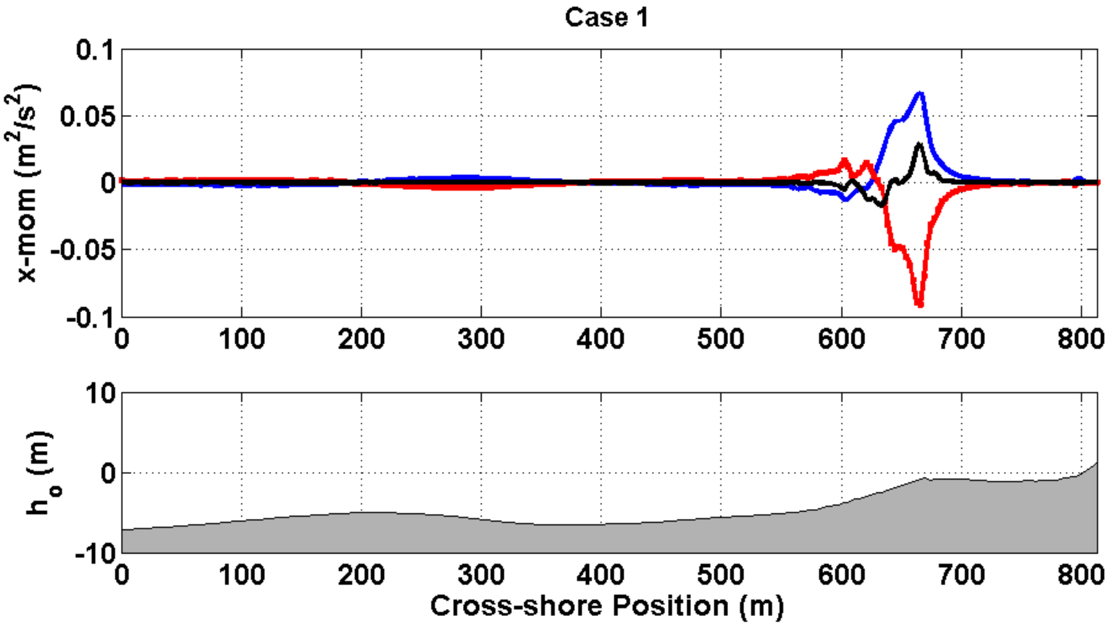

Figure 40: The top panel shows dominant terms in the cross-shore momentum balance for the terrace profile including $\frac{-1}{\rho}\frac{\partial S_{xx}}{\partial x}$ (blue), $-gh\frac{\partial \bar{\zeta}}{\partial x}$ (red) and 3D dispersion (black) for case 1 with no longshore pressure gradient forcing. Bathymetry for the terrace profile is shown in the bottom panel.

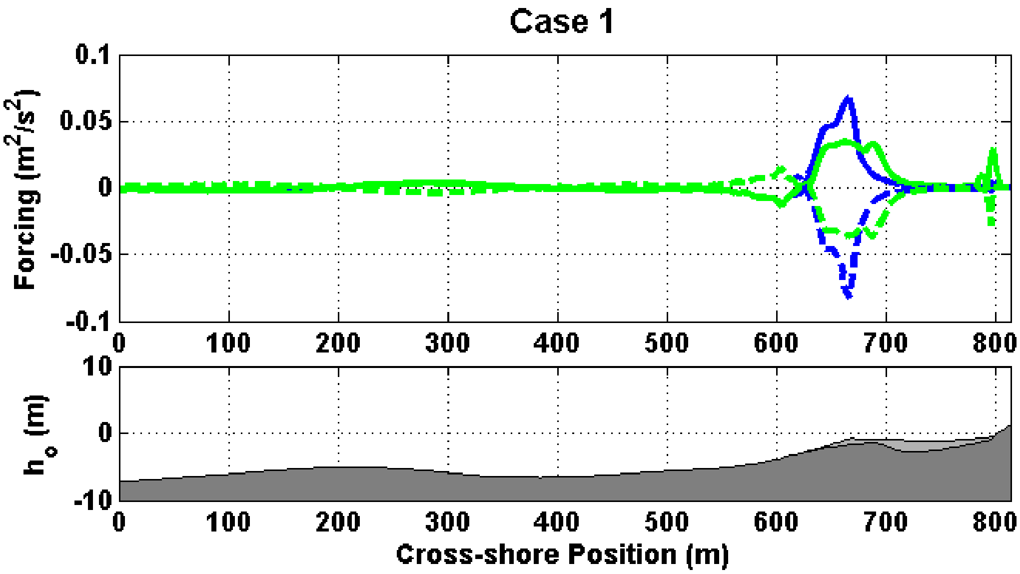

Figure 41: The cross-shore variation of the radiation stress gradient, $\frac{-1}{\rho}\frac{\partial S_{xx}}{\partial x}$ (solid), and the cross-shore pressure gradient, $-gh\frac{\partial\bar{\zeta}}{\partial x}$ (dash), for the terrace (blue) and trough (green) profiles for case 1 is shown in the top panel, with the terrace profile, shaded light gray, and the trough profile, shaded dark gray, in the bottom panel.

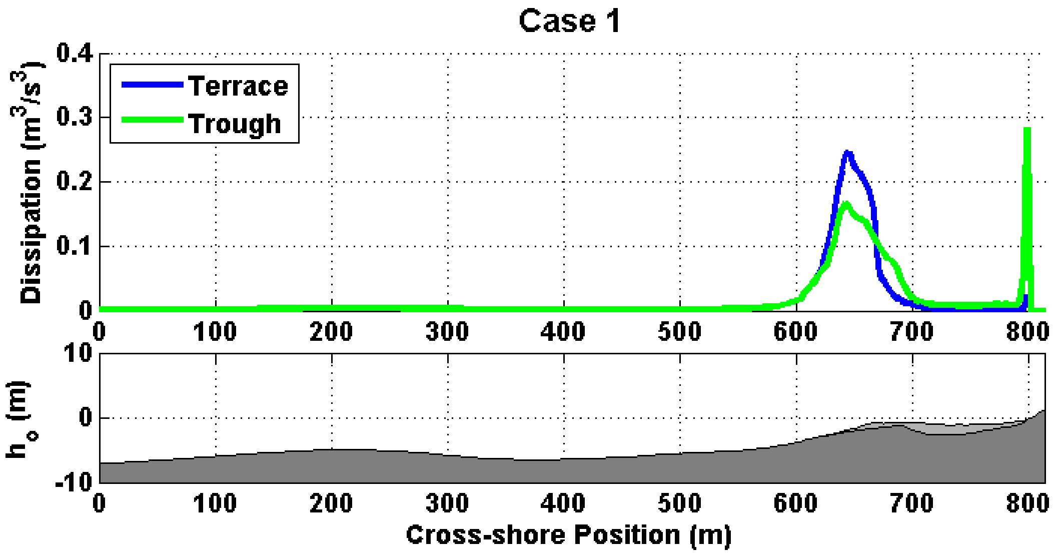

Figure 42: The cross-shore variation of the dissipation due to wave breaking for the terrace and trough profiles under case 1 conditions is shown in the top panel, with the terrace profile, shaded light gray, and the trough profile, shaded dark gray, in the bottom panel.

The results for the model simulations for cases 2, 3, and 4 are shown in Figures 43, 44, and 45. Similar to case 1, the model clearly underpredicts the wave height (panel (a)) compared to the instrument (black star) for both profiles. The magnitudes of the longshore currents (panel (b)) in the trough are underpredicted by the model when compared to the video currents. The peak in the cross-shore variation of the currents simulated by the model is also located farther offshore than observed in the video currents. The RMS differences between the video and model currents are listed in Table 11, and show that, in every case, the model currents for trough profile are in better agreement than currents for the terrace profile. Also in every case, the agreement is worse for the trough area compared to the entire surfzone. However, the difference in MWL (panel (c)) between the terrace and trough profiles (panel (d)) creates a longshore pressure gradient in the trough vicinity, which acts as an additional force to drive currents. Therefore, the inclusion of a longshore pressure gradient forcing term in the model will cause the longshore currents to increase in the trough area such that the modeled currents will more closely match the video estimated currents.

Table 11: The RMS difference between video and model currents for the terrace and trough profiles over the entire surfzone and for the trough only for all cases.

RMS_v (m/s)	Full Surfzone			Trough Only		
	N	Terrace Profile	Trough Profile	N	Terrace Profile	Trough Profile
Case 1	36	0.74	0.64	20	0.97	0.85
Case 2	26	0.76	0.71	17	0.93	0.88
Case 3	30	0.55	0.44	20	0.66	0.53
Case 4	30	0.58	0.45	20	0.66	0.53

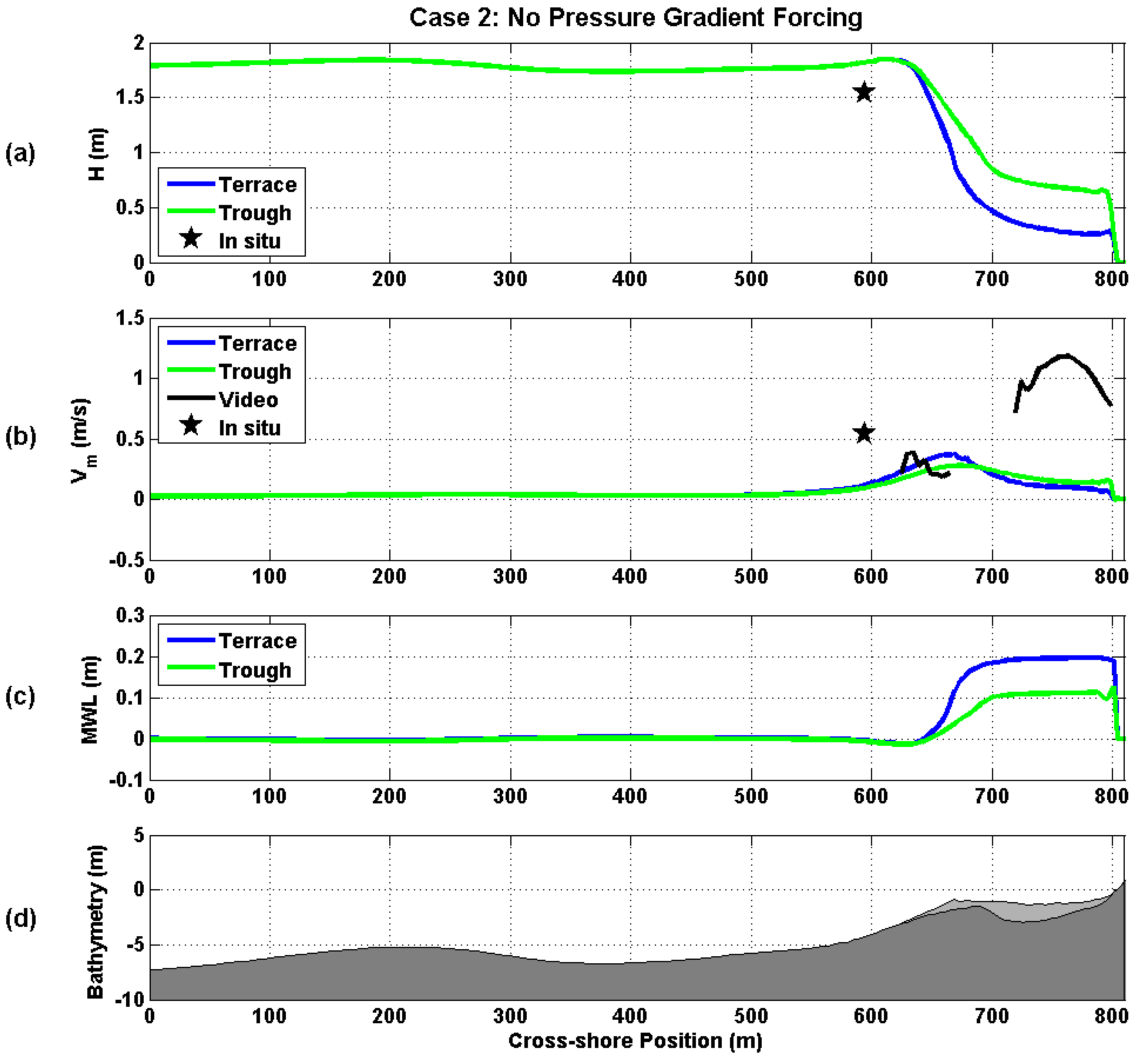

Figure 43: Cross-shore variation of (a) H, (b) V_m, (c) MWL, and (d) h_o for the terrace (light gray) and trough (dark gray) profiles for case 2.

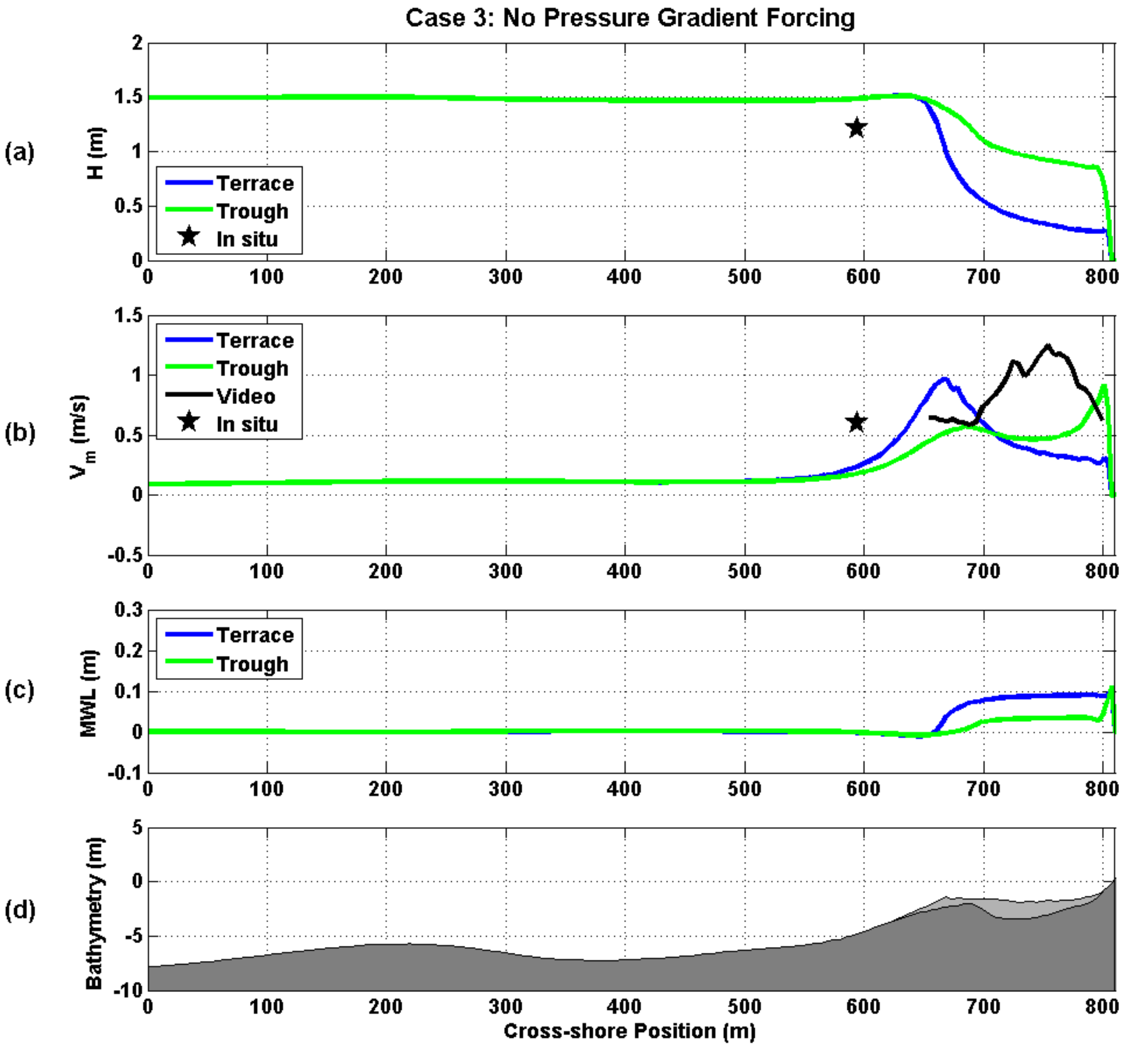

Figure 44: Cross-shore variation of (a) H, (b) V_m, (c) MWL, and (d) h_o for the terrace (light gray) and trough (dark gray) profiles for case 3.

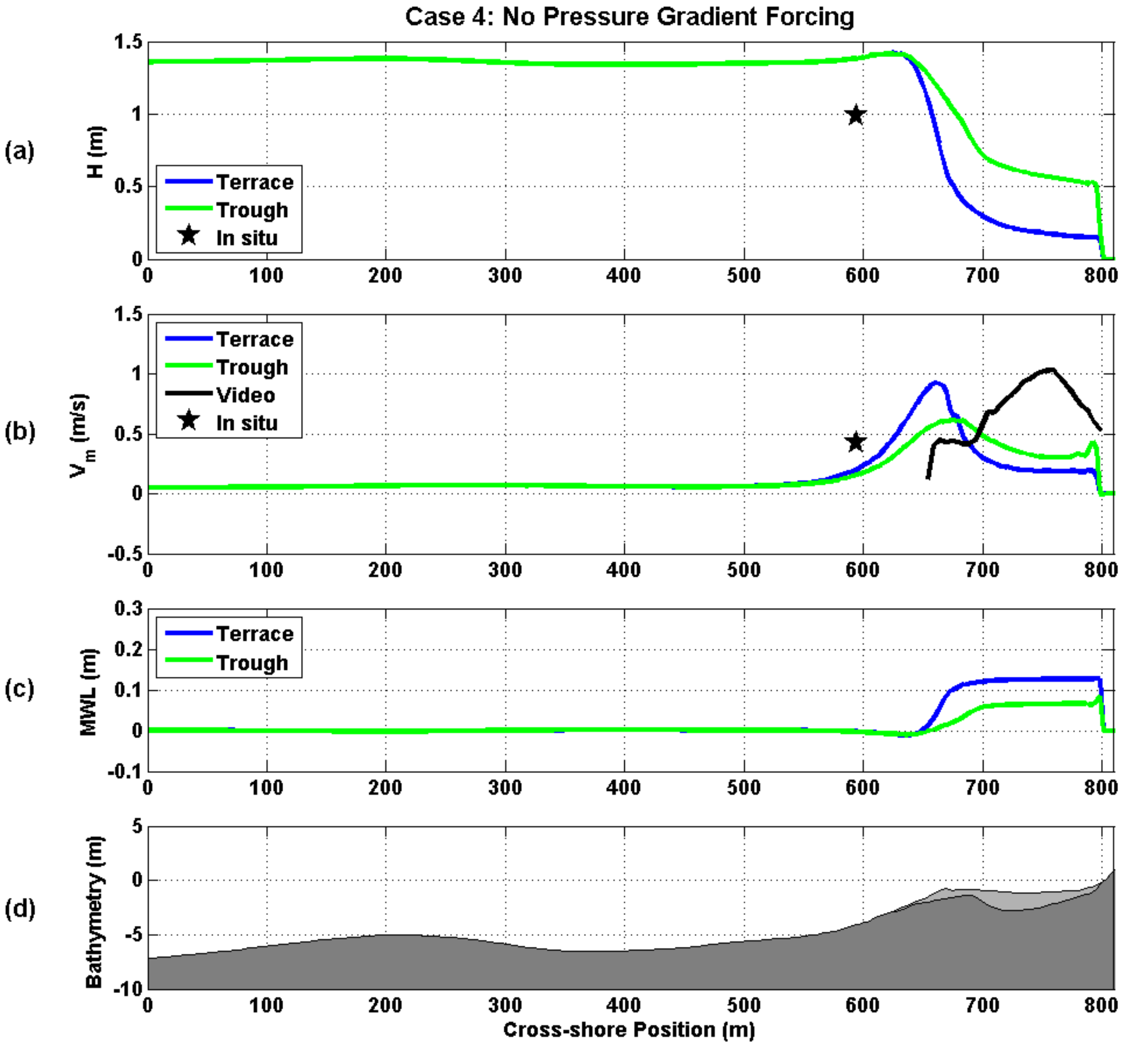

Figure 45: Cross-shore variation of (a) H, (b) V_m, (c) MWL, and (d) h_o for the terrace (light gray) and trough (dark gray) profiles for case 4.

4.2.1 Pressure Gradient Driven Longshore Currents

To account for the longshore pressure gradient forcing in the 1D model, the difference in the MWL between the terrace and trough profiles, $\Delta\zeta$, is determined and then divided by the distance between the profiles, L_p, such that

$$\left(\frac{\partial\bar{\zeta}}{\partial y}\right)_c = \zeta_c' = \frac{\Delta\zeta}{L_p} \tag{52}$$

where the prime indicates a first order derivative with respect to y and subscript 'c' indicates a constantly applied pressure gradient forcing. This yields a forcing term that is large where the MWL difference is large, increasing currents in the trough where they are being underpredicted. It is incorporated in the longshore momentum equation by superimposing the longshore pressure gradient forcing term, $-gh\zeta_c'$.

The results from the model simulation with the constant pressure gradient forcing applied for case 1 are shown in Figure 46. The longshore current (panel (a)) is increased significantly (compared to Figure 39 (b)) in the trough region where the MWL difference (panel (b)) is largest. Even though the modeled currents are much larger in magnitude, the location of peak model currents is similar to the peak video currents. For every case, the RMS differences between the video and model currents are listed in Table 12 and show that the agreement decreased significantly compared to the simulations that did not include pressure gradient forcing (Table 11). Also in every case, the agreement is better for the entire surfzone compared to the trough area. The model results for cases 2, 3, and 4 are shown in Figures 47, 48, 49, indicating the same trend as case 1 of much stronger longshore currents in the trough driven by the large MWL difference.

Table 12: The RMS differences between video and model currents over the entire surfzone and for the trough area only for all cases including longshore pressure gradient forcing.

RMS_v (m/s)	Full Surfzone	Trough Only
Case 1	1.53	1.68
Case 2	1.59	1.85
Case 3	1.49	1.58
Case 4	1.53	1.52

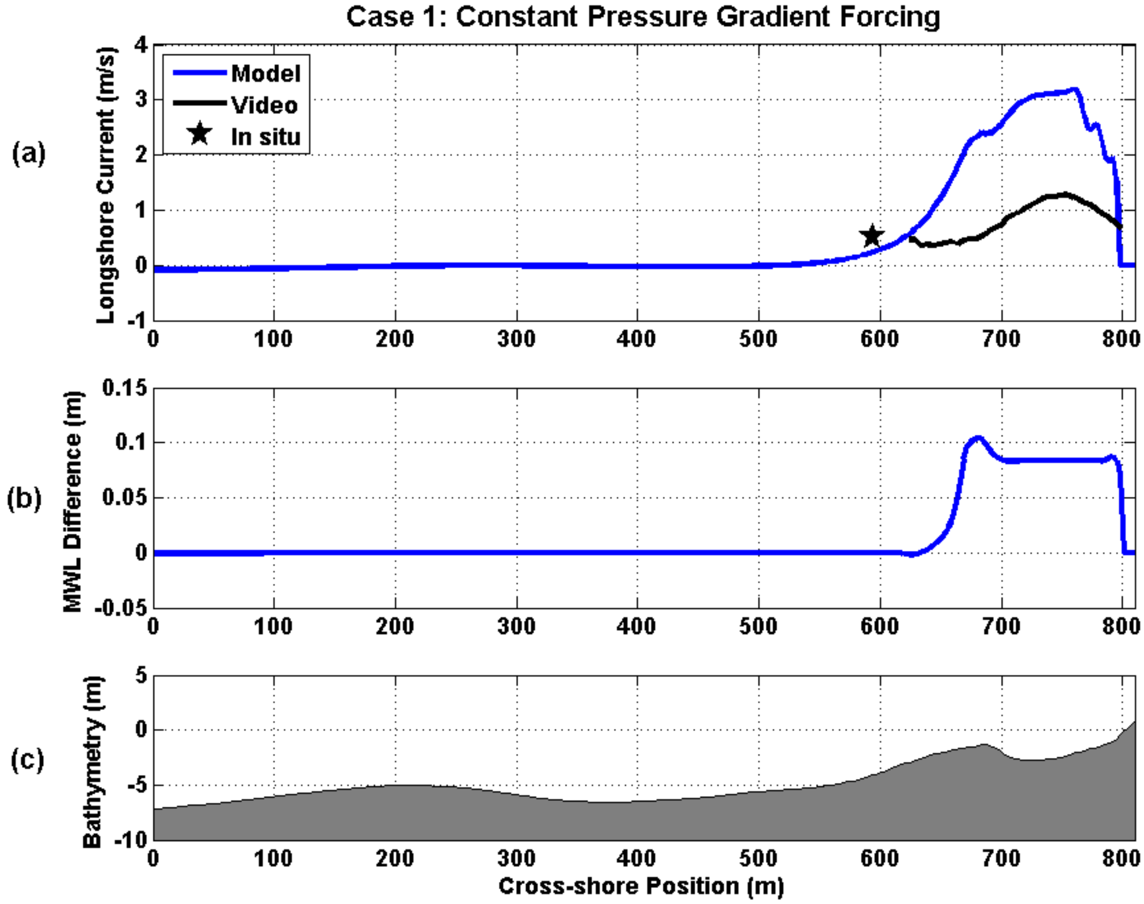

Figure 46: Cross-shore variation of (a) V_m for case 1 with the constant pressure gradient forcing applied, (b) MWL difference between the terrace and trough profiles and (c) h_o for the trough profile.

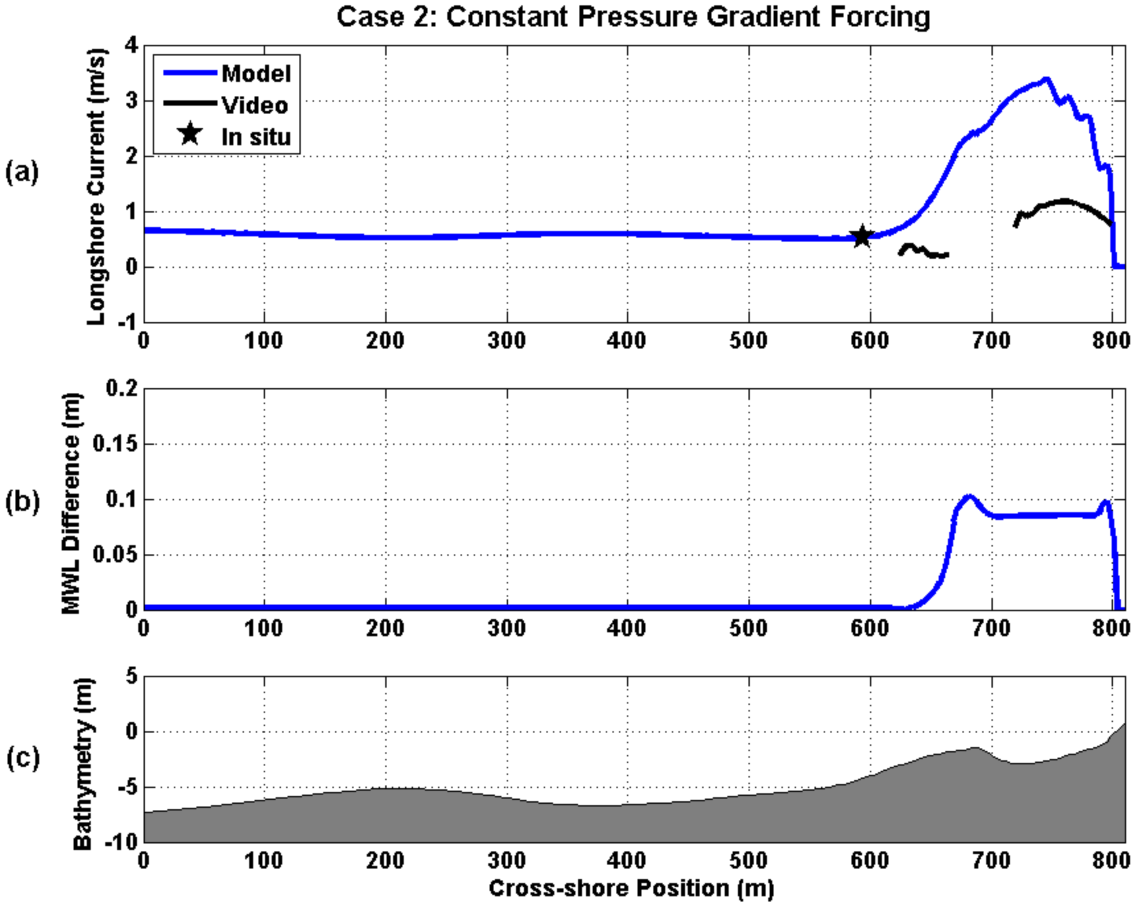

Figure 47: Cross-shore variation of (a) V_m for case 2 with the constant pressure gradient forcing applied, (b) MWL difference between the terrace and trough profiles and (c) h_o for the trough profile.

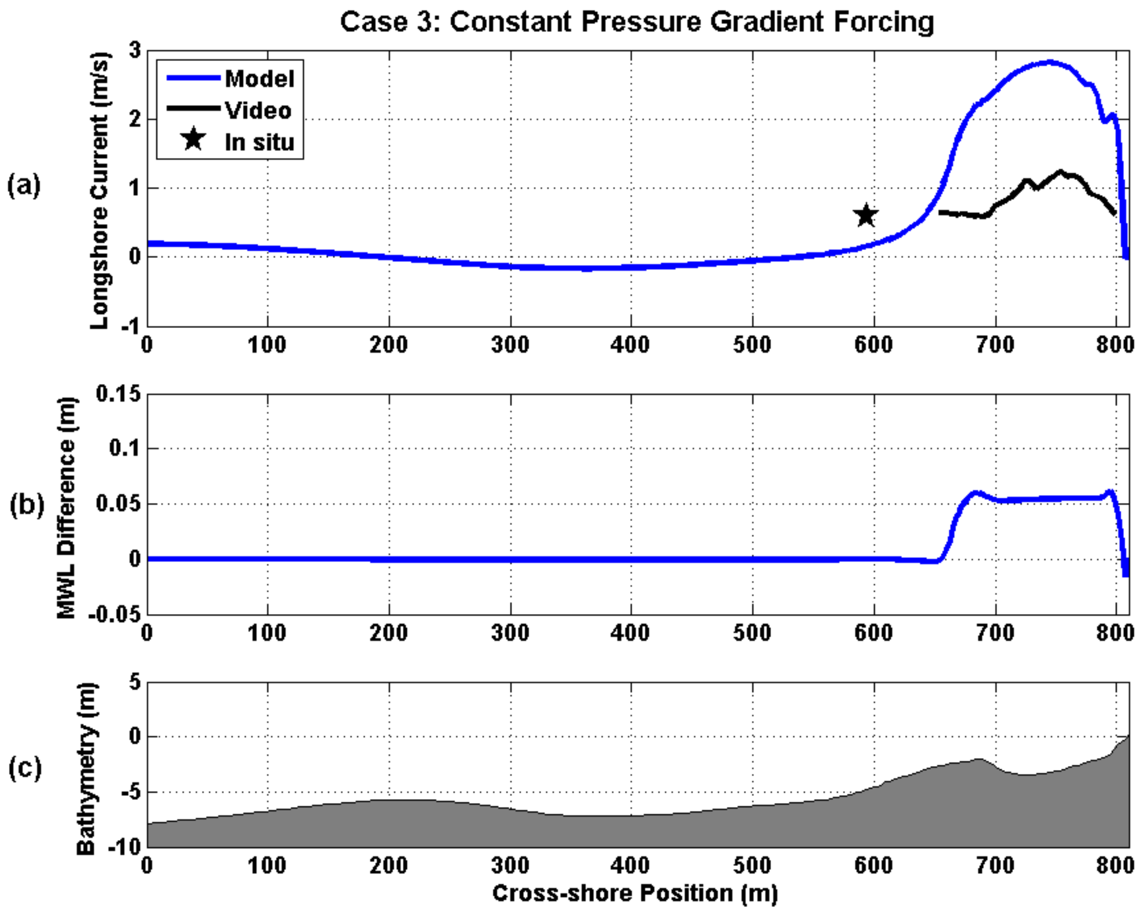

Figure 48: Cross-shore variation of (a) V_m for case 3 with the constant pressure gradient forcing applied, (b) MWL difference between the terrace and trough profiles and (c) h_o for the trough profile.

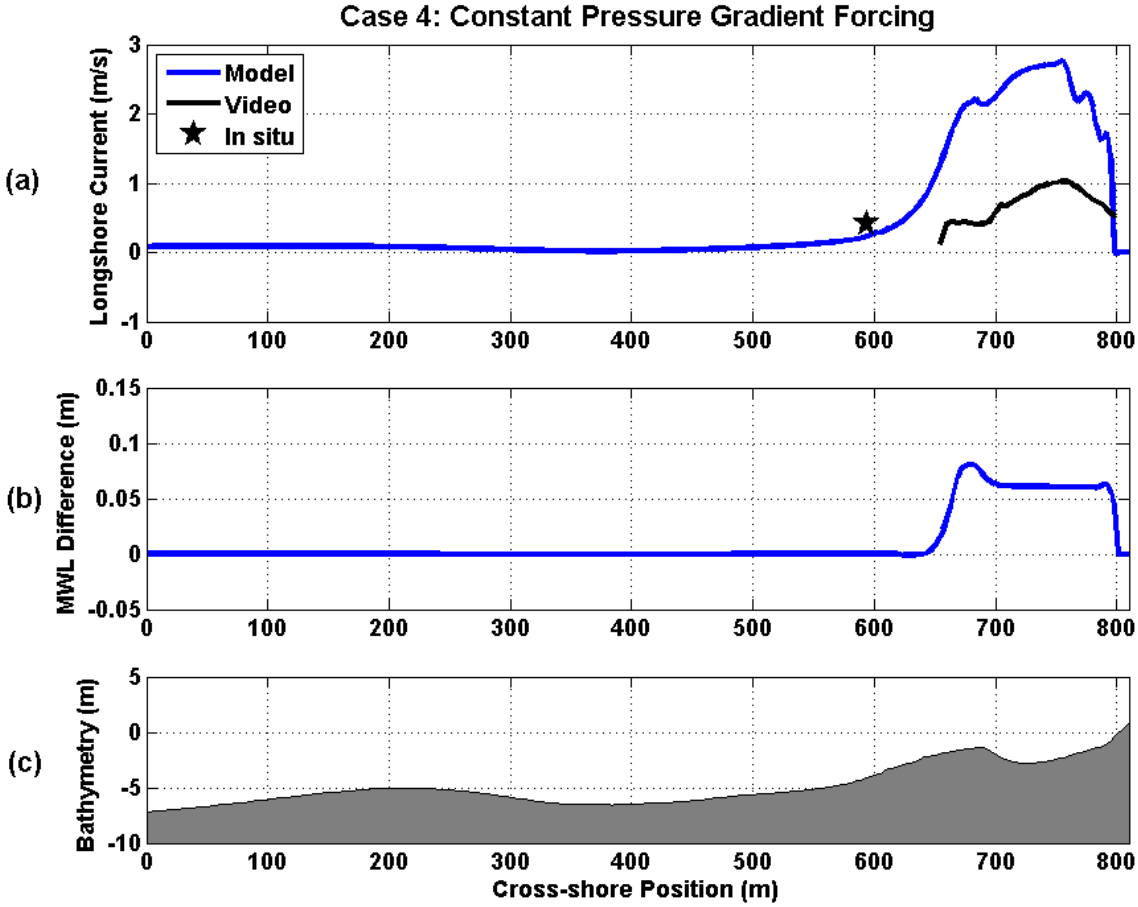

Figure 49: Cross-shore variation of (a) V_m for case 4 with the constant pressure gradient forcing applied, (b) MWL difference between the terrace and trough profiles and (c) h_o for the trough profile.

The dominant terms for the longshore momentum balance, shown in the top panel of Figure 50, include the constant pressure gradient forcing, $-gh\zeta_c'$, and the radiation stress forcing, $\frac{-1}{\rho}\frac{\partial S_{xy}}{\partial x}$, which is balanced by the bottom friction term, $-\frac{\bar{\tau}_y^B}{\rho}$. The pressure gradient is obviously the largest term, contributing the most forcing to longshore current generation and causing the significant overprediction of the currents. Because the model is only 1D, the longshore acceleration $\left(\partial \bar{Q}_y^2/\partial y\right)$ of the flow is neglected. The MWL difference and hence, the pressure gradient, is applied over a relatively short distance so the flow most likely has not reached equilibrium between the forcing and bottom stress.

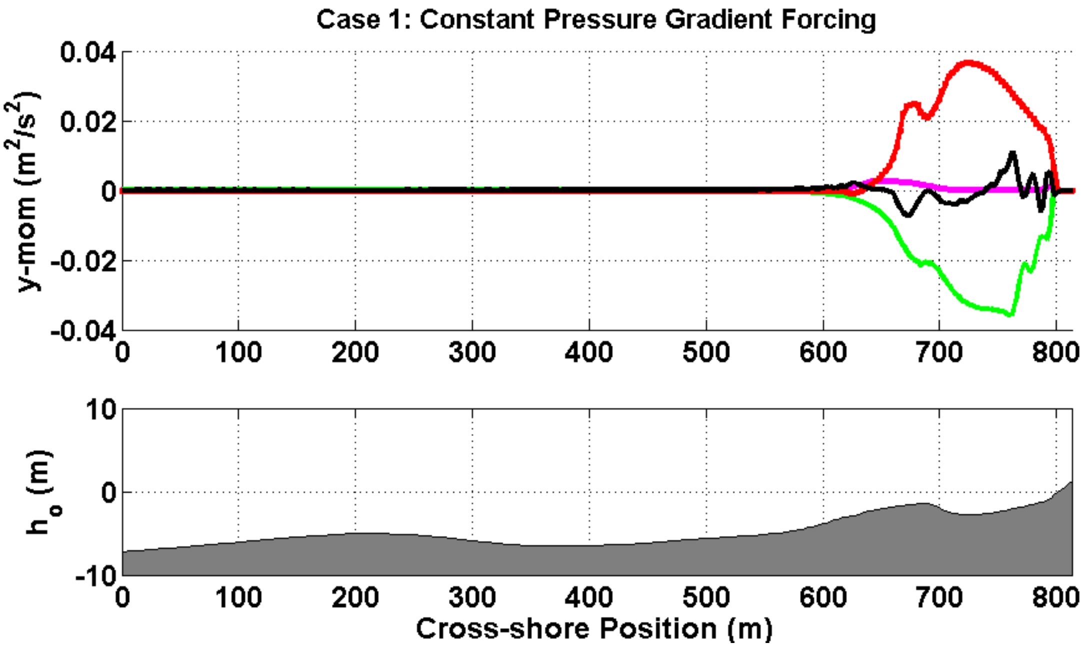

Figure 50: The top panel shows dominant terms in the longshore momentum balance including $\frac{-1}{\rho}\frac{\partial S_{xy}}{\partial x}$ (magenta), $-\frac{\bar{\tau}_y^B}{\rho}$ (green), $-gh\zeta_c'$ (red) and 3D dispersion (black) for case 1 with constant longshore pressure gradient forcing. Bathymetry for the trough profile is shown in the bottom panel.

4.3 Analysis of Longshore Accelerations

As seen in the previous section, the inclusion of the full pressure gradient forcing term allows the model to more accurately predict the location of the longshore currents compared to the video; however, it significantly overpredicts the magnitude of the currents, most likely because it does not account for accelerations of the flow. The dominant momentum balance for strictly pressure gradient driven flow is given by

$$\frac{\partial}{\partial y}\left(\frac{\overline{Q_y}^2}{h}\right)+\frac{\bar{\tau}_y^B}{\rho}=-gh\zeta_c' \qquad (53)$$

and is illustrated in Figure 51. This shows that the acceleration, $\frac{\partial}{\partial y}\left(\frac{\overline{Q_y}^2}{h}\right)$, and the shear stress terms balance the pressure gradient. When the pressure gradient is applied, the accelerations immediately become large and balance the pressure gradient. The bottom shear stress grows as the velocity increases and the accelerations decrease over a distance. At equilibrium, the acceleration term is zero, and the bottom shear stress balances the pressure gradient. Since the distance between the terrace and trough profiles is relatively short (~65m), the flow most likely has not yet reached an equilibrium state.

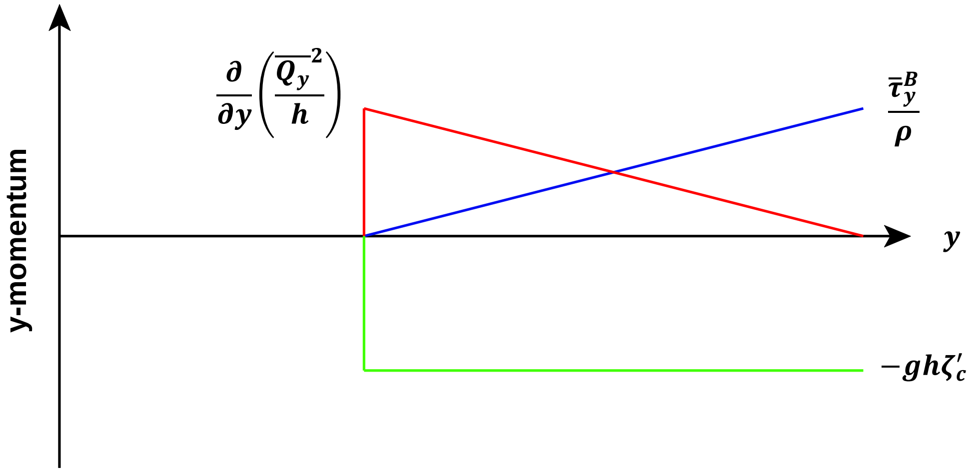

Figure 51: Schematic of the longshore momentum balance for a pressure gradient driven flow with the acceleration, $\frac{\partial}{\partial y}\left(\frac{\overline{Q_y}^2}{h}\right)$ (red) the bottom shear stress, $\frac{\overline{\tau}_y^B}{\rho}$ (blue), and the pressure gradient, $-gh\zeta_c'$ (green).

To better quantify the effect of the pressure gradient on the flow accelerations, an analytical solution for a simplified condition is derived. Assuming depth uniform currents, steady state, no surface stress, small turbulent effects, flat bottom and linearized pressure gradient, Equation (45) reduces to

$$\frac{\partial \overline{Q_x}}{\partial x} + \frac{\partial \overline{Q_y}}{\partial y} = 0 \quad (54)$$

and Equation (46) becomes

$$\frac{1}{h_o}\frac{\partial}{\partial x}\left(\overline{Q_x}\ \overline{Q_y}\right)+\frac{1}{h_o}\frac{\partial}{\partial y}\left(\overline{Q_y}^2\right)=-gh_o\frac{\partial\bar{\zeta}}{\partial y}-\frac{1}{\rho}\frac{\partial S_{xy}}{\partial x}-\frac{\bar{\tau}_y^B}{\rho}. \tag{55}$$

Solving for $\overline{Q_x}$ in Equation (54) gives

$$\overline{Q_x}=-\int\frac{\partial\overline{Q_y}}{\partial y}dx\,. \tag{56}$$

Substituting Equation (56) into Equation (55), assuming $\overline{Q_y}$ is not a function of x and rearranging gives

$$\frac{\partial}{\partial y}\left(\overline{Q_y}^2\right)=-2gh_o^2\frac{\partial\bar{\zeta}}{\partial y}-\frac{2h_o}{\rho}\frac{\partial S_{xy}}{\partial x}-\frac{2h_o}{\rho}\bar{\tau}_y^B \tag{57}$$

where

$$\bar{\tau}_y^B=\frac{1}{2}\rho f_w\frac{\overline{Q_y}^2}{h_o^2}\,. \tag{58}$$

The pressure gradient term is also divided into an amplitude, $\left|\overline{\zeta_c'}\right|$ given by Equation (52), and a longshore varying component, $\zeta_p'(y)$ which governs the shape of ζ', such that

$$\frac{\partial\bar{\zeta}}{\partial y}=\zeta'=\left|\overline{\zeta_c'}\right|\zeta_p'(y). \tag{59}$$

Defining $\lambda=\overline{Q_y}^2$, $a=f_w/h_o$, $b=2gh_o^2\left|\overline{\zeta_c'}\right|$ and $F_w=-\frac{2h_o}{\rho}\frac{\partial S_{xy}}{\partial x}$, the nonlinear partial differential equation becomes the solvable linear first-order differential equation

$$\lambda'+a\lambda=-b\zeta_p'+F_w \tag{60}$$

where a, b, and F_w are known constants which are not functions of y.

Two different shapes for the longshore pressure gradient are used. First, the water level is assumed to vary linearly resulting in a constant pressure gradient as given by Equation (52). Because the water level is decreasing, this results in

$$\zeta_{p,c}'=-1\,. \tag{61}$$

This is shown in Figure 52 by the blue solid line, with the corresponding longshore water level variation shown as the green solid line. To eliminate discontinuities in the forcing, a second profile assumes a cosine water level variation and the resulting sine curve variation for the water level gradient, represented as

$$\left(\frac{\partial \bar{\zeta}}{\partial y}\right)_s = \zeta_s' = -\frac{\pi\left|\bar{\zeta}_c'\right|}{2}\sin(k_s y) \tag{62}$$

where the subscript ‘s’ indicates the sine profile and $k_s = \pi / L_p$. Therefore, it turns out that

$$\zeta_{p,s}' = -\frac{\pi}{2}\sin(k_s y)\,. \tag{63}$$

The sine pressure gradient is shown as the blue dash line in Figure 52 with the corresponding water level profile shown as the green dash line.

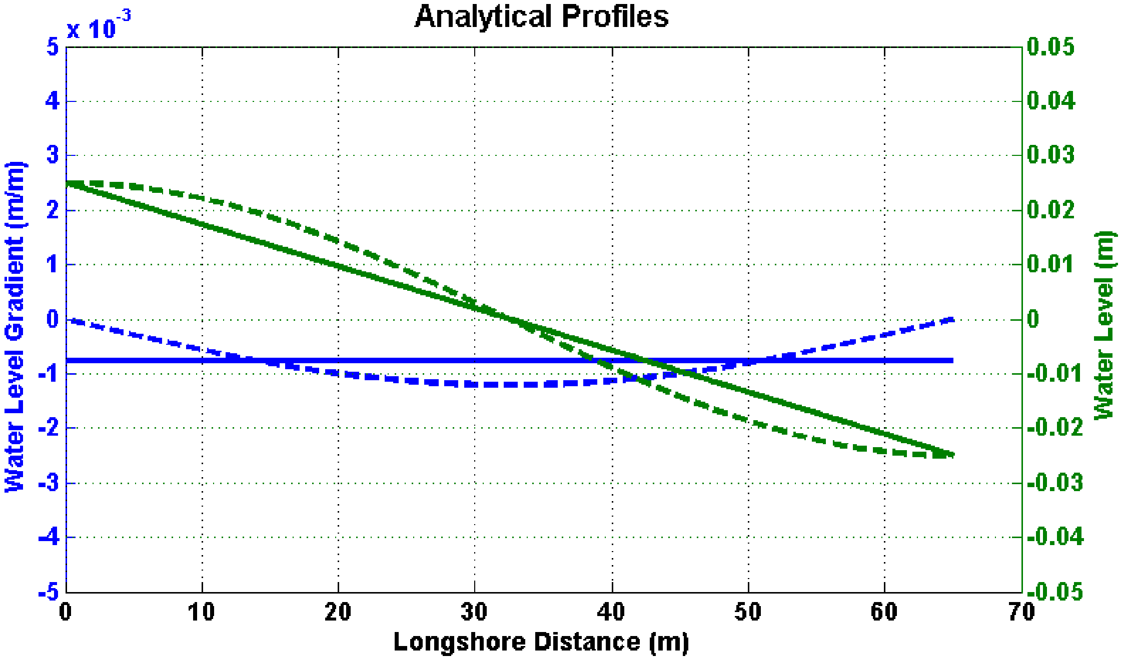

Figure 52: Water level gradient (blue) and water level (green) profiles for the constant pressure gradient profile (solid) and the sine pressure gradient profile (dash).

Finally, for the upstream ($y = 0$) boundary condition, the flux is specified as Q_{yo} assuming that the upstream flow has no pressure gradient forcing and is at equilibrium between the bottom stress and the forcing, F_w. From Equations (57) and (58), this results in

$$Q_{yo}^2 = \frac{F_w}{a}. \tag{64}$$

4.3.1 Analytical Solutions for the Constant Pressure Gradient Profile

The governing equation is solved first for the constant pressure gradient profile. Substituting Equation (61) into Equation (60) yields

$$\lambda' + a\lambda = b + F_w \tag{65}$$

Taking the Laplace transform from the y to the m domain gives

$$m\Lambda - \lambda(0) + a\Lambda = \frac{b}{m} + \frac{F_w}{m} \tag{66}$$

where Λ is the Laplace transform of λ. Applying the boundary condition $\lambda(0) = \bar{Q}_{yo}^2$, where $\bar{Q}_{yo}$ is the incoming flux, and solving for Λ gives

$$\Lambda(m) = \frac{b}{m(m+a)} + \frac{F_w}{m(m+a)} + \frac{\bar{Q}_{yo}^2}{(m+a)}. \tag{67}$$

The Laplace inverse of Equation (67) is taken and the boundary condition that the incoming flux has reached equilibrium is applied such that $F_w = a\bar{Q}_{yo}^2$. The solution for $\bar{Q}_{y,c}^2$ is found as

$$\lambda(y) = \bar{Q}_{y,c}^2 = \frac{b}{a}(1 - e^{-ay}) + \bar{Q}_{yo}^2 \tag{68}$$

and the velocity, V, is defined as

$$V^2 = \frac{\bar{Q}_y^2}{h_o^2}. \tag{69}$$

The equilibrium solution, $\bar{Q}_{eq,c}^2$, can be obtained from Equation (65) by neglecting the acceleration term, λ', and solving for λ

$$\bar{Q}_{eq,c}^2 = \frac{b + F_w}{a} = \frac{b}{a} + \bar{Q}_{yo}^2 \,. \tag{70}$$

By taking the limit of Equation (68) as y approaches infinity, the longshore varying solution is seen to converge to the equilibrium solution

$$\lim_{y \to \infty} \frac{b}{a}\left(1 - e^{-ay}\right) + \bar{Q}_{yo}^2 = \frac{b}{a} + \bar{Q}_{yo}^2 \,. \tag{71}$$

To determine the importance of accelerations for the domain being considered, it is estimated that $h_o = 2m$, $\Delta\zeta = 0.05m$, $L_p = 65m$, $f_w = 0.007$, and $\bar{Q}_{yo}^2 = 1m^2/s^2$. Using these parameter values, Figure 53 (a) shows that V_c is much less than $V_{eq,c}$, indicating that the flow is accelerating and has not reached an equilibrium state. The longshore momentum terms, which are given in Figure 53 (b), show the acceleration and bottom stress terms balance the pressure gradient and radiation stress forcing and an equilibrium state has not yet been reached since the acceleration does not reach zero. When the distance between profiles becomes large ($L_p = 1600m$) and equilibrium is reached, as shown in Figure 53 (c), V_c converges to $V_{eq,c}$. Figure 53 (d) shows that the acceleration becomes negligible such that the pressure gradient and radiation stress forcing is balanced completely by the bottom stress.

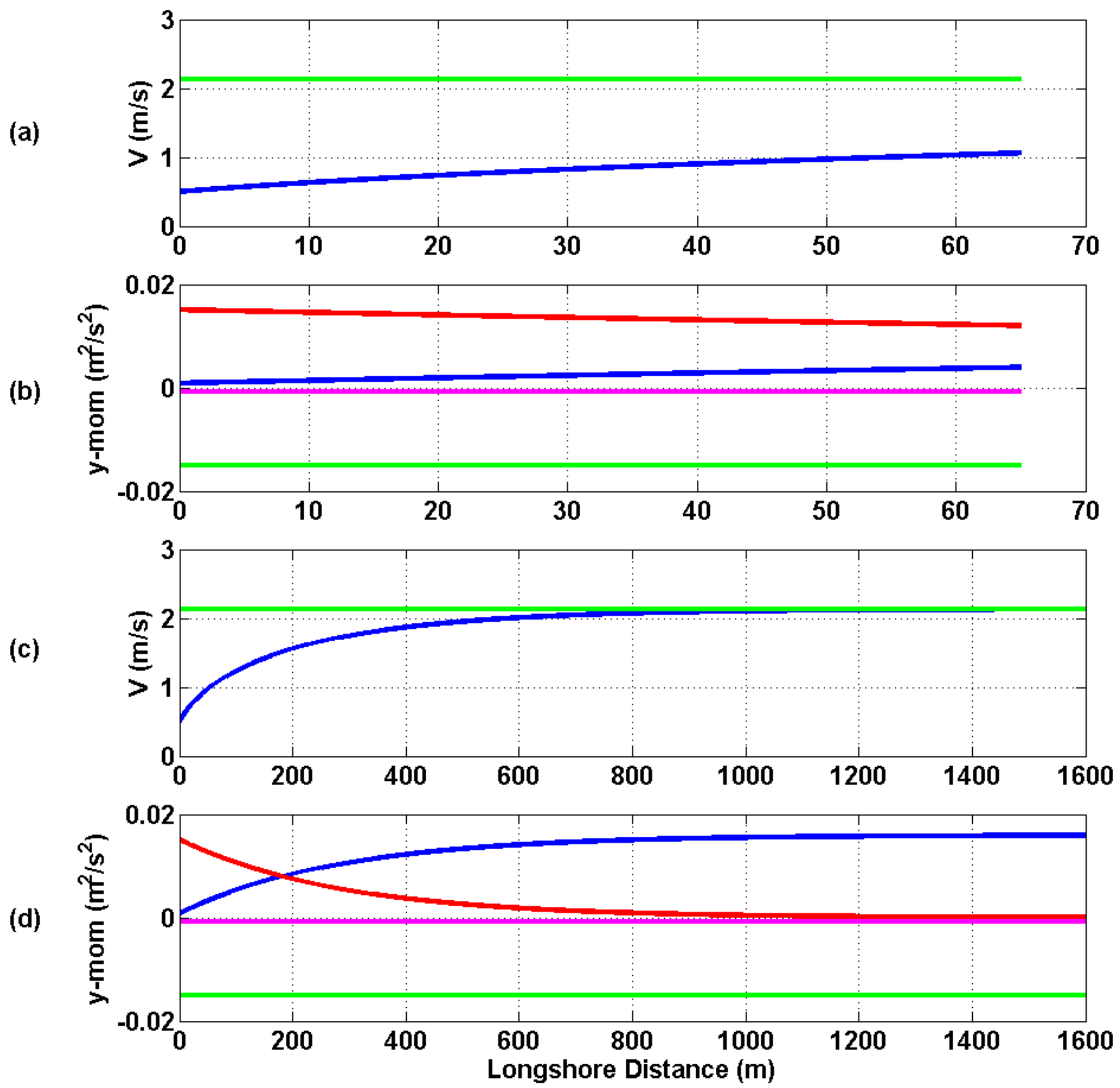

Figure 53: Longshore variation of, (a) V_c (blue), and $V_{eq,c}$ (green) (b) longshore momentum $\frac{1}{\rho}\frac{\partial S_{xy}}{\partial x}$ (magenta), $-gh\zeta_c'$ (green), $\frac{\bar{\tau}_{y,c}^B}{\rho}$ (blue) and $\frac{1}{2}\frac{\partial}{\partial y}\left(\frac{\overline{Q_{y,c}}^2}{h}\right)$ (red). Longshore variation over a longer distance of (c) V_c (blue), $V_{eq,c}$ (green) and (d) longshore momentum terms $\frac{1}{\rho}\frac{\partial S_{xy}}{\partial x}$ (magenta), $-gh\zeta_c'$ (green), $\frac{\bar{\tau}_{y,c}^B}{\rho}$ (blue), and $\frac{1}{2}\frac{\partial}{\partial y}\left(\frac{\overline{Q_{y,c}}^2}{h}\right)$ (red).

To gain a better understanding of the relationship between the general solution and the equilibrium solution and to determine the distance at which equilibrium is reached, $\bar{Q}_{y,c}^2$ is normalized by $\bar{Q}_{eq,c}^2$ to give

$$\frac{\bar{Q}_{y,c}^2}{\bar{Q}_{eq,c}^2} = \frac{\frac{b}{a}(1 - e^{-ay}) + \bar{Q}_{yo}^2}{\frac{b}{a} + \bar{Q}_{yo}^2} = 1 - \frac{e^{-ay}}{1 + \frac{a}{b}\bar{Q}_{yo}^2} \tag{72}$$

where $\bar{Q}_{y,c}^2/\bar{Q}_{eq,c}^2$ ranges from 0 to 1. As the flow reaches equilibrium, this ratio approaches unity. Solving for e^{-ay} in Equation (72) gives

$$e^{-ay} = \left(1 - \frac{\bar{Q}_{y,c}^2}{\bar{Q}_{eq,c}^2}\right)\left(1 + \frac{a}{b}\bar{Q}_{yo}^2\right). \tag{73}$$

The normalized distance is then found to be

$$\frac{y}{h_o} = -\frac{1}{f_w}\ln\left[\left(1 - \frac{\bar{Q}_{y,c}^2}{\bar{Q}_{eq,c}^2}\right)\left(1 + \frac{a}{b}\bar{Q}_{yo}^2\right)\right] \tag{74}$$

which has dependence on f_w, h_o, $\bar{Q}_{yo}^2$, and $\left|\bar{\zeta}_c'\right|$, since $b = 2gh_o^2\left|\bar{\zeta}_c'\right|$.

The dependence of y/h_o on f_w is determined by specifying $\bar{Q}_{y,c}^2/\bar{Q}_{eq,c}^2 = 0.95$ such that the flow has reached 95% of its equilibrium state. For the case with $\bar{Q}_{yo}^2 = 0$, Equation (74) reduces to

$$\frac{y_{95}}{h_o} = -\frac{\ln(0.05)}{f_w} \tag{75}$$

where y_{95} is the distance at 95% equilibrium. Figure 54 shows that the distance to reach 95% of the equilibrium state decreases as the friction factor increases from 0.007 to 0.02, which is also clearly shown by the inverse relation of y_{95}/h_o to f_w in Equation (75). From this equation it is also observed that y_{95} is linearly dependent on h_o. For $h_o = 2\,m$, the distance the flow must travel to reach 95% equilibrium is 856 m for $f_w = 0.007$ and is 300 m for $f_w = 0.02$. This shows that the flow is affected by accelerations over a longer distance when the friction factor is small compared to a larger friction factor. However, for the distance between the terrace and trough profiles ($L_p = 65\,m$), the accelerations are important even assuming $f_w = 0.02$, which is the largest friction factor within the range determined. It is important to note that when the incoming flux is neglected, y_{95}/h_o is a function of f_w only, therefore the magnitude of the pressure gradient has no effect on the distance it takes for 95% equilibrium to be reached. However, the normalized distance is a function of the pressure gradient when the incoming flux term is included, but the dependence is weak, only reducing the equilibrium distance 6.7% for an extreme but realistic mean water level difference.

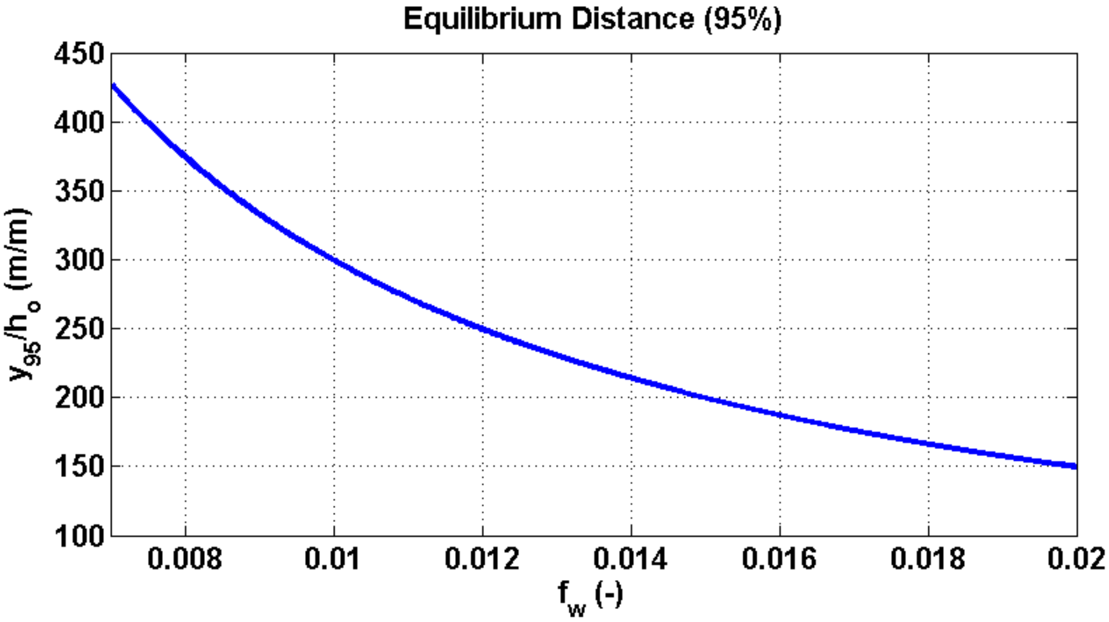

Figure 54: Dependence of the normalized distance, y_{95}/h_o, on f_w at 95% equilibrium.

4.3.2 Modified Pressure Gradient

Although the observed longshore current could be accelerating, the video estimated currents provide an average longshore current without resolving flow variabilities. Therefore, the RMS velocities, V_{rms}, of the analytical results are more representative of currents observed by the video. The RMS flux ($\bar{Q}_{rms}$) is found by integrating over the domain which gives

$$\bar{Q}_{rms,c}^2 = \frac{1}{L_p}\int_0^{L_p} \bar{Q}_{y,c}^2 dy = \frac{b}{aL_p}\left(L_p + \frac{1}{a}e^{-aL_p} - \frac{1}{a}\right) + \bar{Q}_{yo}^2 \,. \tag{76}$$

To include the acceleration effects that the 1D model neglects, the pressure gradient forcing is modified (ζ'_{mod}), reducing the magnitude of the pressure gradient forcing applied in the model, resulting in a quasi two-dimensional (Q2D) model. To accomplish this, an equilibrium momentum balance is assumed using Equations (57) and (58) while neglecting the acceleration such that the longshore momentum balance becomes

$$2gh_o^2\zeta'_{mod} = F_w - \frac{f_w}{h_o}\left(\overline{Q_{rms}{}^2}\right) \tag{77}$$

where ζ'_{mod} accounts for the acceleration effects neglected by the 1D model. Solving for ζ'_{mod} and assuming the incoming flux is driven by the radiation stress forcing, F_w, as shown by Equation (64) gives

$$\zeta'_{mod} = \tfrac{a}{b}\left|\bar{\zeta}'_c\right|\left(\bar{Q}_{yo}^2 - \bar{Q}_{rms}^2\right)\,. \tag{78}$$

Substituting Equation (76) into Equation (78) yields the modified constant pressure gradient

$$\zeta'_{mod,c} = \left|\bar{\zeta}'_c\right|\left(\frac{1}{aL_p} - \frac{1}{aL_p}e^{-aL_p} - 1\right) \tag{79}$$

such that the final longshore momentum balance is between the RMS bottom shear stress (calculated using the RMS flux) and the radiation stress and modified pressure gradient forcing shown in Figure 55.

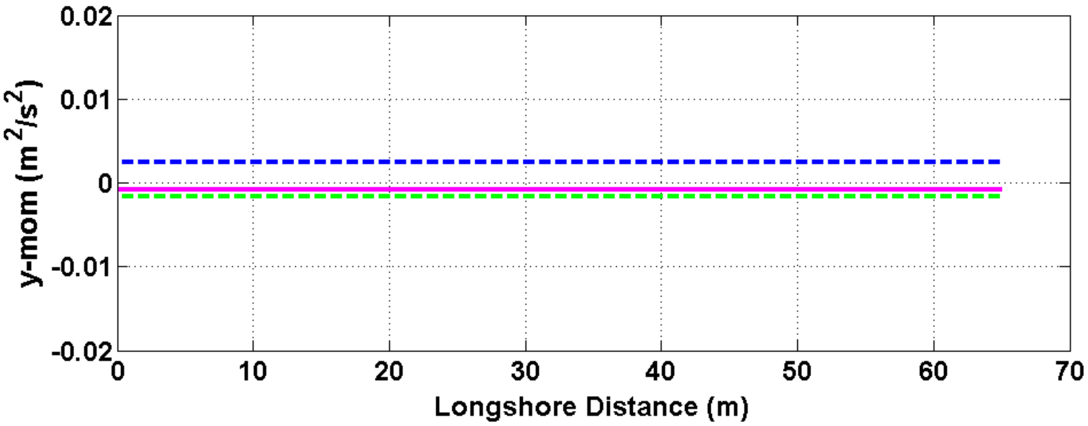

Figure 55: Longshore momentum balance between $\zeta'_{mod,c}$ (green dash), $\frac{1}{\rho}\frac{\partial S_{xy}}{\partial x}$ (magenta solid), and $\frac{\bar{\tau}^{B}_{rms,c}}{\rho}$ (blue dash).

To illustrate how the modified pressure gradient behaves, the effects of varying parameters on $\zeta'_{mod,c}$ are evaluated. From Equation (79), it is seen that $\zeta'_{mod,c}$ varies with $|\overline{\zeta'_c}|$, which is a function of $\Delta\zeta$ and L_p, as well as a, which is equal to f_w/h_o. Normalizing the modified pressure gradient with the constant pressure gradient (Equation (52)) gives

$$\frac{\zeta'_{mod,c}}{\zeta'_c} = \frac{|\overline{\zeta'_c}|\left(\frac{1}{aL_p} - \frac{1}{aL_p}e^{-aL_p} - 1\right)}{-|\overline{\zeta'_c}|} = 1 + \frac{e^{-aL_p}}{aL_p} - \frac{1}{aL_p} \tag{80}$$

eliminating the dependence on $\Delta\zeta$. This ratio is plotted with respect to aL_p, which is varied from 0 to 10, in Figure 56. As aL_p increases, $\zeta'_{mod,c}/\zeta'_c$ approaches unity, meaning that $\zeta'_{mod,c}$ is converging to ζ'_c because acceleration effects are becoming less important. Because $aL_p = f_w L_p/h_o$, an increase in f_w or L_p or a decrease in h_o causes an increase in aL_p. For small aL_p, the ratio is linearly dependent on aL_p, which can be seen in Figure 56 for the beginning part of the curve.

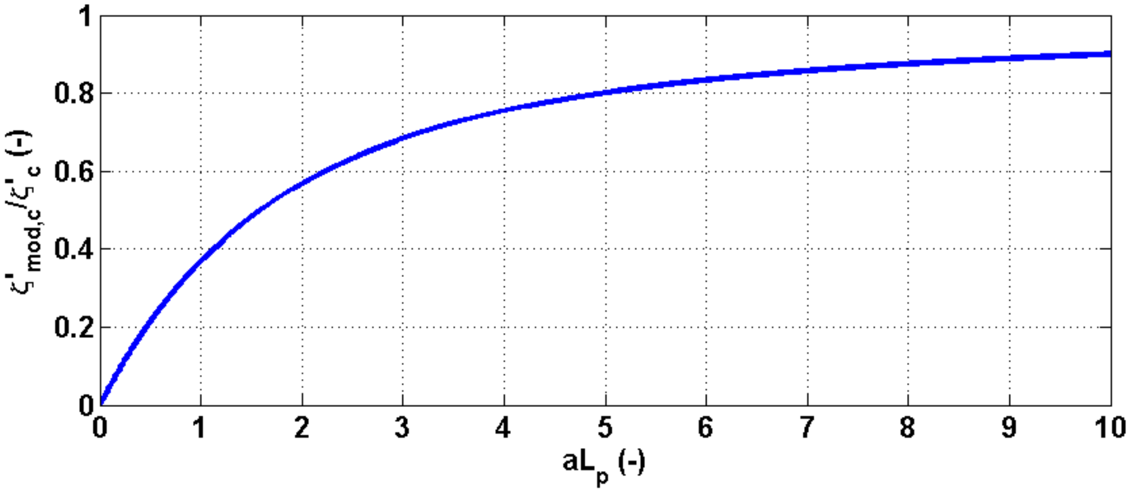

Figure 56: The dependence of $\zeta'_{mod,c}/\zeta'_c$ on aL_p as it is increased from 0 to 10.

To gain a physical understanding of the effects of friction factor, longshore distance, and water depth on all the processes involved with finding the modified pressure gradient, a simplification using Taylor Series Expansion (TS) about $aL_p = 0$ is performed for the case with $\bar{Q}_{yo}^2 = 0$. The assumption that aL_p is small is reasonable given that for $f_w = 0.007$, $h_o = 2m$, and $L_p = 65m$, aL_p turns out to be 0.22. Keeping the first three terms of the expansion for $\bar{Q}_{rms,c}^2$ gives

$$TS\left[\bar{Q}_{rms,c}^2\right] \approx \frac{b}{aL_p}\left(L_p + \frac{1}{a}\left(1 - aL_p + \frac{\left(aL_p\right)^2}{2}\right) - \frac{1}{a}\right) = \frac{bL_p}{2} = gh_o^2|\Delta\zeta| \tag{81}$$

which is independent of f_w and L_p but is a function of h_o^2. Using $TS\left[\bar{Q}_{rms,c}^2\right]$ to calculate the bottom stress, given by Equation (58), yields

$$TS\left[\bar{\tau}_{rms,c}^B\right] \approx \frac{1}{2}\rho\frac{f_w}{h_o^2}\left(gh_o^2|\Delta\zeta|\right) = \frac{1}{2}\rho g f_w \Delta\zeta\ . \tag{82}$$

Equation (82) shows that $TS\left[\bar{\tau}_{rms,c}^B\right]$ is not dependent on h_o or L_p, but it increases as f_w increases. Lastly, a TS is performed on the modified pressure gradient Equation (79) to give

$$TS\left[\zeta'_{mod,c}\right] \approx \zeta'_c\left[1+\frac{1}{aL_p}\left(1-aL_p+\frac{\left(aL_p\right)^2}{2}\right)-\frac{1}{aL_p}\right]=\frac{\Delta\zeta}{L_p}\frac{aL_p}{2}=\frac{\Delta\zeta}{2}\frac{f_w}{h_o}. \tag{83}$$

$TS\left[\zeta'_{mod,c}\right]$ is not dependent on L_p but remains a function of f_w and h_o for small aL_p.

The effects on each of these parameters as f_w, h_o or L_p are increased is listed in Table 13. As f_w increases, there is no effect on ζ'_c. For small values of aL_p, the primary momentum balance is between the pressure gradient and the accelerations; therefore, $TS\left[\bar{Q}^2_{rms,c}\right]$ is independent of friction factor. Since there is no change in the RMS flux, $TS\left[\bar{\tau}^B_{rms,c}\right]$ is increased directly due to f_w and $TS\left[\zeta'_{mod,c}\right]$ is increased since the pressure gradient is modified to balance the larger RMS shear stress.

As h_o increases, ζ'_c is not affected because it is independent of depth. However, $TS\left[\bar{Q}^2_{rms,c}\right]$ increases since a larger pressure force results from deeper water for a fixed slope of ζ'_c. Although the RMS flux increases, this is balanced by the increase in water depth such that the velocity, and thus the $TS\left[\bar{\tau}^B_{rms,c}\right]$, is unchanged. Therefore, $TS\left[\zeta'_{mod,c}\right]$ decreases because less of a slope in the water level is needed when the pressure force is increased.

Lastly, as L_p increases, there is no effect on any of the terms except a decrease in ζ'_c, which is exactly compensated by the longer distance the force is applied, such that the work done by the flow stays constant. Work is equal to the force times the distance over which the force is applied and can be related to ζ'_c, or the force, such that $\Delta\zeta$ is the change in energy, or work, and L_p is the distance. This can be represented as

$$\Delta\zeta = \zeta'_c L_p \tag{84}$$

so that it is clear to see that as L_p increases, ζ'_c must decrease by an exactly proportionate amount such that $\Delta\zeta$ remains unchanged.

Table 13: Effect of increasing the values of f_w, L_p or h_o on ζ_c', $TS[\bar{Q}^2_{rms,c}]$, $TS[\bar{\tau}^B_{rms,c}]$, and $TS[\zeta'_{mod,c}]$.

	$\boldsymbol{f_w}$	$\boldsymbol{h_o}$	$\boldsymbol{L_p}$
$\boldsymbol{\zeta_c'}$	no effect	no effect	decreases
$\boldsymbol{TS[\bar{Q}^2_{rms,c}]}$	no effect	increases	no effect
$\boldsymbol{TS[\bar{\tau}^B_{rms,c}]}$	increases	no effect	no effect
$\boldsymbol{TS[\zeta'_{mod,c}]}$	increases	decreases	no effect

4.3.3 Analytical Solutions for the Sine Pressure Gradient Profile

Now, the governing equation is solved for the second case with the sine pressure gradient profile. Substituting Equation (63) into Equation (60) yields

$$\lambda' + a\lambda = b_s \sin(k_s y) + F_w \tag{85}$$

where $b_s = \frac{\pi}{2} b$. Taking the Laplace transform gives

$$m\Lambda - \lambda(0) + a\Lambda = b_s\left(\frac{k_s}{m^2 + k_s^2}\right) + \frac{F_w}{m}. \tag{86}$$

Applying the boundary condition $\lambda(0) = \bar{Q}^2_{yo}$ and solving for Λ gives

$$\Lambda(m) = b_s\left[\frac{k_s}{(m+a)(m^2+k_s^2)}\right] + \frac{F_w}{m(m+a)} + \frac{\bar{Q}^2_{yo}}{(m+a)}. \tag{87}$$

The Laplace inverse is taken of Equation (87), and again, applying $F_w = a\bar{Q}^2_{yo}$, an equation is found defining $\bar{Q}^2_y$ as

$$\lambda(y) = \bar{Q}^2_{y,s} = b_s A\left[e^{-ay} + \frac{a}{k_s}\sin(k_s y) - \cos(k_s y)\right] + \bar{Q}^2_{yo} \tag{88}$$

where

$$A = \frac{k_s}{k_s^2 + a^2} = \frac{\pi L_p h_o^2}{\pi^2 h_o^2 + f_w^2 L_p^2}. \tag{89}$$

The top panel of Figure 57 shows the velocity, V_s, defined as

$$V_s^2 = \frac{\bar{Q}_{y,s}^2}{h_o^2} \tag{90}$$

which has a more realistic variation in velocity without the discontinuities in the derivatives at the endpoints compared to V_c shown in Figure 53 (a). The bottom panel of Figure 57 shows the acceleration term mostly balances the pressure gradient. However, the bottom stress gradually increases over the distance between profiles, which causes the acceleration term to decrease faster than the pressure gradient forcing. By the end where the pressure gradient approaches zero, the flow actually decelerates slightly to balance the bottom stress.

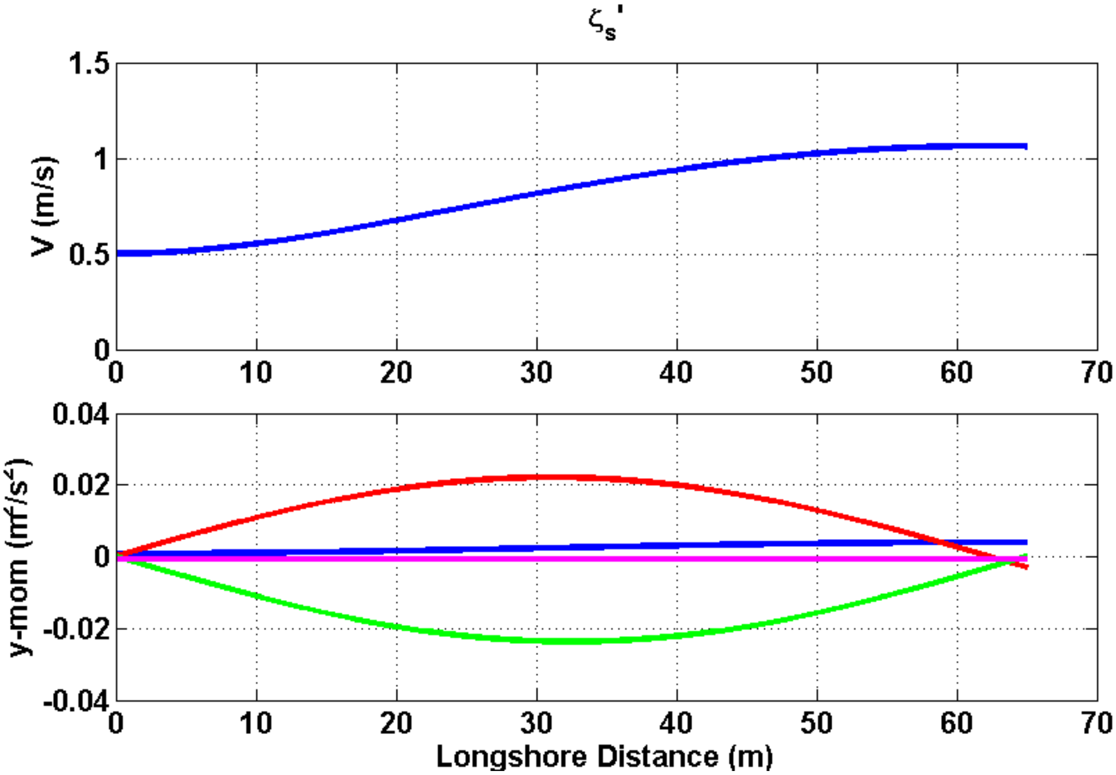

Figure 57: Longshore variation of, (top) V_s (bottom) longshore momentum $\frac{1}{\rho}\frac{\partial S_{xy}}{\partial x}$ (magenta), $-gh\zeta_s'$ (green), $\frac{\bar{\tau}_{y,s}^B}{\rho}$ (blue) and $\frac{1}{2}\frac{\partial}{\partial y}\left(\frac{\overline{Q_{y,s}}^2}{h}\right)$ (red).

Next, the $\bar{Q}^2_{rms,s}$ is found and is given as

$$\bar{Q}^2_{rms,s} = \frac{1}{L_p}\int_0^{L_p} \bar{Q}^2_{y,s}dy = \frac{b_s A}{aL_p}\left(1 - e^{-aL_p} + \frac{2a^2}{k_s^2}\right) + \bar{Q}^2_{yo}\,. \tag{91}$$

The velocities for the constant and sine pressure gradient profiles are calculated using Equation (69) and are shown in Figure 58. There is a negligible difference between $V_{rms,c}$ and $V_{rms,s}$, quantified to be less than 1% due to the similarities in V_c and V_s which are also shown in this figure.

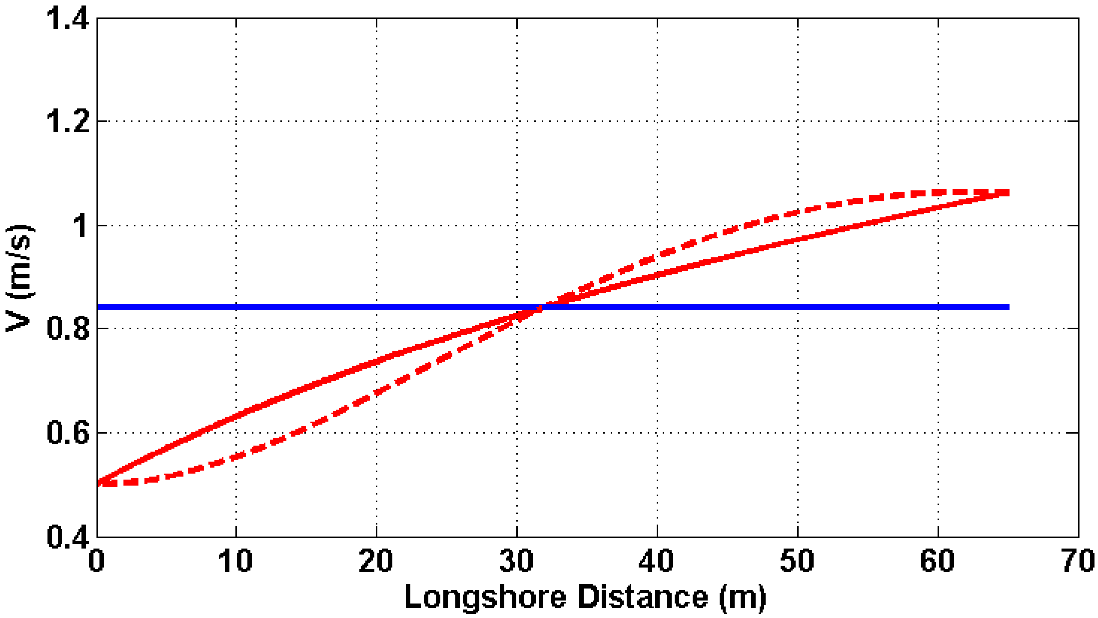

Figure 58: $V_{rms,c}$ (blue solid) and $V_{rms,s}$ (blue dash) corresponding to V_c (red solid) and V_s (red dash).

As the distance between profiles becomes large, the limit of $\bar{Q}^2_{rms,c}$ as L_p goes to infinity is found from Equation (76) to be equal to the equilibrium solution given by Equation (70). Similarly, taking the limit of $\bar{Q}^2_{rms,s}$ gives

$$\lim_{L_p\to\infty}\bar{Q}^2_{rms,s} = \lim_{L_p\to\infty}\frac{b_s}{a}\left(\frac{\pi}{\pi^2+a^2L_p^2}-\frac{\pi}{\pi^2+a^2L_p^2}e^{-aL_p}+\frac{2a^2L_p^2}{\pi\left(\pi^2+a^2L_p^2\right)}\right)+\bar{Q}^2_{yo}. \tag{92}$$

Applying l'Hôpital's rule yields

$$\lim_{L_p\to\infty}\bar{Q}^2_{rms,s}=\frac{b}{a}+\bar{Q}^2_{yo} \tag{93}$$

which is the equilibrium solution and is the same result obtained from taking the limit of the constant pressure gradient case. Therefore, the constant and sine pressure gradient cases approach the same value for V_{rms} as the domain grows.

Substituting Equation (91) into Equation (78) yields the modified sine pressure gradient

$$\zeta'_{mod,s}=\frac{\pi}{2}\frac{A}{L_p}\left|\bar{\zeta}'_c\right|\left(e^{-aL_p}-2\frac{a^2}{k_s^2}-1\right). \tag{94}$$

Comparing the momentum balances for the constant case (Figure 59 (top)) and the sine case (Figure 59 (bottom)), the acceleration and pressure gradient terms are seen to have much different shapes between the cases. However, the modified pressure gradient, which is found by balancing the RMS bottom shear stress, are very similar.

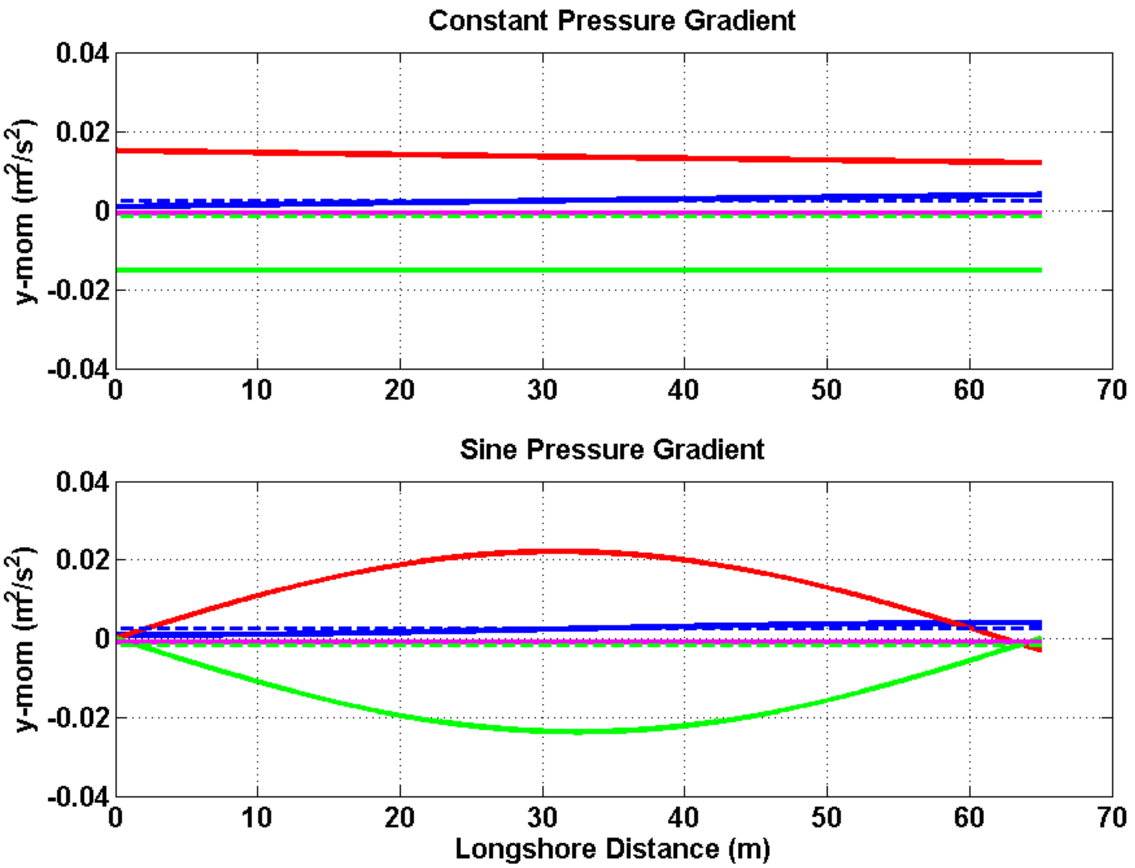

Figure 59: Longshore variation of, (top) longshore momentum for the constant case $\frac{1}{\rho}\frac{\partial S_{xy}}{\partial x}$ (magenta), $-gh\zeta_c'$ (green solid), $\frac{\bar{\tau}^B_{y,c}}{\rho}$ (blue solid) $\frac{1}{2}\frac{\partial}{\partial y}\left(\frac{\overline{Q_{y,c}}^2}{h}\right)$ (red), the modified pressure gradient, $-gh\zeta'_{mod,c}$ (green dash), and the RMS bottom stress $\bar{\tau}^B_{rms,c}$ (blue dash), (bottom) longshore momentum terms for the sine case $\frac{1}{\rho}\frac{\partial S_{xy}}{\partial x}$ (magenta), $-gh\zeta_s'$ (green), $\frac{\bar{\tau}^B_{y,s}}{\rho}$ (blue), $\frac{1}{2}\frac{\partial}{\partial y}\left(\frac{\overline{Q_{y,s}}^2}{h}\right)$ (red), the modified pressure gradient, $-gh\zeta'_{mod,s}$ (green dash), and the RMS bottom stress $\bar{\tau}^B_{rms,s}$ (blue dash).

4.3.4 Quasi Two-dimensional Model

The modified pressure gradient for the sine profile given by Equation (94) is used as the pressure gradient forcing in the Q2D model for cases 1, 2, 3 and 4. Since this equation is derived using a flat bottom assumption, a constant depth of $h_o = 1.8\,m$ is used, which is the average depth in the trough area between the two profiles. The results from these model simulations are shown in Figures 60 – 63. In each case, the modeled currents match the video currents much more closely than without pressure gradient forcing or the pressure gradient forcing excluding acceleration effects. The magnitude and location the peak of the modeled currents with the modified pressure gradient forcing is similar to the peak video currents. The better agreement between the video and model currents in the surfzone and the trough for every case is also reflected in their RMS differences given in Table 14, where the agreement is best when only the trough area is considered.

Although the model simulated currents are similar for each case, there are subtle differences in the cross-shore profiles. Comparing Figures 60 – 63, a small secondary peak in the currents is located at cross-shore location 675 m, which is offshore of the pressure gradient driven flow, implying that it is caused by radiation stress forcing. Although this variation is present in all cases, it is smallest for case 2, which from Table 10 has the smallest wave angle. Therefore, the variation may be caused by a large angle of incidence of incoming waves causing a peak in the primarily radiation stress driven currents offshore of the primarily pressure gradient driven flow in the trough area. Case 3, which has the highest water level of any other case, is the only simulation that a peak in currents is predicted at the shoreline (Figure 62). This indicates that waves are too small to break over the bar because of the high tide level, allowing more wave energy to be dissipated at the shoreline, driving significant longshore currents at that location. Lastly, case 4 has the smallest wave height of any other case, which is clearly reflected by the weaker longshore currents shown in Figure 63.

Table 14: The RMS differences between video and model currents over the entire surfzone and for the trough area only for all cases including longshore pressure gradient forcing.

RMS_v (m/s)	Full Surfzone	Trough Only
Case 1	0.25	0.23
Case 2	0.20	0.19
Case 3	0.18	0.17
Case 4	0.29	0.16

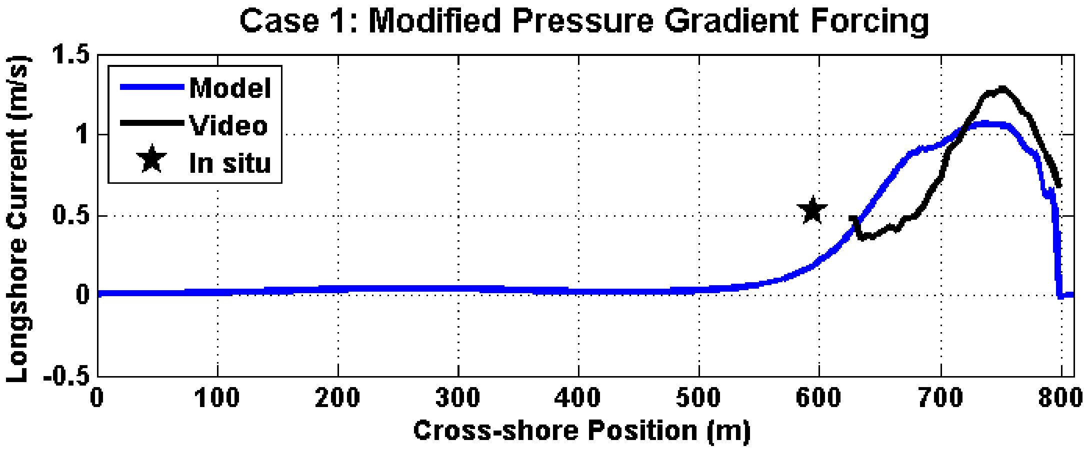

Figure 60: Cross-shore variation of V_m for case 1 with the modified pressure gradient forcing applied.

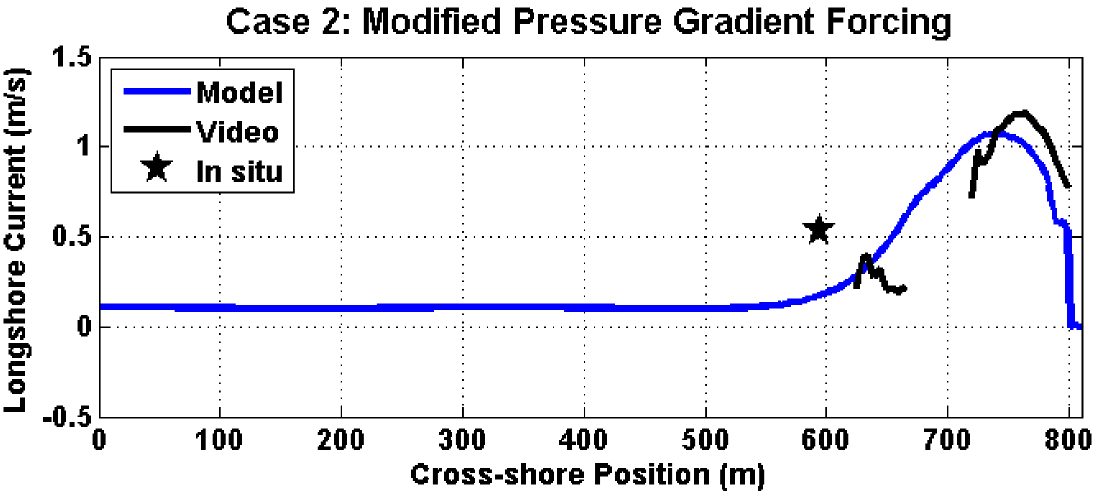

Figure 61: Cross-shore variation of V_m for case 2 with the modified pressure gradient forcing applied.

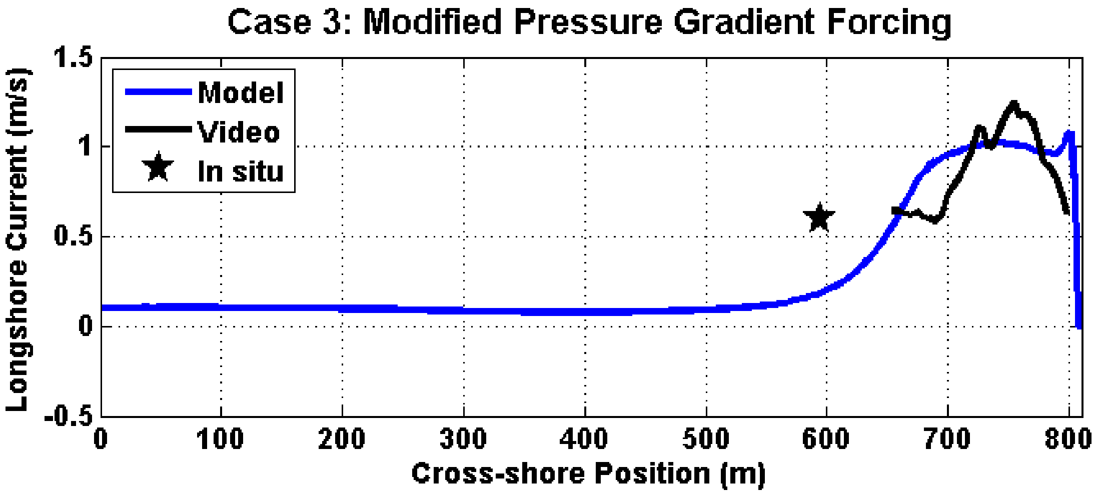

Figure 62: Cross-shore variation of V_m for case 3 with the modified pressure gradient forcing applied.

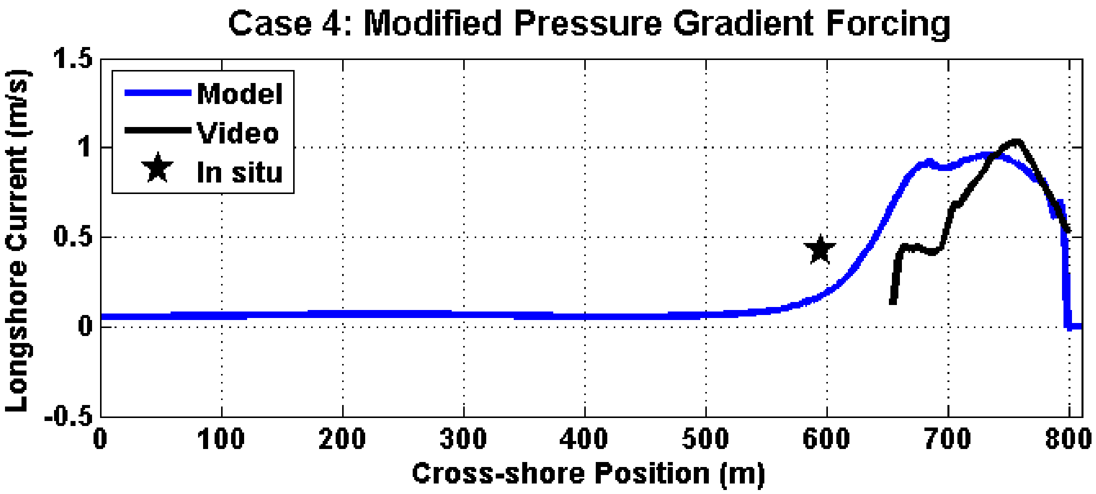

Figure 63: Cross-shore variation of V_m for case 4 with the modified pressure gradient forcing applied.

4.3.5 Model Sensitivity to Gamma

To gain a better understanding of the model results, the wave breaking parameter, γ, is decreased from 0.6 to 0.4 and the effect on currents is analyzed. Figure 64 shows that the reduction in γ causes the currents to decrease in the trough but increase slightly on the offshore bar. The longshore forcing terms, shown in Figure 65, indicate that the radiation stress and pressure gradient forcing for $\gamma = 0.6$ is larger than the radiation stress and pressure gradient forcing for $\gamma = 0.4$ in the trough.

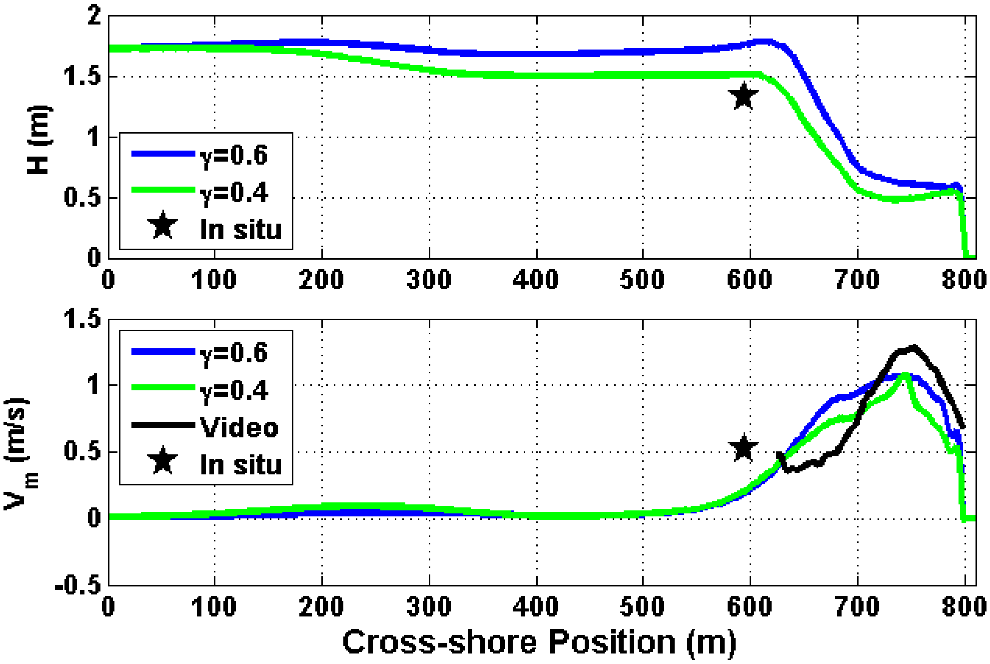

Figure 64: Cross-shore variation of (top) H and (bottom) V$_m$ for $\gamma = 0.6$ (blue) and $\gamma = 0.4$ (green) for case 1.

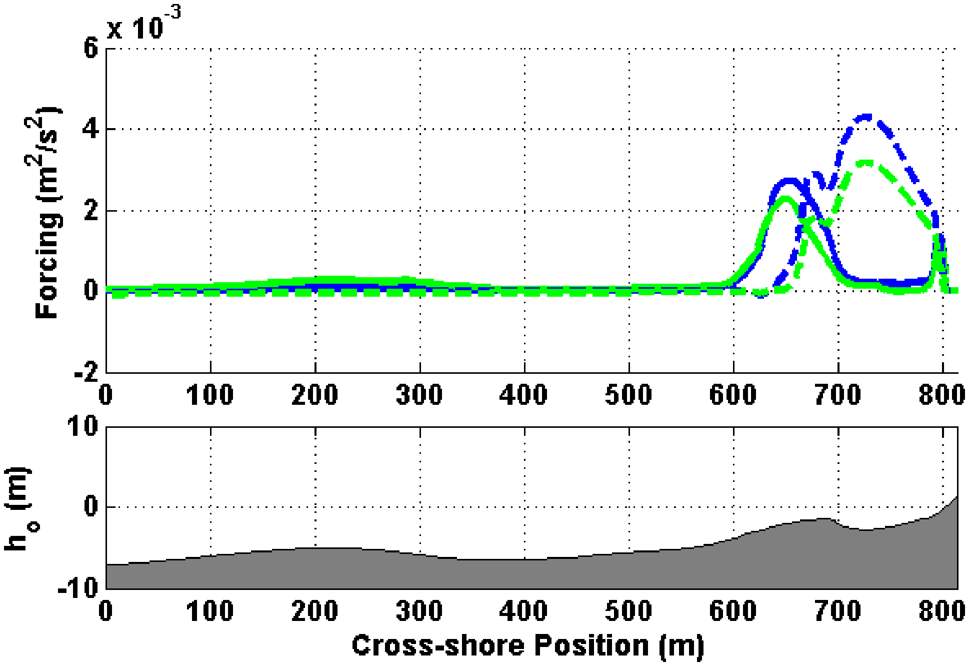

Figure 65: Cross-shore variation (top) radiation stress gradient, $\frac{-1}{\rho}\frac{\partial S_{xy}}{\partial x}$ (solid), and the longshore pressure gradient, $-gh\frac{\partial\bar{\zeta}}{\partial y}$ (dash), for $\gamma = 0.6$ (blue) and $\gamma = 0.4$ (green) for case 1, (bottom) h_o for the trough profile.

The decrease in radiation stress gradient forcing on the inner bar with a decrease in γ (Figure 65) is due to a decrease in wave breaking. This can be quantified by calculating the difference of wave height before breaking (x=609m) and after breaking (x=729m) which is found to be 1.14 m for $\gamma = 0.6$ and 1.02 m for $\gamma = 0.4$. This difference is due to more breaking on the outer bar for $\gamma = 0.4$, which causes less energy to be contributed to breaking at the inner bar, thus a smaller reduction in wave height. The smaller γ is shown to have less dissipation in Figure 66. From Equations (40) and (41), it can be seen that dissipation is a function of γ^{-4} such that a decrease in γ increases dissipation; however, dissipation is also a function of H_{rms}^{7} such that smaller wave height results in less dissipation. Even though smaller γ leads to more dissipation, smaller H_{rms} reduces it more because dissipation is a stronger function of H_{rms} than γ. Therefore, the decrease in radiation stress for a decrease in γ is caused by less wave breaking on the inner bar. Because the cross-shore pressure gradient forcing is decreased due to the decrease in cross-shore radiation stress, the mean water level difference between the terrace and trough profiles is smaller for $\gamma = 0.4$.

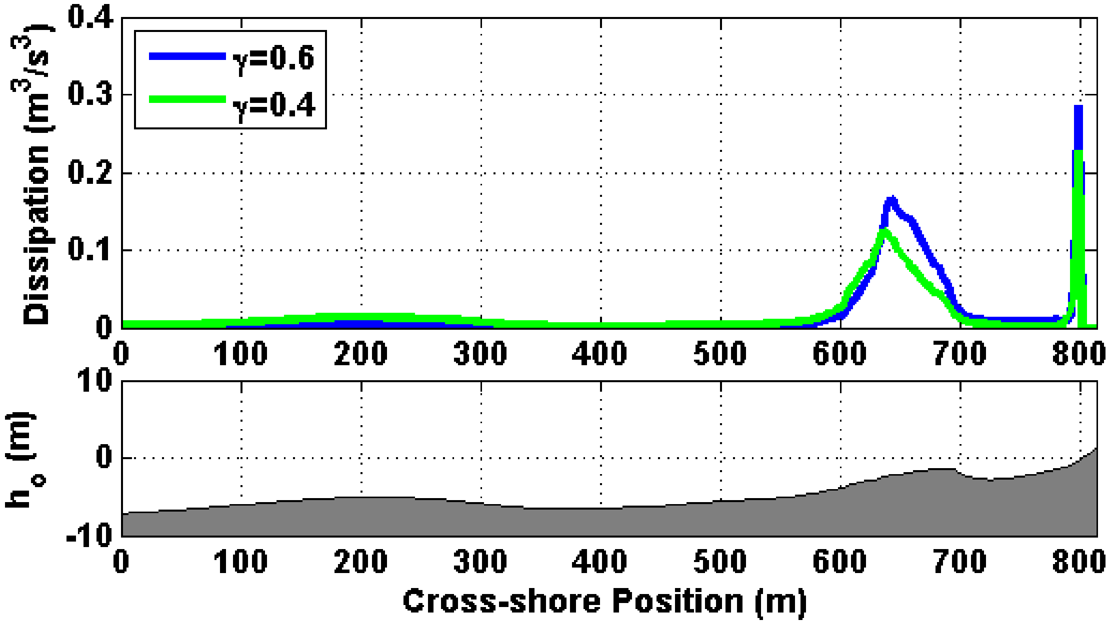

Figure 66: Cross-shore variation (top) dissipation for $\gamma = 0.6$ (blue) and $\gamma = 0.4$ (green) for case 1, (bottom) h_o for the trough profile.

4.3.6 Effects of Friction Factor on Model Currents

Another parameter that affects the modeled longshore currents is the friction factor. As the friction factor is increased, the currents are decreased significantly at the offshore edge of the inner bar (x=600 m) and only slightly in the trough, as shown in Figure 67.

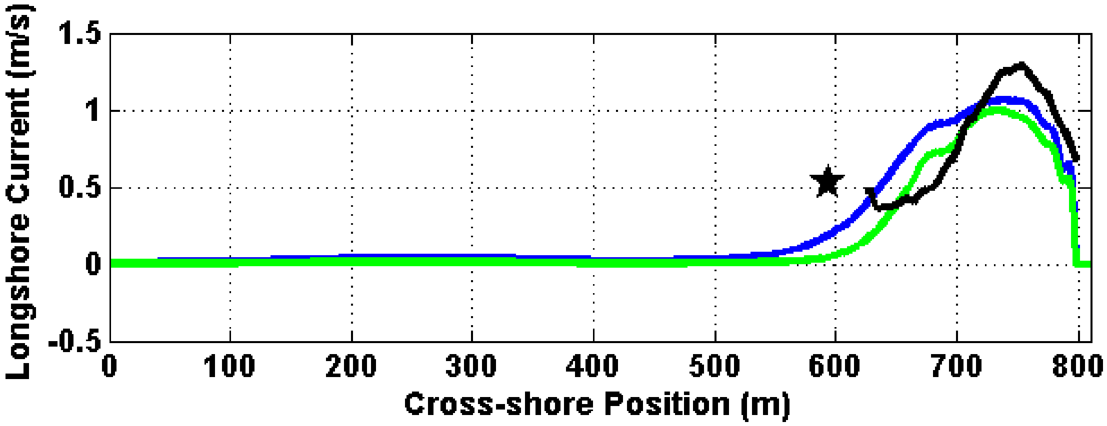

Figure 67: Cross-shore variation of V_m for $f_w = 0.007$ (blue), $f_w = 0.02$ (green), video (black) and instrument (black star) for case 1.

The forcing is shown in Figure 68 and reveals that the radiation stress forcing is unchanged by the increase in friction factor; however, the longshore pressure gradient forcing is increased significantly as friction is increased as demonstrated previously. By combining Equations (58) and (69), the bottom shear stress is defined as

$$\bar{\tau}_y^B = \frac{1}{2}\rho f_w V_c^2 \,. \tag{95}$$

Balancing the shear stress with the total forcing generated by radiation stress and pressure gradients, F_t, and solving for velocity gives

$$V_c^2 = \frac{2F_t}{\rho f_w}. \tag{96}$$

Equation (95) shows that the velocity is a function of the ratio of forcing to friction factor, which is shown in Figure 69. It is clearly seen that, at the offshore edge of the inner bar, F_t/f_w is much larger for $f_w = 0.007$ compared to $f_w = 0.02$. In the trough, however, there is only a small difference in magnitudes of the ratios. Therefore, the bigger difference in the currents between $f_w = 0.007$ and $f_w = 0.02$ at the offshore edge of the inner bar is due to the change in the ratio of total forcing and friction factor, on which the velocity is dependent. Even though the forcing is increased with the larger friction factor, this is more than compensated by the decrease in currents due to the larger f_w.

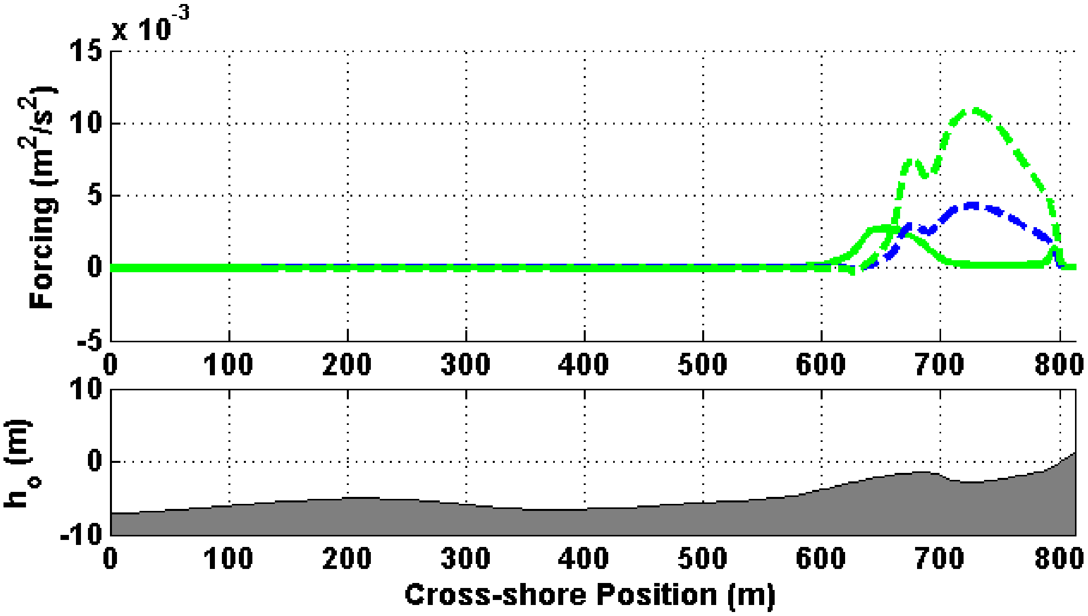

Figure 68: Cross-shore variation (top) radiation stress gradient, $\frac{-1}{\rho}\frac{\partial S_{xy}}{\partial x}$ (solid), and the longshore pressure gradient, $-gh\frac{\partial \bar{\zeta}}{\partial y}$ (dash), for $f_w = 0.007$ (blue) and $f_w = 0.02$ (green) for case 1, (bottom) h_o for the trough profile.

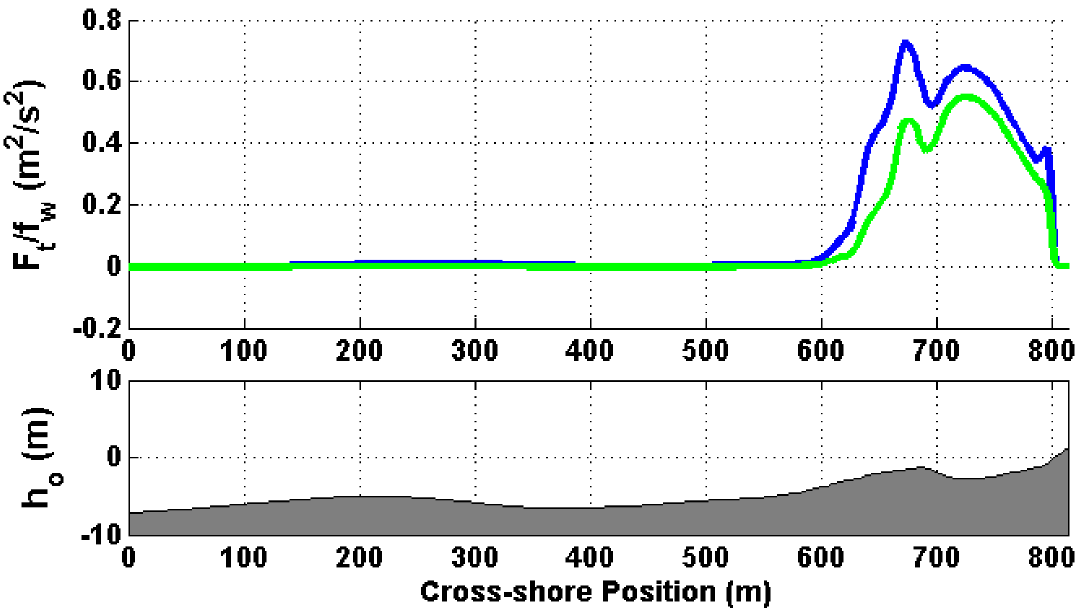

Figure 69: Cross-shore variation (top) ratio of forcing to friction factor, F_t/f_w for $f_w = 0.007$ (blue) and $f_w = 0.02$ (green) for case 1, (bottom) h_o for the trough profile.

4.4 Summary

As part of the NearCoM numerical modeling system, the wave module, REF/DIF-S, and the circulation module, SHORECIRC, are used to simulate nearshore waves and currents for the Nor'easter storm event occurring on February 12 and 13. The model, which is run for a 1D cross-shore profile, uses offshore wind and wave conditions for four cases that are evaluated at the model boundary and two bathymetry profiles, one which intersects a trough and one which intersects a terrace. The first 1D simulation predicts currents that are much weaker and farther offshore than the video estimated currents. However, a mean water level difference, which is located in the trough area between the inner bar and the shoreline at the location of maximum video currents, results from larger wave setup due to preferential breaking on the terrace profile compared to the trough profile.

Although another 1D model simulation that includes the pressure gradient forcing predicts currents with a cross-shore variation similar to the video estimated currents, the magnitude of the model simulated currents are much larger than the currents estimated from video. The longshore momentum balance shows that the pressure gradient term dominates over the radiation stress term and is balanced by the bottom shear stress. Because the relatively large water level difference (~0.1m) is applied over a relatively short distance (~65 m), it is assumed that the flow has not reached an equilibrium state and the convective accelerations are important.

The effects of the accelerations on the flow is determined by solving two analytical cases for a linearly varying water level, corresponding to a constant pressure gradient, and a cosine varying water level, corresponding to a sinusoidal pressure gradient. Using reduced continuity and momentum equations and simplified parameters representative of the storm conditions, it is shown that the flow in the video domain is accelerating and the bottom shear stress has not fully developed to balance the forcing terms.

Because the model used in this study does not resolve 2D accelerations, the effects of the accelerating flow are accounted for by modifying the pressure gradient term in the momentum balance. The acceleration term is neglected and the bottom shear stress is calculated in terms of an RMS longshore velocity, which is representative of the average current that the video provides. The modified pressure gradient is found such that, in addition to the radiation stress term, the forcing terms are balanced by the RMS bottom shear stress. For the regime of small $f_w L_p / h_o$, which is representative of the domain considered in this research, the modified pressure gradient increases with a larger friction factor due to higher bottom stress. As water depth increases, the pressure force increases and less of a slope of the water level is needed, decreasing the modified pressure gradient. The distance between profiles has no effect on the modified pressure gradient because the decrease in the pressure gradient is exactly compensated by the increase in the distance between profiles.

Substituting this modified pressure gradient into the longshore momentum balance as the pressure gradient forcing, the Q2D model simulated currents are similar in magnitude and cross-shore variation to the video estimated currents for all cases. By reducing the breaking wave parameter, the simulated longshore currents are reduced because wave height decreases, which decreases the longshore variability in setup, reducing the longshore pressure gradient that drives the currents. Increasing the friction factor also decreases currents at the outer edge of the inner surfzone because the radiation stress forcing is not a function of friction factor. However, in the inner surfzone where the pressure gradient forcing is dominant, there is less of an effect because the pressure gradient increases with increasing friction factor.

CHAPTER 5

CONCLUSIONS

The complex processes that drive sediment transport are important to understand so that shoreline change can be predicted and mitigated. To develop the understanding of these processes, a coastal erosion study was conducted at Cape Hatteras, NC, which is part of the cuspate forelands of the Southeastern United States. This highly dynamic area was studied using several types of in situ and remote sensing techniques from February 2 – 21, 2010 to assess the sediment transport and processes that maintain the existence of the cape's associated shoal complex, Diamond Shoals.

The present research focuses on radiation stress and pressure gradient driven longshore currents, which are the basic mechanisms that drive longshore sediment transport. Using video images from recordings of a portion of the surf zone on the North side of the cape, longshore currents are estimated with the Optical Current Meter Technique developed by Chickadel et al. (2003). Image statistics are calculated to characterize morphology of the nearshore region and to qualitatively assess the amount of wave breaking that occurs in view of the camera. To determine the effect of wave breaking on currents, the numerical models SHORECIRC and REF/DIF-S are used as part of the NearCoM modeling system to simulate nearshore waves and currents. The model simulated momentum balances are used to evaluate the effects of radiation stress and pressure gradient driven longshore currents, where the predicted currents are compared to currents estimated with video and measured with an in situ instrument.

For a Nor'easter storm occurring on February 12 and 13, the gradients in cross-shore and longshore radiation stress and the surface wind stress are calculated using the hour averaged wind and wave data. These results are compared to the hour averaged longshore velocities estimated with video to determine the effects of the changing wind and wave conditions on the currents. The wave height to water depth ratio affects the currents since a larger ratio indicates more wave breaking which means more wave dissipation and an increase in radiation stress forcing. However, the angle of incidence of incoming waves is shown to affect the longshore currents more significantly than any other wind or wave parameter. A more oblique wave angle causes a greater component of the radiation stress to act in the longshore direction, contributing more forcing to generate longshore currents.

Using the NearCoM modeling system with SHORECIRC and REF/DIF-S, currents driven by pressure gradient and radiation stress forcing are simulated. The magnitude of the current driven by the pressure gradient is directly related to the magnitude of the pressure gradient forcing term, which is dependent on the mean water level difference and the distance over which the pressure gradient acts. For a relatively large mean water level difference that acts over a relatively short distance, which is the case for this study, acceleration effects greatly impact the flow because the flow has not reached an equilibrium state. Prior to reaching an equilibrium state, the pressure gradient forcing term is mostly balanced by the acceleration term while the bottom shear stress gradually increases over the length of the domain. Therefore, neglecting this acceleration term causes a large overestimate of the bottom stress, leading to an over prediction of longshore currents.

Analytical solutions are used to determine the effects of the accelerations on the flow. The pressure gradient forcing is first assumed to be constant over the distance between profiles, such that the water level variation is linear, and a second solution assumes a sine pressure gradient profile, such that the water level variation has a cosine shape. Solving reduced forms of the continuity and longshore momentum equations, the longshore velocity is found as a function of longshore distance. For small distances, the velocity is much less than the equilibrium velocity and the longshore momentum for the flow shows the acceleration term mostly balances the radiation stress and pressure gradient forcing terms, while the bottom stress gradually increases. However, for longer distances the velocity approaches an equilibrium velocity and the bottom stress mostly balances the radiation stress and pressure gradient forcing terms while the acceleration term goes to zero.

An equilibrium distance is derived to determine the distance the flow must travel to reach an equilibrium state, or a state in which acceleration effects are negligible. This term is linearly dependent on water depth and decreases with increasing friction factor. However, the equilibrium distance is found to be only a weak function of the pressure gradient forcing.

To account for the effects of accelerations but maintain the balance that is present in an equilibrium flow state, a RMS value of the bottom shear stress is used to modify the pressure gradient. The modified pressure gradient, which is reduced due to acceleration effects, is superimposed in the longshore momentum equation as the pressure gradient forcing term and, with the radiation stress forcing, balances the bottom shear stress. The longshore current simulations that include the modified pressure gradient forcing are much more realistic compared to the simulations that assume an equilibrium flow state because the modified pressure gradient includes the effects of accelerations. Comparing the Q2D model simulated currents to the video estimated currents show that the flow observed in the video is at least partially driven by longshore pressure gradients because the model and video currents are similar in magnitude and cross-shore variation.

The unique contributions of this research are:

- A new method is developed to calculate the apparent velocity induced from the 2D video interpreting vertical motion in the real-world as horizontal motion;

- Theoretical analysis of a longshore flow that is driven, at least in part, by a relatively large pressure gradient over a relatively short distance to show the importance of flow accelerations;
- Analytical solutions of the equilibrium distance for a flow that is affected by accelerations;
- The effects of accelerations on the flow are included in a quasi two-dimensional model by using a modified pressure gradient to more accurately predict longshore currents.

Additional research that can be done to improve the results of this study are performing the same types of analysis on the full video data set. This includes creating standard deviation images for each day to determine the morphological changes, such as bar migration, of the nearshore region in view of the camera throughout the duration of the experiment. These images can also be used to determine estimates of dissipation or percentage of breaking, which can then be compared to the video estimated currents. By cross-referencing the results with the wind and wave data, additional conclusions may be gained on the effects of the changing conditions on longshore currents, dissipation, and wave breaking.

To evaluate the resulting conclusions from the video, longshore simulations that include time varying tides and forcing will provide more insight on the longshore currents and how they are affected by changing wind and wave parameters. Also, the importance of accelerations on the flow can be determined using a 2D model that directly resolves the longshore flow accelerations. Ideally, all model results, including the Q2D results, could be validated using measurements from a laboratory or field experiment that focuses on pressure gradient driven flow.

REFERENCES

Alexander, P. S. and Holman R. A. (2004). “Quantification of nearshore morphology based on video imaging.” *Marine Geology*, 208, 101-111.

Apotsos, A., Raubenheimer, B., Elgar, S., and Guza, R. T. (2008). “Wave-driven setup and alongshore flows observed onshore of a submarine canyon.” *Journal of Geophysical Research*, 113(C07025).

Battjes, J. A., (1975). “Modeling of turbulence in the surf zone.” *ASCE Proc. Symp. on Modelling Techniques*, San Francisco, 1050-1061.

Benedet, L. and List, J. H. (2008). “Evaluation of the physical processes controlling beach changes adjacent to nearshore dredge pits.” *Coastal Engineering*, 55, 1224-1236.

Bowen, A. J. (1969). “The generation of longshore currents on a plane beach.” *Journal of Marine Research*, 27(2), 206-215.

Cambazoglu, M. K. and Haas, K. A. (2011). “Numerical modeling of breaking waves and cross-shore currents on barred beaches.” *Journal of Waterway, Port, Coastal and Ocean Engineerin*g, 137(6), 310-324.

Chickadel, C. C., Holman, R. A., and Freilich, M. H. (2003). “An optical technique for the measurement of longshore currents.” *Journal of Geophysical Research*, 108(C11), 3364.

Coffey, F. C. and Nielsen, P., (1984). “Aspects of wave current boundary layer flows.” *Proc. 19th International Conference on Coastal Engineering*, ASCE, 2232-2245.

Dalrymple, R. A. (1978). “Rip currents and their causes.” *Proc. Coastal Engineering Conference 16th*, New York, ASCE, 1414-1427.

Gourlay, M. R. (1976). “Non-uniform alongshore currents.” *Proc. Coastal Engineering Conference 15th*, New York, ASCE, 701-720.

Guedes, R. M. C., Calliari, L. J., Holland, K. T., Plant, N. G., Pereira, P. S., and Alves, F. N. A. (2011). “Short-term sandbar variability based on video imagery: comparison between time-average and time-variance techniques.” *Marine Geology*, 289, 122-134.

Haas, K. A. and Cambazoglu, M. K. (2006). “Video observations of longshore currents, Myrtle Beach, South Carolina.” *Proc. 30th International Conference on Coastal Engineering*, San Diego, California, 1079-1086.

Haas, K. A., Svendsen, I. A., Brander, R. W., and Nielsen, P. (2002). “Modeling of a rip current system on Morton Island, Australia.” *Proc. 28th International Conference on Coastal Engineering*, Cardiff, Wales.

Haller, M. C., Dalrymple, R. A., and Svendsen, I. A. (2002). “Experimental study of nearshore dynamics on a barred beach with rip channels.” *Journal of Geophysical Research*, 107(C6,3061).

Holland, K. T., Holman, R. A., Lippmann, T. C., Stanley, J., and Plant, N. (1997). “Practical use of video imagery in nearshore oceanographic field studies.” *IEEE Journal of Oceanic Engineering*, 22(1), 81-92.

Johns, B. (1983). Physical Oceanography of Coastal and Shelf Seas. *Elsevier Science Publishers*, pp. 470.

Jonsson, I. G. (1966). “Wave boundary layers and friction factors.” *10th International Coastal Engineering Conference*, Tokyo.

Keeley, J. R. and Bowen, A. J. (1977). “Longshore variations in the longshore current.” *Canadian Journal of Earth Sciences*, 14(8), 1897-1905.

Keen, A. S., Holman, R. A., and Reuben, J. (2012). “Optical estimation of breaking wave induced dissipation.” *Ocean Sciences Meeting*, AGU, Salt Lake City, UT.

Kirby, J. T., and Dalrymple, R. A., (1994). “Combined refraction/diffraction model REF/DIF-1 version 2.5.” *Technical Report CACR-94-04*, Center for Applied Coastal Research, Univ. of Delaware.

Kirby, J. T., Dalrymple, R. A., and Shi, F. (2004). “Refraction-Diffraction model REF/DIF-S version 1.3, documentation and user’s manual.” *Research Report CACR-04-01.*, Center for Applied Coastal Research, Univ. of Delaware.

Lippmann, T. C. and Holman, R. A. (1989). “Quantification of sand bar morphology: a video technique based on wave dissipation.” *Journal of Geophysical Research*, 94(C1), 995-1011.

List, J. H., Benedet, L., Hanes, D. M., and Ruggiero, P. (2009). “Understanding differences between Delft3D and empirical predictions of alongshore sediment transport gradients.” *Proc. 31st International Conference on Coastal Engineering*, World Scientific, Singapore, 1864-1875.

List, J. H., Warner, J. C., Thieler, E. R., Haas, K. A., Voulgaris, G., McNinch, J. E., and Brodie, K. L. (2011). “A nearshore processes field experiment at Cape Hatteras, North Carolina, U.S.A.” *Proceedings of the Coastal Sediments*, Hackensack, N.J., World Scientific Publishing, 2144-2157.

Longuet-Higgins, M. S. (1970a). “Longshore currents generated by obliquely incident sea waves, 1.” *Journal of Geophysical Research*, 75(33), 6778-6789.

Longuet-Higgins, M. S. (1970b). “Longshore currents generated by obliquely incident sea waves, 2.” *Journal of Geophysical Research*, 75(33), 6790-6801.

Longuet-Higgins, M. S. and Stewart, R. W. (1964). “Radiation stresses in water waves; a physical, discussion, with applications.” *Deep-Sea Research*, 11(4), 529-562.

Markham, V. D. and Steinzor, N. (2006). “U.S. national report on population and the environment.” *Center for Environment and Population*, Library of Congress Number: 2006902653.

McNinch, J. E. and Luettich, R, A. (2000). “Physical processes around a cuspate foreland: implication to the evolution and long-term maintenance of a cape-associated shoal.” *Continental Shelf Research*, 20, 2367-2389.

McNinch, J. E. and Wells J. T. (1999). “Sedimentary processes and depositional history of a cape-associated shoal, Cape Lookout, North Carolina.” *Journal of Marine Geology*, 158, 233-252.

Mei, C. C and Liu, P. L-F. (1977). “Effects of topography on the circulation in and near the surf zone – linear theory.” *Estuarine and Coastal Marine Science*, 5(1), 25-37.

Nielsen, P. (1999). “Simple equipment for coastal engineering research and teaching.” *Proceedings of the Fifth International Conference on Coastal & Port Engineering in Developing Countries*, Cape Town, South Africa, 1029-1037.

Nielsen, P., Brander, R. W., and Hughes, M. G. (2001). ”Rip currents: observation of hydraulic gradients, friction factors and wave pump efficiency.” *Proceedings from the Fourth Conference on Coastal Dynamics*, ASCE, 483-492.

Park, J-Y. and Wells, J. T. (2005). “Longshore transport at Cape Lookout, North Carolina: shoal evolution and the regional sediment budget.” *Journal of Coastal Research*, 21(1), 1-17.

Park, J-Y. and Wells, J. T. (2007). “Spit growth and downdrift erosion: results of longshore transport modeling and morphologic analysis at the Cape Lookout cuspate foreland.” *Journal of Coastal Research*, 23(3), 553-568.

Perkovic, D., Lippmann, T. C., and Frasier, S. J. (2009). “Longshore surface currents measured by Doppler radar and video PIV techniques.” *IEEE Transactions on Geoscience and Remote Sensing*, 47(8), 2787-2800.

Putrevu, U., Oltman-Shay, J., and Svendsen, I. A. (1995). “Effect of alongshore nonuniformities on longshore current predictions.” *Journal of Geophysical Research*, 100(C8), 16119-16130.

Reniers, A. J. H. M., van Dongeren, A. R., Battjes, J. A., and Thornton, E. B. (2002). “Linear modeling of infragravity waves during Delilah.” *Journal of Geophysical Research*, 107(C10), 3137.

Ruessink, B. G., Miles, J. R., Feddersen, F., Guza, R. T., and Elgar, S. (2001). “Modeling the alongshore current on barred beaches.” *Journal of Geophysical Research*, 106(C10), 22451-22463.

Shi, F., Hanes, D. M., Kirby, J. T., Erikson, L., Barnard, P., and Eshleman, J. (2011). “Pressure-gradient-driven nearshore circulation on a beach influenced by a large inlet-tidal shoal system.” *Journal of Geophysical Research*, 116(C04020).

Shi, F., Kirby, J. T., Newberger, P., and Haas, K. A. (2005). “Master program for nearshore community model, version 2005.4.” *Documentation and User’s Manual*, NOPP Nearshore Community Model Research Group.

Stockdon, H. F. and Holman, R. A. (2000). “Estimation of wave phase speed and nearshore bathymetry from video imagery.” *Journal of Geophysical Research*, 105(C9), 22015-22033.

Svendsen, I. A. and Putrevu, U. (1994). “Nearshore mixing and dispersion.” *Proceedings of the Royal Society, London*, A 445, 561-576.

Svendsen, I. A., (2006). Introduction to Nearshore Hydrodynamics. *World Scientific*, pp. 722.

Svendsen, I. A., Haas, K. A., and Zhao, Q. (2002). “Quasi-3D nearshore circulation model SHORECIRC, version 2.0.” *Research Report CACR-02-01*, Center for Applied Coastal Research, Univ. of Delaware.

Thieler, E. R. and Ashton, A. D. (2011). “’Cape capture’: geological data and modeling results suggest the Holocene loss of a Carolina Cape.” *Geology*, 39(4), 339-342.

Thornton, E. B. (1970). “Variation of longshore current across the surf zone.” *Proc. Coastal Engineering Conference 12th*, New York, ASCE, 291-308.

Thornton, E. B. and Guza, R. T. (1983). “Transformation of wave height distribution.” *Journal of Geophysical Research*, 88(10), 5925-5938.

Willson, R. G. and Shafer, S. A. (1994). “What is the center of the image?” *Journal of the Optical Society of America A*, 11(11), 2946-2955.

Wu, C. S., Thornton, E. B., and Guza R. T. (1985). “Waves and longshore currents: comparison of a numerical model with field data.” *Journal of Geophysical Research*, 90(C3), 4951-4958.